UNIVERSITY OF CALIFORNIA
RIVERSIDE

Dynamic Processes in Biological Systems: From Capsid Disassembly to Tissue Growth and Bacterial Chemotaxis

A Dissertation submitted in partial satisfaction
of the requirements for the degree of

Doctor of Philosophy

in

Physics

by

Alireza Ramezani

September 2023

Dissertation Committee:

Prof. Roya Zandi, Co-Chairperson
Prof. Mark Alber, Co-Chairperson
Prof. John Barton

The Dissertation of Alireza Ramezani is approved:

Committee Co-Chairperson

Committee Co-Chairperson

University of California, Riverside

Acknowledgments

Graduate school is a challenging but incredibly rewarding experience. It is a time filled with growth, friendship, and endless opportunities for learning. However, this would not have been possible for me without the individuals who helped me through this journey. I would like to take this opportunity to acknowledge all the people who have helped and supported me during these years.

First of all, I would like to express my heartfelt gratitude to my advisors, Prof. Roya Zandi, and Prof. Mark Alber for their support, guidance, and insightful comments. I am grateful for the opportunity to have them as my advisors, and I will always remember the impact they have had on my life.

I would also like to thank my committee member Prof. John Barton for his time and effort reviewing my dissertation. I would like to extend my sincere gratitude to Prof. Weitao Chen, Dr. Ali Nematbakhsh, Prof. Paul Van der Schoot, Prof. Jan C. M. van Hest, Prof. William Cannon, Prof. Dale Pelletier, Prof. Scott Retterer, Dr. Tomas Rush, Dr. Suzanne B.P.E. Timmersmans, and Prof. Huijing Du. It was a pleasure to work with them. Their expertise and insights have added valuable perspectives to my research and made my projects stronger as a result.

I would like to thank Dr. Ali Nematbakhsh, who was my mentor when I joined the lab. He taught me all the measurement and data analysis techniques patiently and were always there to answer my questions.

I would like to thank Amin Safdari, Sanaz Panahandeh, Yinan Dong and Siyu Li for not only providing a supportive and collaborative environment at work but also for their

friendship. Their friendship, technical assistance, and shared passion for our research have made this experience truly enjoyable. I will always cherish the friendships I have formed with them.

I would also like to thank others who helped me during my research: Hodjat Asghari Esfeden, Austin Hansen, Christian Michael, Sam and Jolene Britton, Hamed Assasi, and Amir Aghaei for their friendship and the interesting discussions we had.

The past seven years in Riverside have been the most wonderful times of my life, spending time with my supportive friends. I would like to thank all of them: Amin Safdari, Mahsa Servati, Marziye Jafariyazdani, Hodjat Asghari Esfeden, Hoda Naghibi, Valeh Ebrahimi, MohammadAmin Baniasadi, Sajjad Bahrami, Fahimeh Arab, Mohsen Karimi, Rasoul Ghadami, Yasin Mazloumi, Maryam Shahcheraghi, mahdi Kohansal, Sanaz Panahandeh, Negin Entezari, AmirAli Darvishzadeh, Shirin Masoumi, Shabnam Etemadi, Arash Mehrkesh, Rabi Rad (Naneh Aein), Mahbod Affarin, and Zahra Nataj.

Most importantly, I want to give my deepest thanks first to my parents, Sima Ostadazim and Morteza Ramezani, for their unconditional love and support. Their faith in me and my abilities has been a source of strength and motivation during the most challenging times of my academic journey. Although being on the other side of the planet may separate us physically, Their love and support will always be with me. Thank you, Maman and Baba, for everything. And to my sister, Shahrzad, I am so blessed to have you in my life. Thanks for your love and encouragement.

Last but not least, I would like to say thank my wife, Arezoo, who has been my constant source of support and encouragement throughout my PhD journey. Her unwavering

love, patience, understanding, and culinary skills have given me courage. This achievement would not have been possible without her. Thank you for always being there for me; I love you!

To my beloved spouse, my lovely sister, and my dear parents.

ABSTRACT OF THE DISSERTATION

Dynamic Processes in Biological Systems: From Capsid Disassembly to Tissue Growth and Bacterial Chemotaxis

by

Alireza Ramezani

Doctor of Philosophy, Graduate Program in Physics
University of California, Riverside, September 2023
Prof. Roya Zandi, Co-Chairperson
Prof. Mark Alber, Co-Chairperson

This thesis explores three projects, offering valuable insights into the dynamic processes governing biological systems. The first project focuses on Cowpea chlorotic mottle virus (CCMV) as a model for virus assembly and disassembly studies. A novel model based on classical nucleation theory explains spontaneous and reversible size conversion of empty CCMV capsids by accounting for the change in free protein concentration during capsid assembly and disassembly.

The second project focuses on growth regulation mechanisms in the *Drosophila* wing disc tissue, an ideal model for studying developmental processes. We develop a multiscale chemical-mechanical model that integrates morphogen gradients, mechanical forces, and tissue dynamics. By comparing spatial distribution of dividing cells in simulations with experimental data, we reveal the critical role of the Dpp morphogen gradient in determining tissue size and shape. If the Dpp gradient spreads in a larger domain a larger tissue size with more symmetric shape can be achieved at a faster growth rate. Additionally, feedback

regulation involving Dpp receptor downregulation enables further morphogen spreading, prolonging tissue growth at a spatially homogeneous rate. This comprehensive model provides a deeper understanding of the interplay between chemical signals and mechanical forces, illuminating the mechanisms controlling tissue growth.

The third project concentrates on bacterial behavior, utilizing a sub-cellular element model to understand dynamics of bacterial chemotactic behavior and its impact on bacterial trajectories. We have investigated bacterial swimming patterns including run-reverse and run-wrap reverse, in addition to chemotaxis strategies in which the bacteria exhibit different responses to the chemoattractant in different swimming modes, including cases where they may not react at all. We have found that simpler motility patterns emerge greater chemotaxis efficiency compared to complicated swimming patterns. In addition, we have discovered that a complicated swimming pattern could lead to bacterial aggregation, only if the dominant swimming mode is involved in the chemotaxis strategy. Based on our simulations, it has been found that bacteria with a simple swimming pattern lacking in enough reorientations can recover their chemotactic behavior by adopting a more complex pattern even if the bacteria won't respond to the chemical gradient in the adopted mode.

Contents

List of Figures

Chapter 1

Introduction

Virus Disassembly

Viruses have captivated the attention of scientists for centuries. A virus is a unique entity that exists at the interface of the living and non-living worlds. Unlike cells, viruses are acellular particles that lack the essential machinery for self-replication and metabolism. Instead, viruses are composed of genetic material, which can be either DNA or RNA, enclosed within a protein coat called a capsid. The capsid plays a critical structural component, providing stability to the viral genome and facilitating its transmission between host cells. The genetic material carries the instructions required for viral replication. Viruses are considered obligate intracellular parasites, as they rely on host cells to provide the necessary cellular machinery and resources for their replication, and propagation. Outside of a host cell, viruses remain inert, but once they infect a susceptible host cell, they exploit the cellular machinery to undergo replication, assembly, and ultimately, the release of progeny viral particles. Understanding the processes by which viruses enter host cells and release

their genetic material is essential in understanding viral infection and pathogenesis. Viruses employ diverse strategies to enter host cells, depending on their type. Enveloped viruses possess a lipid envelope derived from the host cell membrane and can enter the cell through membrane fusion or endocytosis. Membrane fusion occurs when viral envelope proteins interact with specific receptors on the host cell membrane, leading to the fusion of the viral envelope with the cell membrane and subsequent release of the viral capsid and genetic material into the cytoplasm. Alternatively, through endocytosis, the entire virus particle is engulfed by the host cell and forms an endosome. The virus then disrupts the endosomal membrane, releasing the capsid and genetic material. Non-enveloped viruses, lacking a lipid envelope, often rely on direct penetration of the host cell membrane, facilitated by specific interactions between viral proteins and cell surface receptors. These interactions trigger conformational changes in viral proteins, allowing the release of the viral genome into the host cell. Looking into the assembly and disassembly of viral capsids provides valuable insights into viral replication, pathogenesis, and the development of antiviral strategies. By understanding the complexities of these processes, we can enhance our ability to combat viral infections, improve public health, and advance scientific knowledge in diverse fields such as virology, medicine, and nanotechnology.

The Caspar and Klug model improved our understanding of viral architecture and assembly. The model is based on icosahedral symmetry, describing the arrangement of protein subunits within viral capsids. It provides a general framework for understanding the assembly of viral capsids. The T-number refers to the triangulation number, which is a measure of the symmetry and arrangement of subunits within the capsid structure.

The number of protein subunits needed to construct a capsid increases with the T-number. These size variations can impact the stability, infectivity, and interactions with host cells or the immune system.

Classical nucleation theory (CNT) provides a framework for understanding the dynamic processes of assembly and disassembly in capsid formation. CNT is a well-established concept in the field of phase transitions and provides insights into how capsids assemble from individual protein subunits or disassemble into their building blocks. CNT describes the initial stages of nucleation, where the first few protein subunits come together to form a stable nucleus. The nucleus then acts as a template for the subsequent addition of more subunits, leading to the growth of the capsid. During assembly, the formation of the nucleus involves overcoming an energy barrier known as the nucleation barrier. This barrier arises due to unfavorable interactions or conformational changes required for subunits to come together in a specific configuration. Once the nucleus is formed and exceeds a critical size, it becomes thermodynamically favorable for additional subunits to bind, leading to the rapid growth of the capsid. CNT explains that nucleation is a stochastic process influenced by factors such as subunit concentration, temperature, and height of barriers.

On the other hand, CNT also applies to the dissociation of capsids. Disassembly occurs when the capsid is destabilized, resulting in the breakdown of protein-protein interactions and the release of subunits. Capsid disassembly can be influenced by factors such as changes in pH, or temperature. CNT explains that disassembly occurs when the energy required to break the protein-protein interactions exceeds the energy gained from holding the capsid structure. CNT explains the initial nucleation steps, the growth of capsids from

stable nuclei, and the factors that influence these processes. By applying CNT principles, researchers can gain insights into the kinetics of capsid assembly and disassembly, facilitating the design of strategies to manipulate and control these dynamic processes. In our study, we utilized a modified classical nucleation theory (CNT) framework, considering only subunits and fully formed capsids in the solution while excluding the presence of intermediate states. This assumption arises because intermediate states may be energetically unstable or short-lived, making their detection challenging or limited. By focusing on subunits and fully formed capsids, we simplify the analysis and concentrate on the key components likely to play significant roles in the assembly and disassembly processes. This approach has potential consequences on our understanding of the kinetics of capsid assembly and disassembly. By disregarding intermediate states, we may overlook important transitional steps and the associated kinetics involved in the pathway. Additionally, the exclusion of intermediate states might impact our ability to fully comprehend the factors influencing assembly and disassembly dynamics, such as kinetic barriers and cooperative interactions. It is important to acknowledge that intermediate states could contribute to the overall assembly landscape, affecting the pathway, and efficiency of capsid formation. However, focusing on subunits and fully formed capsids simplifies the analysis and facilitates the characterization of the dominant structures present in solution. This approach may allow us to discover fundamental principles governing capsid assembly and disassembly, highlighting critical factors that contribute to the formation of stable capsid structures. Future studies could explore methods to further investigate and characterize these intermediate states.

Here, we calculate time-series concentrations of different capsid sizes by integrating rate equations driven from CNT, with the Euler-forward method. This approach provides a dynamic perspective on the assembly and disassembly processes of capsids and allows us to track the changes in concentration over time. It provides a quantitative framework for analyzing the kinetics and dynamics of these processes.

Growth Regulation on Tissue Growth

As we delve into these microscopic entities, we also step into the world of tissue development. Tissue growth control lies at the heart of developmental biology and is a fundamental process in maintaining tissue homeostasis and function. Precise regulation of tissue growth is essential for organisms to achieve proper organ size, shape, and functionality. Deviations from normal growth patterns can lead to developmental abnormalities, tissue overgrowth, or underdevelopment, all of which can have profound implications for an organism's health and well-being. Furthermore, dysregulated tissue growth is a reason of many diseases, including cancer. Abnormal growth patterns and uncontrolled cell proliferation can lead to the formation of tumors and the spread of malignant cells. Understanding the mechanisms that govern tissue growth is crucial for explaining the fundamental principles of embryonic development, and tissue repair. By unraveling the complicated regulatory pathways involved in growth control, researchers can gain insights into how cells proliferate, differentiate, and organize to form complex tissues and organs.

The Drosophila wing disc is a simple epithelial structure found during the larval stages of Drosophila development. It gives rise to the adult wing, and its growth and patterning are tightly regulated to ensure proper wing formation. The wing disc has different

compartments, such as the anterior and posterior compartments, providing a spatially controlled environment for studying the effects of morphogens and their spreading on tissue growth. The Drosophila wing disc serves as an invaluable model system for understanding the fundamental principles of tissue growth and development. Its remarkable regenerative capacity, well-defined structure, and conserved molecular mechanisms make it an ideal platform for studying the interplay between morphogen signaling, cellular processes, and tissue growth dynamics. The disc serves as a model to explore how morphogens, such as Decapentaplegic (Dpp) and Wingless (Wg), establish concentration gradients, which play essential roles in patterning and growth regulation. These morphogens are secreted from specific localized sources within the disc, and their diffusion and spreading influence the activation of downstream signaling pathways and cellular responses.

Regulation of tissue growth involves complex molecular mechanisms. One prominent example is the growth regulation model centered around Decapentaplegic (Dpp), a morphogen in the Transforming Growth Factor-β (TGF-β) family, which plays a crucial role in various developmental processes, including tissue growth and patterning in vertebrates. Dpp gradient is established through a combination of localized Dpp production, diffusion, and interaction with extracellular inhibitors. Cells interpret the Dpp concentration as a positional cue, which determines their fate, proliferation rate, and patterning.

Experimental evidence and mathematical modeling have provided insights into the mechanisms underlying Dpp-mediated growth regulation. Mathematical models, such as reaction-diffusion, have been used to simulate Dpp distribution and its impact on tissue growth. These models incorporate parameters such as Dpp production, diffusion, degra-

dation, and interaction with inhibitors to predict the concentration gradient and subsequent cellular responses. Furthermore, studies have identified downstream feedback loops, involving transcriptional regulation, receptors, and extracellular modulators. These feedback loops contribute to the precise control of Dpp signaling, ensuring robust and dynamic growth regulation. These models have implications beyond Drosophila development, as similar growth regulation principles have been observed in other organisms.

Mechanical models have played a key role in understanding growth regulation by investigating the physical forces and mechanical properties that underlie these processes. Several mechanical models, including agent-based models, vertex-based models, and subcellular element models, have been proposed to study growth regulation. These models can incorporate various parameters such as tissue stiffness, growth rates, and external mechanical forces to analyze tissue growth patterns and predict the mechanical properties of developing tissues. These models provide a quantitative framework to explore the effects of mechanical forces, cell-cell interactions, and tissue mechanics on growth dynamics.

Understanding the complex processes of tissue growth and morphogenesis requires the integration of both mechanical and chemical cues. The interplay between these cues plays a critical role in shaping tissues and organs during development. While chemical cues, such as morphogens and signaling molecules, provide positional information and guide cellular behaviors, mechanical cues, including forces and physical properties, influence cell behavior, tissue organization, and overall growth dynamics. Mechanical cues are also known to influence cellular signaling pathways and gene expression, providing feedback mechanisms that regulate tissue growth. Likewise, chemical signals can influence mechanical properties,

such as tissue stiffness or contractility, thereby influencing tissue growth. The interplay between mechanical and chemical cues presents a dynamic feedback system that influences cellular behavior and tissue organization. The combined consideration of mechanical and chemical cues not only improves our understanding of developmental processes but also offers insights into tissue engineering strategies, and the treatment of developmental disorders and diseases. In this study, we build upon previous mechanical and chemical models to develop a refined framework for studying growth regulation. By incorporating novel aspects, such as the impact of morphogen gradient, we aim to gain deeper insights into the complex interplay between chemical signaling dynamics and tissue growth.

Bacterial Chemotaxis

The exploration of biological systems extends beyond viral capsids and tissue growth to contain the bacterial behavior. Bacteria provide a fascinating platform to investigate the principles that govern living organisms at a cellular level. Rotation of flagella generates propulsive force and enables bacteria to exhibit various swimming patterns, including straight runs, tumbles, and directed changes in direction. Flagellated motion grants bacteria the ability to actively explore their surroundings, respond to environmental cues, and find niches for growth and reproduction. By altering the rotational direction of their flagella, bacteria can modulate their movement in response to external cues such as chemical gradients. This chemotactic behavior allows bacteria to move towards or away from specific substances, aiding in the search for nutrients, avoiding toxins, and navigation towards optimal environments. Lastly, this thesis extends its exploration with a focus on modeling chemotactic bacteria, as another application of sub-cellular element model. Here,

we delve into the dynamic motion of *Pseudomonas*, a chemotactic bacteria to unravel the complexities of bacterial navigation within chemical gradients. We study various swimming patterns and chemotaxis strategies by dynamically controlling the bacterial reversal frequency. Our results reveal that a simple motility pattern proves to be more efficient in terms of chemotaxis than complex patterns like run-wrap-reverse. Additionally, we observe that the wrap mode might enhance chemotaxis efficiency, particularly when bacterial reorientation is limited within the run-reverse pattern. Moreover, our research highlights that a complex swimming pattern might lead to aggregation, but only when the dominant swimming mode is chemotactic.

Summary

All projects in this thesis revolve around the interactions within larger systems. They study how regulating a micro scale interaction or a behavior might control the macro scale outcome. Considering these projects, this thesis focuses on an exploration of dynamics in biological systems' behavior across diverse scales.

Chapter 2

The Dynamics of Viruslike Capsid Assembly and Disassembly: Theoretical methods

Based on previous experimental, theoretical and computer simulation results, we propose that nucleation serves as the fundamental process governing capsid assembly and disassembly.[1, 2, 3] To this end, we combine equilibrium theory, inspired by the physics of supramolecular polymers, and classical nucleation theory (CNT).[4] This allows us to calculate the time evolution of the assembly and disassembly of mixtures of capsids, the predictions of which we compare with experimental results provided by our collaborators [5] . Note that the kinetics of assembling free subunits into competing capsids with different T numbers has been previously explored. [6, 7] However, a kinetic theory of T number conversion has not yet been attempted. To derive the essential thermodynamic parameters

needed for our kinetic theory, we formulate the free energy of an aqueous solution containing exclusively free ELP-CCMV subunits and fully formed capsids. In our equilibrium theory, we neglect intermediate states since previous experimental and simulation studies demonstrate that these states are nearly undetectable (if present at all) and represent short-lived states.[5, 8, 9, 10, 11, 12] Within a mean-field approximation, the dimensionless free energy f per solvent molecule in a dilute, aqueous solution represented as follows:

$$f = x_s ln x_s - x_s + \sum_{T=1,3} x_T ln x_T - x_T + \sum_{T=1,3} q_T g_T x_T \tag{2.1}$$

Here x_s is the mole fraction of ELP-CP subunits, while x_1 and x_3 correspond to the mole fractions of the fully formed capsids for T=1 and T=3 species, respectively. Free energy per solvent molecule is measured in units of the thermal energy $k_B T$ with k_B Boltzmann's constant and T the absolute temperature. See Refs.[4, 13] for the derivation of Equation 2.1. The effective binding free energy between ELP-CP subunits in T=1 and T=3 capsids are represented by g_1 and g_3, respectively. These binding free energies are measured in units of thermal energy and are averaged over all subunits of a fully formed capsid. Additionally, q_1 and q_3 represent the number of subunits that constitute the capsid of the T=1,3 shells, respectively. The first six terms in Equation 2.1 represent the translational entropy and the entropy of mixing while the last two terms account for the overall (net) binding free energy of the subunits in assemblies.

An important factor in the development of the classical nucleation theory for virus capsids, is the difference between the chemical potential of free protein subunits in the metastable solution and bound proteins in the capsids. The chemical potential of the

free protein subunits in solution, $\mu_s = \partial f/\partial x_s$, and chemical potentials of the capsids, $\mu_T = \partial f/\partial x_T$, follow from Equation 2.1 where T=1,3 indicate the T number of the shell. The equilibrium distribution of proteins over the free proteins and different types of capsids can be obtained by minimizing Equation 2.1 subject to the condition of conservation of mass, $c_s = x_s + q_1 x_1 + q_3 x_3$, with c_s the overall mole fraction of coat proteins in solution. The resulting mass-action equations are $x_T = (x_s e^{-g_T})^{q_T}$ with T=1,3. The reference chemical potentials are tacitly absorbed in the binding free energies g_T. For each type of capsid, there is a critical free protein concentration c_T^* below which the concentration of capsids is almost zero as the number of subunits in the capsids, q_T, is large compared to unity. For CCMV, the basic protein subunits are dimers, so $q_1 = 30$ for the T=1 and $q_3 = 90$ for the T=3 capsid.

Using the equilibrium theory described above, we can now set up the kinetic theory of capsid assembly and disassembly within the framework of CNT.[2] The Gibbs free energy of the formation of an incomplete spherical capsid of the T species containing $n_T = 1, ..., q_T$ molecules with a circular rim can be written as

$$\Delta G_T(n_T) = n_T \Delta\mu_T + a_T \sqrt{(q_T(q_T - n_T)} \tag{2.2}$$

where $a_T = 4\pi R_T \sigma_T / q_T$ is a dimensionless magnitude of the rim energy, with R_T the radius of the shell and σ_T the free energy cost per unit length of the rim [4]. σ_T can be estimated as $\sigma_T = -s g_T / r_T$ where $s \in [0, 1]$ is a geometric factor indicating the average fraction of bonds that a subunit on the rim is missing, which depends on the local coordination number and roughness of the rim. r_T is the effective diameter of a protein

unit that is approximated as a disk. Assuming that the surface of a fully formed capsid is covered entirely by capsid proteins, the effective diameter can be written as $r_T = \sqrt{\frac{q_T}{4R_T}}$ [2]. A previous and more detailed study on the line tension of shells composed of Lennard-Jones disks, packed on the surface of sphere, shows that $s \approx 0.3 - 0.4$, with the latter value an upper limit as proteins are more flexible than Jennard-Jones particles - we set $s = 0.3$ in our simulations [14]. Finally, the first term in Equation 2.2 represents the thermodynamic driving force for the assembly or disassembly of capsids. To obtain the dimensionless barrier height, ΔG_T^* for the two T numbers, we calculate the critical nucleus size n_T^*, that is, find the value of n_T for which Equation 2.2 is maximal and insert this into Equation 2.2 to obtain

$$\Delta G_{as,T}^* = \Delta G_T^0(\sqrt{\Gamma_T^2 + 1} - \Gamma_T) \tag{2.3}$$

where $\Delta G_T^0 \equiv q_T a_T/2$ is the maximum barrier height and $\Gamma_T \equiv -\Delta\mu_T/a_T$ is a measure for the degree of super- or undersaturation for the species. We note that Γ_T depends on the concentration of a capsid.

In the process of assembly of a capsid, subunits can attach to and detach from the growing shell through a sequence of what we presume to be reversible kinetic steps. Within the classical nucleation theory, the rate of capsid assembly is limited by the formation rate of the energetically most unfavorable critical nucleus through the Boltzmann weight ΔG_T^* that acts as a kinetic bottleneck. The steady-state nucleation rate for association reads [4]:

$$J_{as,T} = x_s \nu_T^* Z_T e^{-\Delta G_{as,T}^*}, \tag{2.4}$$

where $Z_T = \sqrt{\frac{-1}{2\pi}(\partial^2 \Delta G_T/\partial n^2)\mid_{n=n_T^*}} = \sqrt{\frac{a_T}{q_T \pi}}(1+\Gamma_T^2)^{3/4}$ is the so-called Zeldovich factor which characterizes the sharpness of the free energy barrier. It can be interpreted as a measure of the lifetime of the critical nucleus of size n_T^*, indicating how long the nucleus persists before transitioning to further assembly or dissociation [8]. The attempt or attachment frequency ν_T^* of the monomers attaching to the critical nucleus varies based on the mode of attachment. It can be influenced by factors such as the diffusivity and concentration of free monomers, the size of the critical nucleus, and an internal molecular time scale associated with the docking process [15]. To simplify the analysis, we make the assumption that the attempt frequency does not rely on the size of the clusters or the concentration.

In modeling the disassembly process, we consider the initial state as a fully formed capsid. Within classical nucleation theory, the rate of capsid disassembly is constrained by the dissociation of the critical nucleus. Specifically, it depends on the time required to overcome the height of the free energy barrier $\Delta G_{dis,T}^*$, but in this case, the process occurs in the opposite direction compared to the assembly process. The nucleation rate for disassembly of complete capsids of species T reads

$$J_{dis,T} = x_T \nu_T^* Z_T e^{-\Delta G_{dis,T}^*} \tag{2.5}$$

where $\Delta G_{dis,T}^*$ represents the free energy barrier for the disassembly of a shell to form monomers. Notice that the dissociation rate depends on x_T, the capsid concentrations of species T=1,3. We will assume that the attachment frequency associated with the association process is equal to that of the dissociation process, as they describe the same process. We presume it to be independent of the size of the critical nucleus [16].

Because capsids with different T numbers have different radius of curvature, we do not allow for a direct transition from one T number to another one. In our reaction path pathway, growth or disassembly can only proceed by the shedding or docking of individual protein subunits, which for CCMV constitute coat protein dimers. This reaction path is well supported by experimental evidence, as there are no indications of partially disassembled T=3 particles spontaneously transforming into T=1 particles, or vice versa. Similarly, T=1 particles do not exhibit a tendency to open up and incorporate subunits to grow into T=3 particles [5]. Thus, we make the presumption that, firstly, one type of capsid disassembles into dimers. Secondly, free dimers subsequently reassemble into different capsid sizes according to their corresponding assembly nucleation rates.

Presuming that kinetic processes are sufficiently slow to allow us to use the expressions for steady-state nucleation rates for association and dissociation, i.e., presume a quasi steady state to hold, the set of equations describing the concentration of dimers, T=1 and T=3 capsids in our system can finally be expressed as follows,

$$\frac{dx_s}{dt} = -q_1 J_{as,1} - q_3 J_{as,3} + q_1 J_{dis,1} + q_3 J_{dis,3} \tag{2.6}$$

and

$$\frac{dx_T}{dt} = J_{as,T} - J_{dis,T} \tag{2.7}$$

The expressions on the left-hand sides of Eqs. (2.6 and 2.7) represent time derivatives of the concentrations of the three components in our model. On the right-hand sides, the terms account for the variations resulting from the formation or dissociation of capsids.

Throughout the process, all concentrations are considered to be time-dependent while still adhering to mass conservation principles at all times. To solve the aforementioned system of equations numerically, we employ an explicit forward Euler method with adaptive time steps. (See 2.1 for more information.)

Using the solutions obtained from these equations, we can compute the fraction of dimers present in each type of capsid relative to the total number of dimers across all capsids,

$$f_T = \frac{q_T x_T}{\sum_{i=1,3} q_i x_i} \tag{2.8}$$

where T=1,3. In general, the time steps in the simulations depend on various parameters, such as the attempt frequency, binding energies and size of the capsids. In order to fit the theory to the experimental data, we choose one experimental data point in the time series of the disassembly of T=3 and the assembly of T=1, and use it as our reference point. When we find the same ratio of proteins in the two kinds of capsid in our simulations as that in the experiments, we set the time in the simulations equal to the time in the experiments. Next, we rescale all other simulation data points accordingly. We repeat this process for the disassembly of T=1 and the assembly of T=3. To check the robustness of this technique, we consider different data points as the reference point. The agreement between theory and experiments does not depend strongly on the reference point that we take. (See 3.3.4 for more information.)

It is important to realize that the time that it takes to change the pH and the salt concentration of the buffer solution might not be exactly the same in each experiment. In addition, the lag time for assembly and disassembly of capsids with different sizes are

arguably different. Therefore it is difficult to pinpoint the actual "time zero" for each individual experiment. In order to deal with this uncertainty, our collaborators start collecting data 30 minutes after the experiment commences. We assume that the lag times are negligible on the time scale of the experiment, thus we ignore the first phase of assembly in CNT in which capsids have not started to assemble or disassemble [4].

2.1 Numerics

The kinetics equations predicted by CNT (Eqs. 2.6 and 2.7) are solved by using finite difference methods. Assembly and disassembly nucleation rates at the beginning of the simulation are determined by the initial conditions. The concentrations of capsids and free dimers are calculated at each time step, using the values and nucleation rates at the previous time step. Hence, our time-stepping equations read:

$$x_s^{t+\Delta t} = x_s^t + (-q_1 J_{as,1}^t - q_3 J_{as,3}^t + q_1 J_{dis,1}^t + q_3 J_{dis,3}^t)\ \Delta t \tag{2.9}$$

and

$$x_T^{t+\Delta t} = x_T^t + (J_{as,T}^t - J_{dis,T}^t)\ \Delta t \tag{2.10}$$

where x_s^t and x_T^t are the concentrations of free dimers and capsids of size T at time t; q_1 and q_3 represent the number of subunits in each fully formed capsid of size T=1 and T=3. As already alluded to, we assume that dimers are our building blocks, so that $q_1 = 30$ and $q_3 = 90$. The instantaneous steady-state assembly and disassembly nucleation rates of capsid size T at time t are $J_{as,T}^t$ and $J_{dis,T}^t$, respectively.

The nucleation rates depend highly on the free dimer concentration. In order to speed up the simulation, we use an adaptive time step such that a maximum of 0.01% of free dimers at time t can be consumed by growing shells. Similarly, a maximum of 0.01% of free dimers can be released by dissociated shells at time t. In other words,

$$\Delta t = \frac{0.0001 x_s}{Max(J_1^t, J_3^t)} \tag{2.11}$$

where $J_T^t = \mid J_{as,T}^t - J_{dis,T}^t \mid$ is the absolute assembly or disassembly rate of capsid size T. The simulation continues until full depletion of the unfavorable capsid size.

From equilibrium theory and experimental observations, we have to assume that there are some free dimers remaining in the solution before the quench, that is, before the induced shift in pH and in salt concentration that on the time scale of the experiment is (virtually) instantaneous. Therefore, we invoke a non-zero value as our initial free dimer concentration. Quickly after starting the simulation, the dimer concentration converges to a fixed concentration relatively close to what must be the smaller critical concentration. Having initially more dimers in the system leads to the fast formation of capsids. On the other hand, a low dimer concentration at the start of the simulation increases the initial disassembly rate. In order to avoid both of these conditions, we choose the initial dimer concentration near the concentration it converges to. It also helps us to avoid any divergence in the simulation as the dissociation rates increase significantly at low dimer concentrations.

Based on the dimer concentration at the end of the experiment, which is relatively close to the critical concentration of the more stable species, we approximate the total dimer concentration is around 10 times larger than the critical concentration. Therefore,

the overall protein in the unfavorable capsid we set at $10c^*$, where $c^* = Min(c_1^*, c_3^*)$. (See table 3.1 and 3.2 for parameter values.) Due to the universality of the phenomena, the model is capable of reproducing the experimental results by using different binding energies. We decide to fix the binding energy of T=1 in our framework and generate experimental results only by changing the binding energy of T=3. This allows us to have a better comparison between the two types of experiment.

Chapter 3

The Dynamics of Viruslike Capsid Assembly and Disassembly

This results were published [5]. I have contributed to this work by developing the model, computational implementations, computational analysis and curve fittings.

3.1 Introduction

Single-stranded RNA (ssRNA) viruses infect all species in the tree of evolution, causing significant economic damage and health concerns. The ssRNA genome of such viruses is protected by a shell called the capsid, composed of many copies of a single or a few protein subunits. To infect a host cell, a virus needs to enter, disassemble, release its genome, and use the cell's machinery for replication. Clearly, the capsid is a responsive structure: Although it protects the genome and should be stable outside the cell, it must also readily disassemble once inside the cell and present its genome for replication [1, 17].

Arguably the most extensively studied viruses in this context are cowpea chlorotic mottle virus (CCMV) and Brome mosaic virus (BMV), which have proven to be good models for virus replication studies. The disassembly of the capsid in a cell must be triggered by changes in the chemical environment, resulting in the weakening of molecular interactions. Indeed, in vitro studies of CCMV and BMV show that following a pH jump from a neutral to a basic environment at high ionic strength the capsids of these viruses spontaneously disassemble [18, 19, 20]. However, since the spatial and temporal resolution of intermediate structures of these studies are limited, kinetic pathways of disassembly have remained a mystery.

Generally, despite a huge body of work dedicated to understanding virus uncoating, our understanding of its kinetics and the factors contributing to it remains rudimentary [2, 6, 7, 8, 9, 10, 21, 22, 23, 24]. One of the main reasons for the lack of insight is the fact that the assembly of CCMV is governed by two driving forces involving two species, namely, the interaction between the capsid proteins (CPs) and that between the ssRNA and the RNA-binding domain of CPs [13]. Distinguishing the contribution of both in the disassembly is not trivial, as CCMV shells in the absence of genome are not stable under physiological conditions [3, 25].

To develop and validate a plausible model that describes capsid assembly and disassembly, experimental conditions have to be found that allow for the elimination of the contribution of nucleic acids. This would not only lead to a better understanding of virus assembly but also allow for the development of tools to manipulate this process, either by preventing capsid formation and counteracting viral replication or by stabilizing empty

capsids under physiological conditions as tools for diagnostic and therapeutic applications [26].

Several years ago the CP variant ELP-CP, which involves the attachment of elastin-like polypeptides (ELPs) at the N-terminus of the CPs of CCMV have been designed [27]. These ELPs consist of nine repeating Val-Pro-Gly-Xaa-Gly pentapeptide units, which switch from an extended water-soluble state to a collapsed hydrophobic state in response to an increase in temperature and/or electrolyte concentration [28]. At pH 5, the ELP-CPs form viruslike particles (VLPs) with a diameter of 28 nm, similar to the native T = 3 particles [27]. At pH 7.5, wild-type CPs do not assemble into shells, yet ELP-CPs assemble into 18 nm (T = 1) VLPs upon increasing the salt concentration, a process induced by the hydrophobicity of the ELPs [27, 29, 30].

Our collaborators describe the results from time-resolved experiments, and investigate the disassembly of one type of ELP-CP capsid and reassembly of another in response to pH changes (section 3.1) [5]. While changing the pH from 5 to 7.5, they monitor how the T = 3 shells disappear, while the T = 1 shells appear as a function of time. They also study the disassembly of T = 1 capsids and the assembly of T = 3 capsids by lowering the pH from 7.5 to 5. To get a better understanding of the mechanism of transition, our collaborators performed experiments in which they added fluorescently labeled ELP-CPs to unlabeled capsids. They observe that at both pH 5.0 and 7.5 the capsids can exchange dimers with the solution which makes it plausible that the observed size change involves the transfer of dimers [5, 31]. Furthermore, they note that it is unlikely for one structure to morph into the other one without disassembly because of the change in the radius of

curvature between the two structures. If the sizes of the two structures were close to each other, then it would be possible for the big pieces of one shell to be recycled to form another shell [32]. These experimental findings can be explained by a simple model based on classical nucleation theory (CNT) applied to viruslike capsids [4, 15, 33, 34], accounting for the time-evolution of the concentrations of the various species that result from the shedding or addition of single protein subunits as the different types of shell assemble and disassemble. As far as we are aware, this is the first study confirming that both assembly and disassembly of viruslike shells can be explained through CNT as a possible mechanism for quantitatively reproducing experimental data.

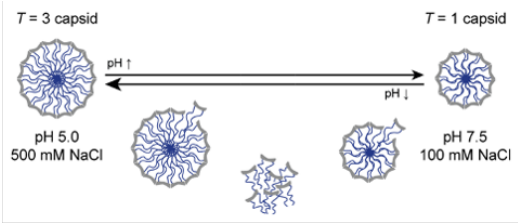

Figure 3.1: Schematic overview of the size change of ELP-CP viruslike particles (VLPs) upon a shift in pH.

3.2 Theory

Experiments suggest that we are pitting the assembly rate of one species against the disassembly rate of another. In order to explore the role of metastability in our experiments, we resort to CNT, as a plausible model to describe the system. Within CNT, the steady-state capsid assembly and disassembly rates $J_{as,T}$ and $J_{dis,T}$ can be written as [4, 16]:

$$J_{as,T} = x_s \nu_T^* Z_T e^{-\Delta G^*_{as,T}} \tag{3.1}$$

$$J_{dis,T} = x_T \nu_T^* Z_T e^{-\Delta G^*_{dis,T}} \tag{3.2}$$

where ν_T^*, Z_T, x_s, and x_T denote the attempt frequency of dimers attaching to the critical nucleus, the Zeldovich factor, and the mole fraction of free subunits, and the capsid of a given T number. $\Delta G^*_{as,T}$ is the height of energy barrier between the free proteins and fully formed capsids, while $\Delta G^*_{dis,T}$ is the height of the free energy barrier between the assembled and free CPs (Figures 3.2D and 3.3D for the opposite size shift). The barrier height depends on the overall protein concentration and on the binding free energies of the proteins in the two types of shell, g_T, in units of thermal energy, averaged over all subunits of a fully formed capsid. The kinetic equations describing the concentration of dimers and T = 1 and T = 3 capsids read as

$$\frac{dx_s}{dt} = -q_1 J_{as,1} - q_3 J_{as,3} + q_1 J_{dis,1} + q_3 J_{dis,3} \tag{3.3}$$

and

$$\frac{dx_T}{dt} = J_{as,T} - J_{dis,T} \tag{3.4}$$

where q_1 and q_3 are the numbers of dimers in fully formed T = 1 and 3 capsids, respectively. The quantities on the left-hand sides of Equations 3.3 and 3.4 represent time derivatives of the concentrations of the species in our model. The terms on the right-hand sides are due to the formation or dissociation of capsids. We solve the above system of equations numerically, using an explicit forward Euler method with adaptive time steps.

3.3 Results

3.3.1 Reassembly during size decrease

Consistent with the experiments performed by our collaborators (Figure 3.2B), we find that upon increasing the pH from 5 to 7.5, the amount of T = 3 structures decreases while at the same time the number of T = 1 structures increases, indicating that under these experimental conditions the protein–protein attraction is stronger between subunits forming T = 1 shells than that of those forming T = 3 ones. Our curve fits in Figure 3.2C for times up to 30 h give $g_1 = -15.0$ and $g_3 = -14.7$ in thermal energy units.

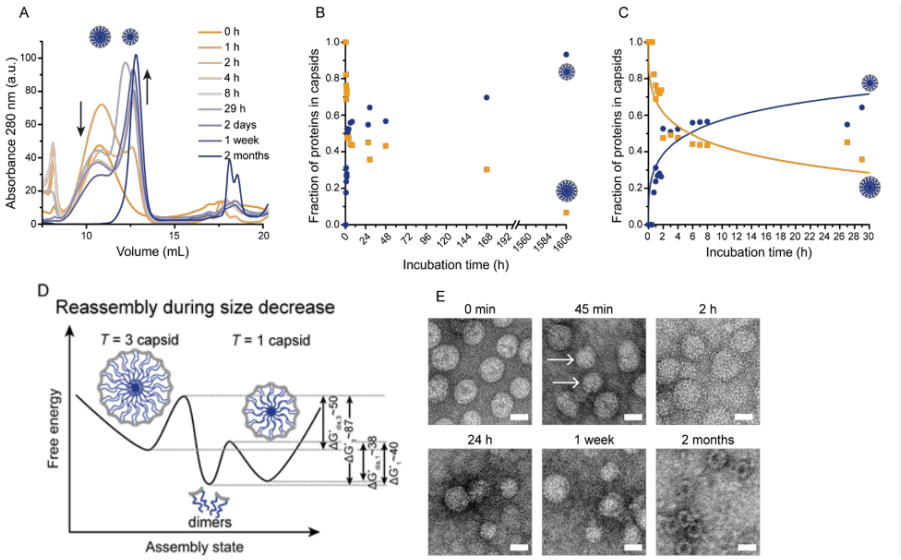

Figure 3.2: Analysis of ELP-CCMV capsids during the transition from T = 3 to T = 1 particles at pH 7.5. (A) SEC chromatograms measured after indicated dialysis times to pH 7.5. (B and C) Protein fractions as T = 1 (blue circles) and T = 3 (yellow squares) capsids as determined by integration of the SEC chromatograms. The solid lines are the results of our numerical solution (Equations 3.3 and 3.4). See Table 3.1 for more details. (D) Schematic overview of the proposed reassembly mechanism during size decrease, where T = 1 capsids are energetically most favorable under the buffer conditions used. ΔG values are in k_BT units. Energy barriers are not drawn to scale; the values provided are indicative. (E) TEM micrographs of samples that were taken after the indicated dialysis times. T = 1 capsids in the 45 min image are indicated with arrows. Scale bars correspond to 20 nm.

As the T = 3 shells disassemble, the concentration of free dimers increases and, at some point, reaches the value of the critical capsid concentration $c_1^* = e^{g_1}$, whereupon T = 1 shells start forming and consuming free dimers. As the free dimer concentration continues to increase, the disassembly rate of the T = 3 shells decreases, and the assembly rate of T = 1 shells increases, explaining the behavior of the disassembly and assembly curves shown in Figure 3.2C. However, fairly quickly the free dimer concentration attains a more or less constant value because the disassembly of T = 3 shells produces dimers that are immediately depleted by the formation of T = 1 shells, confirming that the changes in protein fraction in the capsids are due to the disassembly of T = 3 and assembly of T = 1 (section 3.3.3). We note that the decrease in free dimer concentration after two months in Figure 3.2A could be due to the fact that dimer proteins at pH 7.5 after prolonged storage are not highly stable and some aggregation and denaturation will occur over time. The theory presented in this thesis does not include this effect.

3.3.2 Reassembly during size increase

We next discuss the size shift from T = 1 to T = 3 following a jump in pH from 7.5 to 5 [31]. Figure 3.3A,B show that T = 1 particles, stable at neutral pH, disappear over time, while T = 3 particles appear. The whole process proceeds much more gradually than the opposite size shift and takes around 2 months to reach full completion (Figure 3.3B). Our collaborators monitor the dynamics using Transmission Electron Microscopy (TEM), as shown in Figure 3.3E. TEM analysis confirm the observed increase in the number of T = 3 particles during the assembly and disassembly processes.

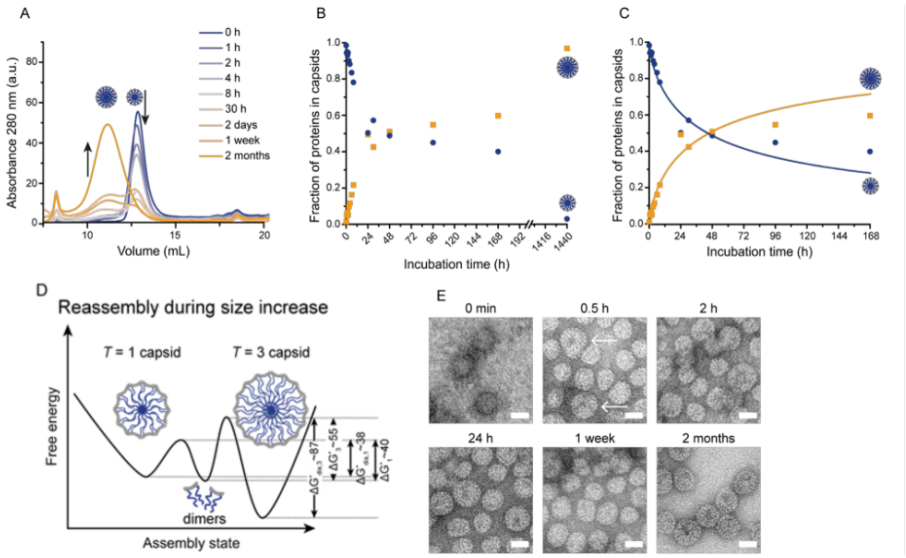

Figure 3.3: Analysis of ELP-CCMV capsids during transition from T = 1 to T = 3 particles at pH 5.0. (A) SEC chromatograms measured after indicated dialysis times to pH 5.0. (B and C) Protein fractions as T = 1 (blue circles) and T = 3 (yellow squares) capsids as determined by integration of the SEC chromatograms . The solid lines are the results of our numerical solution (Equations 3.3 and 3.4). See Table 3.2 for more details. (D) Schematic overview of the proposed reassembly mechanism during size increase, where T = 3 capsids are energetically most favorable under the buffer conditions used. ΔG values are in k_BT units. Energy barriers are not drawn to scale; the values provided are indicative. (E) TEM micrographs of samples taken after the indicated dialysis times. The T = 3 capsids in the 0.5 h image are indicated with arrows. Scale bars correspond to 20 nm.

The number of T = 1 structures decreases and the amount of T = 3 structures increases in parallel, which points at stronger attractive interactions between CPs in the native species at low pH. Our curve fits in Figure 3.3C for times up to 168 h give $g_1 = -15.0$ and $g_3 = -15.4$ in thermal energy units. Again we find that the free subunit concentration very quickly becomes more or less constant: The disassembly of T = 1 shells produces dimers that are used for the formation of T = 3 shells.

From Figures 3.2B,C and 3.3B,C, it appears that T = 3 capsids easily dissociate at pH 7.5, crossing the growing fraction of T = 1 capsids after 6 h, while the disassembly of T = 1 CPs at pH 5.0 is much slower, crossing the growing fraction of T = 3 capsids

only after 48 h. This is expected because the smaller size of a T = 1 capsid produces fewer subunits per disassembled shell. ELPs are positioned closer next to each other because of the higher curvature of T = 1 shells, and the interaction between ELPs remains strong at pH 5.0.

3.3.3 Protein exchange between capsids of different size

We showed results of the fraction of proteins in the two types of capsid, f_T, as we find this the most informative. Alternatively, we can also calculate the fraction of dimers

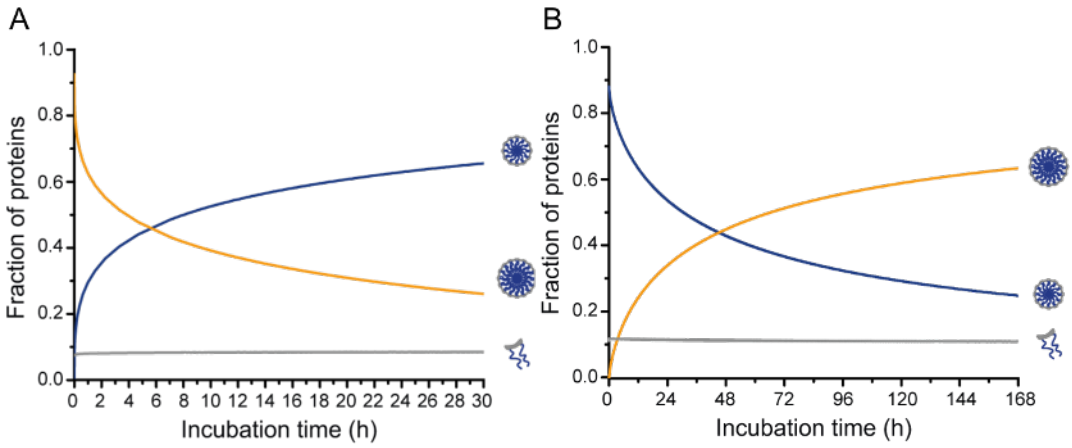

Figure 3.4: The fraction of protein in T=1 (blue line) and T=3 (yellow line) and dimer (gray line) over the total amount of protein in the solution (h_T) for the experiments showing A) disassembly of T=1 (represented in the Figure 3.3) and B) disassembly of T=3 (represented in the Figure 3.2). Refer to Tables 3.1 and 3.2 for the parameter values.

in one type of capsid relative to the total number of dimers in solution, $h_T = \frac{q_T x_T}{c_s}$, where T=1,3 is as before the T number of the capsid and c_s the overall dimer concentration in solution. Our simulations show that for our choice of parameters the concentration of dimers remains constant during the process (see Figure 3.4), implying that the increase in

the protein fraction in capsids is not due to the assembly of the free dimers initially present in the solution. This agrees with what is seen in the experiments [5]. This supports the proposed idea that one capsid size undergoes disassembly, resulting in the formation of free dimers. Subsequently, these free dimers reassemble to create the other capsid size. The fraction f_T plays a critical role in describing the assembly and disassembly kinetics for the problem at hand.

3.3.4 Model robustness with respect to different reference points

We have calibrated the simulation results using a reference point in the data series, as mentioned in the caption for Figures 3.2C and 3.3C. Here we re-calibrated the same

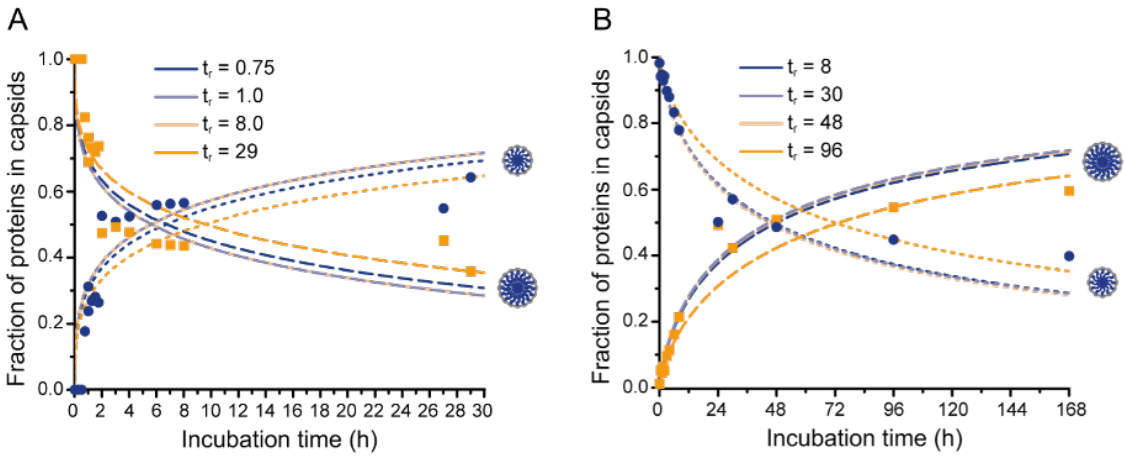

Figure 3.5: The fraction of protein in capsids (f_T as described in Equation 2.8) of T=1 (short dashed lines) and T=3 (long dashed lines) for A) disassembly of T=3 (represented in the Figure 3.2) and B) disassembly of T=1 (represented in the Figure 3.3) experiments, using different reference times. See Tables 3.1 and 3.2 for parameter values.

simulation data set with respect to a number of reference points to verify the robustness of our fitting procedure. We find that the curve fits depend only relatively weakly on the choice

of reference point (Figure 3.5). Unfortunately, our numerical implementation of Classical Nucleation Theory does not allow us to find the fundamental time scale, that is, the time scale associated with the attempt frequency. In spite of this, we are able to show that the disassembly and assembly of the two different capsid sizes can be explained by CNT.

3.4 Conclusions

In this context, we note that under specific conditions, the association and dissociation of empty capsids exhibit hysteresis. This means that the process of capsid assembly is more favorable or easier compared to the disassembly process [35]. Hence, assembled capsids can be significantly more stable kinetically than they are thermodynamically, implying that the height of the free energy barrier must be larger for disassembly than it is for assembly [4, 36]. Both the experimental findings and our theoretical calculations concur that the disassembly step serves as the rate-limiting factor in the conversion of unstable capsid shells into stable shells of different sizes.

In conclusion, our investigations demonstrate that ELP-CPs can undergo reversible switching between T = 1 and T = 3 structures in response to changes in solution conditions. While we acknowledge the possibility of other models explaining these experimental observations, notably, the interconversion between the two structures can be accurately described, particularly during the initial and intermediate timeframes, by CNT. At pH 7.5, the driving force for the assembly of coat proteins is the interaction between the ELPs, while at pH 5.0 the attractive interaction between capsid proteins predominates over the attractive ELP–ELP interactions. Since ELPs are attached to the capsid proteins, the ELP-CCMVs

do form a shell at pH 7.5, but only the smallest possible one as the ELPs need to be as close as possible to each other to make contact. This insight is of importance not only for a more fundamental understanding of virus assembly but also for the improved design of VLP-based nanomedicines.

3.5 Table of parameters

All parameters related to the simulation of disassembly of T=3 and assembly of T=1, and vice versa, discussed in the main text and used in our comparison with the experiments are tabulated below.

parameter	**Value(unit)**	**Description**
g_1	$-15(k_BT)$	Binding energy of T=1 capsids
g_3	$-14.7(k_BT)$	Binding energy of T=3 capsids
q_1	30	Number of dimers in fully formed T=1
q_3	90	Number of dimers in fully formed T=3
$x_s(t=0)$	$0.8c_1^*$	Initial dimer concentration
$x_1(t=0)$	0	Initial T=1 concentration
$x_3(t=0)$	$1/9c_1^*$	Initial T=3 concentration
ν^*	$1(a.u.)$	Critical attempt frequency
s	0.3	fraction of bonds at the rim
t_r	$4(hours)$	Reference time

Table 3.1: Parameters used in simulation of disassembly of T=3 and assembly of T=1

parameter	**Value(unit)**	**Description**
g_1	$-15(k_BT)$	Binding energy of T=1 capsids
g_3	$-15.4(k_BT)$	Binding energy of T=3 capsids
q_1	30	Number of dimers in fully formed T=1
q_3	90	Number of dimer in fully formed T=3
$x_s(t=0)$	$1.3c_3^*$	Initial dimer concentration
$x_1(t=0)$	$1/3c_3^*$	Initial T=1 concentration
$x_3(t=0)$	0	Initial T=3 concentration
ν^*	$1(a.u.)$	Critical attempt frequency
s	0.3	fraction of bonds at the rim
t_r	$48(hours)$	Reference time

Table 3.2: Parameters used in simulation of disassembly of T=1 and assembly of T=3

Chapter 4

A multiscale chemical-mechanical model predicts impact of morphogen spreading on tissue growth

This results were published [37]. I have contributed to this work in the formal analysis, investigation, software developing, and visualizations.

4.1 Introduction

Understanding mechanisms underlying proper tissue growth and shape formation in an embryo is among the most important unanswered questions in developmental biology.

The growth of tissues and organs always exhibits the property of self-organization, with precise control of cell proliferation resulting in robust tissue size and specific shape as integrity. This process also stays robust under external perturbations as observed in wound healing and tissue regeneration [38, 39, 40, 41, 42, 43]. Uncontrolled cell growth and cell division often lead to abnormal development or fatal diseases such as cancer.

During tissue development, chemical signals are found to be critical to the regulation of cell proliferation and tissue shape formation. A variety of molecules, from extracellular ligands to intracellular proteins, have been identified as growth regulators in different biological systems. For example, transforming growth factor Beta ($TGF-\beta$), a member of the growth factor superfamily, has been found to regulate the growth in multiple animal organs [44, 45]. In particular, bone morphogenic proteins (BMP) are members of the $TGF-\beta$ family and play essential roles in establishing the basic embryonic body plan for tissue development in vertebrates [46, 47, 48, 49, 50]. Disruption of BMP signals can affect the growth rate and pattern formation, leading to disorders in adult tissues [51, 52]. On the other hand, in addition to the central core of the growth control machinery, which depends on chemical cues, cell mechanics play a fundamental role in shaping a tissue [53, 54, 55, 56, 57, 58, 59, 60]. Each cell has a complex mechanical architecture that not only shapes itself as integrity but also allows it to sense the physical surroundings and make responses. For example, cytoskeletal tension in one cell can be affected by differential growth associated with neighboring cells and modulate intracellular molecular signals to regulate growth as feedback [61]. Cell deformation can be induced by mechanical forces such as the adhesion to the extracellular matrix (ECM), contractility in the cytoskeleton,

and cell–cell adhesion, which may also lead to physical changes of nuclei and an alteration in gene expression to switch cell fate between growth, differentiation, and apoptosis [62]. Therefore, it is necessary to consider both chemical signals and mechanical properties, as well as the interplay between them, to understand the general principles involved in tissue development.

Drosophila wing disc, a primordial epithelial organ that later becomes the adult wing, as shown in Figure 4.1A, serves as a classic model to study tissue growth regulation due to its simple geometry, the limited number of cells, and fast growth. Additionally, the well-established molecular signaling network involved in this tissue contains multiple conserved molecules critical to other developing systems in mammals [45]. Understanding the mechanism of growth regulation in the *Drosophila* wing disc is substantial in understanding limb development in mammals. In this tissue, Decapentaplegic (Dpp), a homolog of BMP, forms a spatial gradient across the anterior-posterior (AP) axis of the tissue to establish and maintain domains of multiple target genes that specify different compartments in the adult tissue (Figure Figure 4.1B, C). For individual cells, a signal transduction cascade converts local concentrations of Dpp into intracellular phosphorylated MAD (pMAD) through binding with receptors on the membrane. pMAD protein is also commonly observed in other systems and related to several cancers in humans [44]. Based on the level of pMAD, different genes are activated along the AP axis of the imaginal wing disc to establish the pattern and regulate growth. In terms of mechanical properties, a wing disc consists of a flat sheet of cells with E-cadherin responsible for cell–cell adhesion between neighboring cells. Inside individual cells, actomyosin is dynamically rearranged to give rise to different

levels of contractility, which links to multiple cellular functions, including nuclear motion during mitotic rounding (Figure 4.1D) [63] and vesicle trafficking [64, 65]. Moreover, actin networks in the cytoplasm, as a major component of the cytoskeleton, provide structural support to each cell and determine cell shapes together with the cytoplasm. More recently, it has been observed that chemical signals can affect cell mechanics by directly controlling the subcellular distribution of the small GTPase Rho1 and the regulatory light chain of non-muscle myosin [66]. Dpp signal promotes the compartmentalization of Rho1 and myosin, which leads to the contraction of actomyosin filaments and an increase in cortical tension. This suggests the interaction between chemical signals and mechanical properties also plays an important role in shaping cells and, therefore, the overall tissue shape.

Several hypotheses regarding growth regulation in the wing disc tissue have been proposed so far. Substantial data suggest that Dpp morphogen is pivotal in regulating growth; however, the underlying mechanism remains controversial and uncertain. In Wartlick *et al.* [67], it was suggested that cells have memory and will divide if the temporal change of the Dpp signal reaches a certain threshold value. In contrast, recent experiments have shown that a Dpp signal is not always required for growth since removing Dpp from the center of the tissue at some stage during the development does not affect the growth [68]. On the other hand, mechanical properties have been shown to be critical in regulating growth based on measurements of cell stress in experiments [61].

Many computational models have been developed to study tissue growth in different biological systems, including cell lineage in epithelia [69, 70, 71, 72] and tumor growth [73, 74, 75]. To include chemical signaling networks, it is common to use continuous models

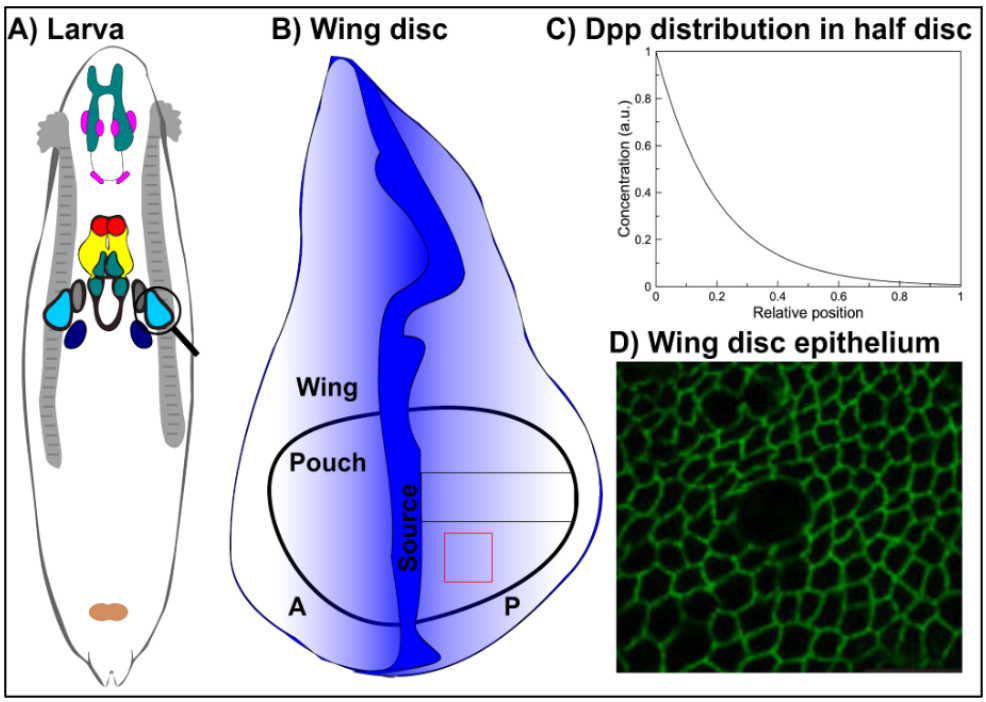

Figure 4.1: A) Diagram of *Drosophila* larva with wing disc tissue circled. B) Illustrative diagram of the *Drosophila* imaginal wing disc. The blue color denotes the Dpp morphogen gradient. C) Schematic profile of the Dpp morphogen in half wing disc. Its distribution follows an exponential shape, as observed in experiments. D) Configuration of epithelial cells in the wing disc pouch. The image has been reproduced from Gibson *et al.* [63]

in which the dynamics of chemical signals are captured by a system of differential equations. This kind of approach usually involves moving boundary problems for capturing tissue growth that are challenging to solve numerically. It can be overcome by using Lagrangian coordinates [76], immersed boundary method [77], level set method [78], or other similar approaches. To include cell mechanics, some models use discrete particles to represent individual cells, which allows one to model cell growth, cell division, and cell–cell interaction. More specifically, each cell can be represented by a single particle (agent-based model) [79], multiple particles on the cell membrane (multi-agent-based model) [80], a polygon (vertex-based model) [58, 67, 81, 82], or multiple particles on the cell membrane and in the cytoplasm (subcellular element method) [83]. In particular, multi-agent-based models and subcellular element models can describe biologically relevant cell shapes with greater flexibility due to the multiple nodes involved. Another type of model is based on the finite element framework, coupled with continuum mechanics principles [84, 85, 86, 87]. Models of this type focus more on tissue growth without subcellular details. Most existing models for studying tissue growth focus on either chemical signals or mechanical properties only. As suggested by recent experimental data, exploring mechanisms involved in tissue growth regulation requires a model that includes both chemical and mechanical factors, as well as the interactions between them.

Several coupled chemical-mechanical models have been developed recently and gained lots of attention. In Aegerter-Wilmsen *et al.* [88], both chemical signals and mechanical cues were considered. However, fixed morphogen gradients were adopted without considering the temporal dynamics or subcellular activities. Vertex-based models have been

coupled at the cell level with diffusive molecules [89] or intracellular gene expression [44, 45] to study tissue development. The subcellular element model has also been coupled with chemical signals without distinguishing cell membrane and cytoplasm [90, 91]. Those existing models provide novel insights into growth regulation in different systems. As far as we know, very few of them consider subcellular details and the interaction between chemical signals and mechanical forces, which is critical in the regulation of individual cell behavior and tissue growth.

Here we developed a multiscale coupled chemical-mechanical model where the mechanical submodel describes cell mechanical and adhesive properties at the subcellular and cellular levels, and the chemical signaling submodel describes both morphogen gradient at the tissue level and the intracellular gene regulatory network at the cellular level. This model was then applied to study growth regulation in *Drosophila* wing imaginal disc. In addition, we incorporated a cell division rule proposed in Wartlick *et al.* [67], in which cells enter the mitotic phase and divide when the Dpp signal is increased by 50% compared with that at the beginning of the cell cycle in individual cells. Following this hypothesis and including cell mechanical properties, morphogen gradients with different decay lengths were tested in the model to simulate tissue growth. We found that a morphogen gradient with a larger decay length maintained the tissue growth longer, resulting in a more symmetric shape at a more spatially homogeneous growth rate, which was consistent with experimental observations. Together with the assumption of an absorbing boundary condition, feedback regulation of the downstream signal to inhibit the synthesis of cell membrane receptors facilitated tissue growth by indirectly expanding the spread of the morphogen gradient.

Although the chemical-mechanical model was only applied to studying the growth regulation of *Drosophila* wing disc, it can be applied to simulate tissue growth and test hypotheses on growth regulation involved in other epithelial tissues.

4.2 Results

We developed a two-dimensional chemical-mechanical model for studying tissue development and applied it to explore the growth regulation mechanism in the *Drosophila* wing disc. In particular, we aimed to understand how spatially uniform growth can be achieved and maintained throughout tissue development, as observed in experiments. [37]

4.2.1 Multiscale chemical-mechanical model of tissue development in two dimensions

During tissue development, both chemical signals and mechanical forces play essential roles in regulating cell growth. We have introduced a multiscale model to integrate both chemical and mechanical factors and the interactions between them at the subcellular level (see Figure 4.2). This chemical-mechanical model employs a subcellular element particle-based method for the mechanical submodel and a system of differential equations as the submodel for chemical signals coupled both in space and time. Details of each submodel are provided in "Methods". In what follows, we briefly describe the coupling of submodels.

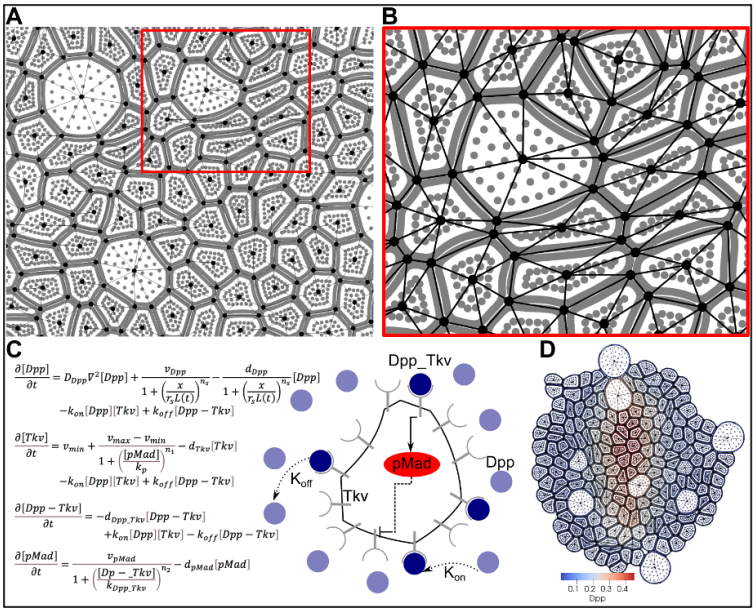

Figure 4.2: A) Triangular mesh over the nodes obtained in the mechanical submodel. B) A zoom-in view of the triangular mesh within the red box indicated in (a). C) Mathematical model (left) and a schematic diagram (right) of the chemical signaling network in a single cell of *Drosophila* wing disc. D) Discretized tissue with Dpp gradient, denoted by blue-red color, obtained in the chemical-mechanical model.

4.2.2 Spatial coupling of mechanical and chemical submodels

The spatial coupling of the chemical signaling submodel and the mechanical submodel is achieved by adopting a dynamic triangular mesh over individual cells as well as the entire tissue. Such dynamic mesh is constructed using discrete nodes representing cell membranes obtained in the mechanical submodel (Figure 4.2A). Shared edges and junction points between neighboring cells are identified as the edges and vertices of triangles, respectively (Figure 4.6). Together with cell centers, they give rise to a triangular mesh covering individual cells (Figure 4.2A, B) (More details about this mesh generator are provided in "Methods"). The chemical signaling submodel in the form of Eqs. 4.4–4.7 is then simulated over the latest mesh to reach the steady state, using an initial condition based on the old Dpp levels from the last update of the chemical signaling submodel in individual cells (Figure 4.2C). Distributions of chemical signal concentrations are obtained at both individual cells and tissue level (Figure 4.2D). Meanwhile, cell averages of the chemical signals are used in the mechanical submodel to direct cell growth and division.

4.2.3 Temporal coupling of mechanical and chemical submodels

Cell growth and division are initiated and regulated by chemical signals. Moreover, the dynamics of chemical signals are at a much faster time scale than the time scale of mechanical changes. Therefore, quasi-steady states (Figure 5.1) of chemical signaling distributions are computed over the dynamic mesh, which captures cell and tissue deformation, and are transmitted into the mechanical submodel at some frequency. This frequency was chosen to limit redundant computation and unnecessary computational cost, as well as

to transmit accurate distributions of chemical signals to the mechanical submodel. In our model, the change in the chemical signaling distribution depended on the deformation of individual cells. Therefore, to couple two submodels in time, we estimated the average time that one cell takes to enter the mitotic phase and divide. It was then converted into the frequency to update the quasi-steady state of chemical signaling distribution over the domain based on the most recent tissue configuration (More details are provided in " Methods").

The multiscale chemical-mechanical model can be applied to study tissue development and investigate mechanisms underlying growth regulation in different biological systems. In what follows, we calibrate the model and use it to study the development of *Drosophila* wing disc pouch tissue.

4.2.4 Calibration of the model for the development of *Drosophila* wing disc pouch

Dpp morphogen is the primary signal controlling cell growth and tissue development in *Drosophila* wing disc pouch [66, 67, 92, 93, 94, 95, 96, 97, 98, 99]. In individual cells, the Dpp molecule binds with its receptors, Thickvein (Tkv), on the cell membrane to form the complex phosphorylates MAD (pMAD) as a downstream signal (Figure 4.2C). Experimental data also suggested pMAD represses the production of Tkv as a negative feedback regulation [43], leading to a lower synthesis of Tkv near the Dpp source region.

In the multi-scale model, dynamics of the morphogen and the intracellular signaling network are modeled by a system of reaction-diffusion equations as shown in Figure 4.2D. Parameters d_*'s represent degradation rates and v_*'s represent production rates. v_{min} and v_{max} are the minimum and maximum production rates of Tkv receptors. The production

of Dpp is modeled as a Hill function of the distance to the Dpp production region located at the AP boundary. Half of the tissue width is denoted as $L(t)$ and the width of the Dpp production region is denoted as $r_s L(t)$, where r_s is a constant calibrated using experimental data [43]. The activation of intracellular signal pMAD by the binding complex Dpp-Tkv is also modeled by a Hill function, so is the negative feedback regulation of pMAD on Tkv.

We applied a hypothesized cell division rule proposed in Wartlick *et al.*, 2011 [67] assuming that cells divide when the level of Dpp signal is increased by 50% compared with that at the beginning of each cell cycle, i.e., $\frac{[Dpp]-[Dpp_{Div}]}{[Dpp_{Div}]} \geq 50\%$, where $[Dpp]$ is the Dpp concentration at the current time and $[Dpp_{Div}]$ is the concentration at the beginning of one cell cycle. This hypothesis, also known as the temporal model, assumes that cells have a memory to keep track of Dpp level throughout the cell cycle and they divide once its relative change gets sufficiently large. Therefore, in our model cells have a constant growth rate during the interphase (Table 5.4), and they progress into the mitotic phase based on the division rule condition indicated above (Figure 4.5A). All other parameter values were provided in Table 5.2 and Table 5.3. This model can be easily revised to incorporate any other cell division rule.

4.2.5 Morphogen absorbance at the tissue boundary and large decay length prolong tissue growth at a fast and spatially homogeneous rate

Dpp is generated along the midline of the wing disc and diffuses bilaterally into the neighboring tissue. Therefore, it forms an exponentially shaped gradient along the AP axis (Figure 4.1B). To characterize the Dpp gradient, it is common to use a quantity called

decay length (λ), which measures the distance from the source region to the location where the Dpp level is reduced to $e^{-1} \approx 37\%$ of its maximum (see section 5.2 for more details) [43]. A greater decay length represents a further spread of the exponential morphogen gradient. The experimental data revealed that ubiquitous expression of Tkv led to a smaller decay length of the Dpp gradient, followed by a slower growth and smaller tissue size [43]. This observation suggests that the spatial distribution of morphogen gradient should play an important role in regulating tissue growth.

To understand how the distribution of the Dpp gradient affected tissue growth, we first used a simplified chemical submodel by ignoring intracellular processes and downstream signals in the form of Equation 4.3 provided in "Methods". This simplified model allowed us to perturb the shape of the gradient easily through tuning one parameter only. In particular, the source term (second term on the right-hand side of Equation 4.3) is specified as $v_{Dpp}/[1+(\frac{x}{r_s L(t)})^{n_s}]$ to represent the synthesis of Dpp molecules along the midline, where v_{Dpp} , r_s, n_s are constants and $L(t)$ denotes half of the tissue width. Moreover, the decay length of Dpp in this simplified model can be analytically estimated as $\lambda = \sqrt{D_{Dpp}/d_{Dpp}}$ (See section 5.2 for details), depending on the diffusion rate and degradation rate. A higher diffusion rate or lower degradation rate allows diffusing molecules to travel further, giving rise to a larger decay length. Both diffusion and degradation rates were calibrated to achieve a similar decay length observed in experiments [43]. We then coupled this simplified chemical submodel with the mechanical submodel under the specific cell division rule to simulate tissue growth. All simulations started with 100 cells (Figure 4.3A). The final shapes of simulated tissue development are shown in Figure 4.3A', B-C. To understand how the

decay length could affect tissue growth, we varied the degradation rate of Dpp concentration, which changed the underlying decay length under different boundary conditions.

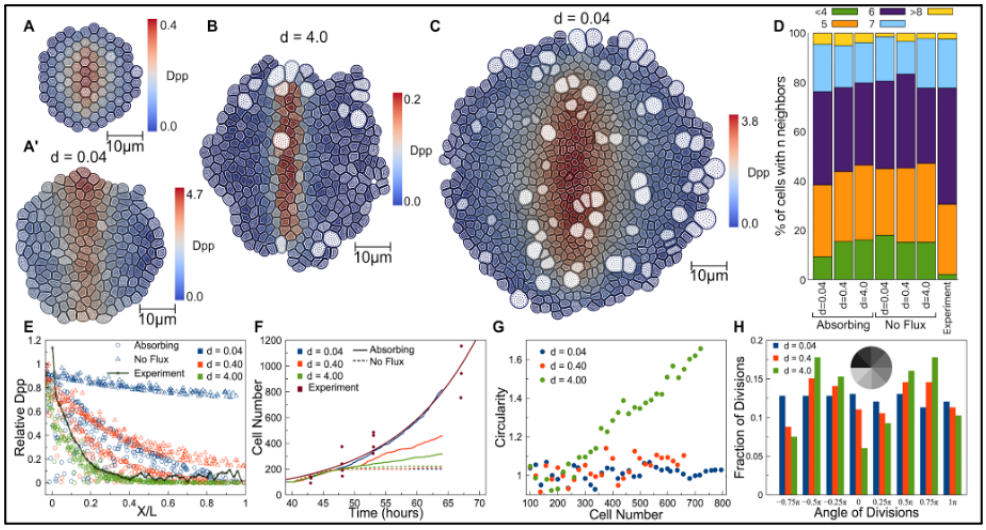

Figure 4.3: A) Initial configuration of the tissue in simulations. Final configuration of the tissue at t=200 with A') no flux boundary condition, B) absorbing boundary condition with a large degradation rate of Dpp, and C) absorbing boundary with a small degradation rate of Dpp. The scale bar in (A–C) is 10 μm. D) Percentage of cells having n number of neighbors for simulations and experimental results. E) Normalized Dpp profile at t=200 with respect to the relative cell position in the tissue under different boundary conditions and with different degradation rates of Dpp. The black line shows fitted experimental quantification of the relative Dpp concentrations from 48 to 130 h. F) Cell numbers with respect to time for different degradation rates and different boundary conditions. G) Tissue circularity with respect to the cell number for different degradation rates. Circularity was defined as the ratio of tissue height over tissue width. H) Distribution of the angular position of dividing cells with respect to tissue center for different degradation rates when there are 500 cells in the tissue.

First, we considered the scenario that free Dpp molecules cannot escape at the boundary of the wing disc pouch and are always kept within the tissue. This was modeled by no flux boundary condition associated with cells located at the tissue boundary. For tissue growth with no flux boundary condition, smaller degradation resulted in a flatter Dpp gradient (red and blue triangles in Figure 4.3E). The Dpp concentration was saturated

at high levels in individual cells, and it did not increase sufficiently to satisfy the cell division rule at the early stage of development. Therefore, most cells only experienced one cell cycle, and tissue growth stopped at the early stage, leading to small tissue sizes (red and blue dash line in Figure 4.3F). With a larger degradation rate, the Dpp gradient became more exponential (green triangles in Figure 4.3E), which was still far from the experimental profile of Dpp [67] (black crosses in Figure 4.3E) and the final tissue size obtained was slightly increased (green dash line in Figure 4.3F). However, tissue growth was still terminated early, and the overall tissue size was much smaller than that obtained in experiments (Figure 4.3F). Therefore, by assuming Dpp molecules could not escape at the boundary, tissue growth only occurred in a short time period at the early stage, and small final sizes were always obtained for different decay lengths of Dpp.

Second, we considered the scenario with Dpp being completely degraded at the periphery zone of the tissue (see "Methods" for more information), which was modeled by using absorbing boundary conditions for cells at the boundary of the tissue. Under these assumptions, the Dpp gradient changed from a linear shape to an exponential shape as the tissue size increased (indicated by circles in Figure 4.3E). Furthermore, by assuming absorbing boundary conditions, the tissue growth was able to reach a size greater than the decay length of Dpp gradient (indicated by solid lines in Figure 4.3F). We also observed that with a larger degradation rate, the morphogen gradient became exponential at a smaller tissue size, and the growth was maintained in a shorter period of time, giving rise to a smaller tissue size (see solid green line in Figure 4.3F). With a smaller degradation rate, the morphogen gradient became exponential at a larger tissue size (blue circles in Figure 4.3E)

and it was still in a good agreement with experimental data [67] (black crosses in Figure 4.3E). In addition, the growth was maintained for a much longer time (Figure 4.3F). To compare our simulated tissue size with experimental data more carefully, we found the time in simulations when a similar cell number was obtained as that at the initial time point and the last time point in the experiments of Wartlick *et al.* [67]. Then we scaled the simulation time accordingly to match those two time points and compared the cell number at intermediate time points. The simulated tissue growth matched experimental data best with the smallest degradation rate (Figure 4.3F). These results were consistent with the experimental observations of a larger decay length of the Dpp, giving rise to larger tissue sizes [43].

In addition to limited growth, it was also shown that with a higher degradation rate, the overall shape of the growing tissue, which was symmetric initially (Figure 4.3A), became asymmetric, and the boundary became less smooth under the absorbing boundary condition (Figure 4.3B). To look into this further, we tracked in model simulations the spatial locations of all dividing cells and visualized the distribution by dividing the tissue into eight sectors of equal size (Figure 4.3H). It was observed that a higher degradation rate led to more dividing cells near the production region of Dpp, hence faster tissue growth along the AP boundary. As a result, the height of the tissue grew faster than the width, yielding an asymmetric shape (Figure 4.3G). In contrast, a smaller degradation rate gave rise to more spatially homogeneous cell division (Figure 4.3H) and a more symmetric overall tissue shape (Figure 4.3G). Indeed, the spatially homogeneous growth rate was also observed in experiments of *Drosophila* wing disc pouch [67, 100, 101, 102, 103, 104], suggesting larger

decay length of Dpp might be beneficial to achieve homogeneous growth in a wild-type wing disc pouch tissue. We also measured the number of neighboring cells throughout the simulated tissues with different boundary conditions and different degradation rates and compared them with experimental data (Figure 4.3D). In all cases, most cells had five or six neighbors, similar to the experimental observations. With the smallest degradation rate and absorbing boundary condition, the cell population with less than four neighbors was the smallest, which was most consistent with experimental data.

Overall, simulation results suggested that the decay length of the morphogen played an essential role in maintaining tissue growth and determining the final shape when absorbing boundary condition is applied. Under such boundary conditions and the specific cell division rule, Dpp distribution with a larger decay length helped a tissue grow longer, faster, and in a more spatially homogeneous manner, which closely resembled the shape of the wild-type wing disc pouch observed in experiments. The absorbing boundary condition with a lower degradation rate allowed Dpp molecules to travel further to establish a gradient with a larger decay length, while no flux boundary condition gave rise to relatively high concentrations everywhere and much smaller tissues. In fact, the specific cell division rule was less frequently satisfied under no flux boundary conditions (see Figure 5.2 for details). In fact, it was observed that due to the hinge region around the wing disc pouch, the Dpp level dropped to almost zero at the tissue boundary [43], suggesting the absorbing boundary condition was more biologically relevant. Therefore, the morphogen absorbance at the peripheral zone also facilitated tissue growth by reshaping the morphogen gradient in a wild-type wing disc.

4.2.6 Negative feedback regulation on the synthesis of receptors promotes tissue growth through increasing morphogen decay length

It was previously shown that the transduction of Dpp signals into cells in the *Drosophila* wing disc relies on a receptor kinase Tkv. Removal of Tkv had a similar effect as the Dpp mutant. Recently, it was also observed that the intracellular downstream signal pMAD downregulates the production of Tkv as a negative feedback regulation, which may reshape the morphogen gradient to some extent. [43] Next, we applied our coupled model with absorbing boundary condition to study the effects of this feedback regulation on tissue growth.

Notice that in the chemical submodel, the negative feedback regulation of pMAD on Tkv was modeled using a Hill function, as illustrated in Figure 4.2C. In particular, the parameter k_p denoted the effective level of pMad involved in negative feedback regulation. Therefore, in simulations, we perturbed k_p to give rise to different levels of this feedback regulation. Higher k_p values gave rise to weaker negative regulation in a smaller region, while lower k_p values led to stronger negative regulation in a larger domain. The cell division rule involved in the coupled model depended on the intracellular signal pMAD.

Simulations were run for low ($k_p = 10$), medium ($k_p = 1$), and high ($k_p = 0.1$) strength of negative feedback, as well as different values of maximal Tkv receptor production rate (v_{max}) (Figure 4.4). All simulations showed a good match with experimental data on the number of neighboring cells throughout tissues (Figure 4.4D). The simulation results showed that, with stronger strength of negative feedback of pMAD, i.e., lower values of k_p, the tissue grew faster and the profile of cell number growing over time was closer to the one

obtained in experiments (Figure 4.4F, F') and the overall tissue shape was more symmetric (Figure 4.4G, G'). Moreover, the spatial distribution of dividing cells was more homogeneous (Figure 4.4H, H'). However, it was also observed that simulation results for $k_p = 0.1$ and 1 were similar to each other. This was because the production rate of Tkv became close to the minimum almost everywhere within the tissue for sufficiently small k_p. Hence, the pMAD gradient remained more or less the same for sufficiently small k_p values. By comparing the results generated using different values of the maximal receptor production rate ($v_{max} = 10$ v.s. 20), it was observed that the effect of the feedback regulation strength became more significant when v_{max} was larger, i.e., the difference in the circularity of tissue shape due to different strength of the negative feedback regulation became more visible (Figure 4.4G, G').

In fact, stronger negative feedback regulation of pMAD on Tkv receptors allowed Dpp molecules to diffuse into a larger area by reducing the binding occurrence near the Dpp production region, and therefore it gave rise to a pMAD gradient with a larger decay length (Figure 4.4E, E'). Based on the cell division rule used in this study, depending on temporal changes of the Dpp signal, a more widely spreading morphogen gradient helped maintain the tissue growth for a longer time and keep the cell number increasing linearly at a faster rate, leading to a larger tissue size and more symmetric shape. This was also consistent with the results obtained by using the simplified chemical submodel (Equation 4.3), in which decreasing the degradation rate led to a larger tissue size and more spatially homogeneous cell division.

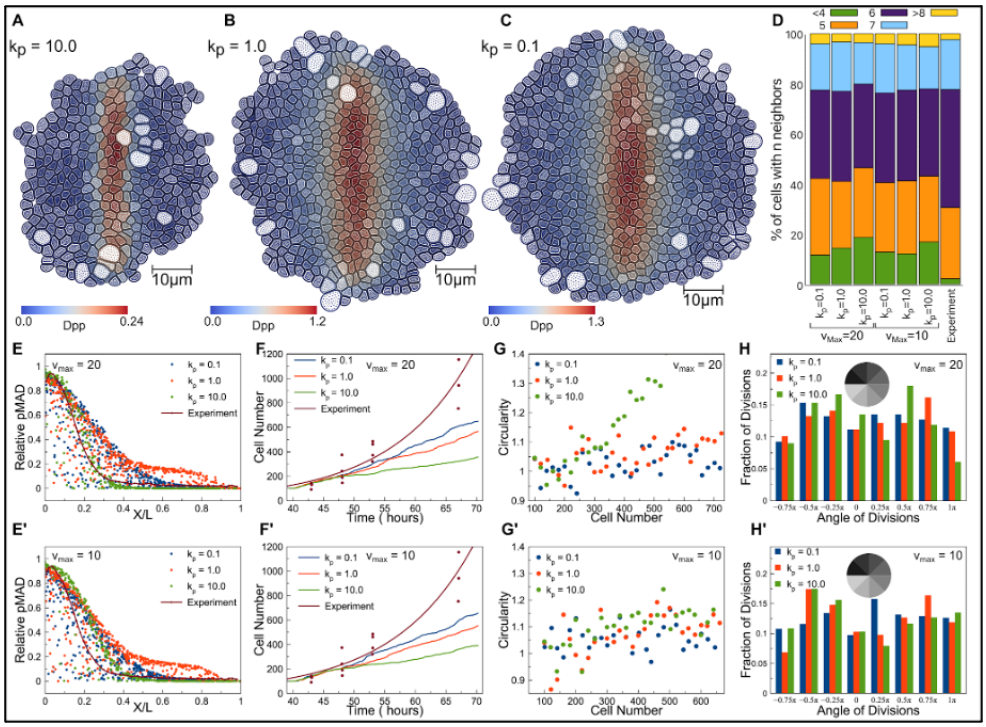

Figure 4.4: Tissue configuration at t=250 for $v_{max} = 20$ with A) $k_p = 10.0$ B) $k_p = 1.0$ and C) $k_p = 0.1$. The scale bar in (A–C) is $10\mu m$. D) Percentage of cells having n number of neighbors for simulations and experimental results. pMAD profile at t=250 with respect to the relative cell position in the tissue with different levels of feedback regulation and E) $v_{max} = 20$ and E') $v_{max} = 10$. The black line represents fitted experimental quantification of the relative signal concentrations from 48 to 130 h. Cell numbers at different levels of feedback regulation over time for F) $v_{max} = 20$ and F') $v_{max} = 10$. Tissue circularity with respect to cell number for different levels of feedback regulation for G) $v_{max} = 20$ and G') $v_{max} = 10$. Distributions of the angular position of dividing cells with respect to the tissue center for different levels of feedback regulation and H) $v_{max} = 20$ and H') $v_{max} = 10$ when there are 500 cells in each simulation.

4.3 Discussion

Here we described a multiscale chemical-mechanical model to study growth regulation involved in tissue development and applied it to study the development of the *Drosophila* imaginal wing disc at the larva stage. The mechanical submodel represents the shape change of individual cells and cell–cell physical interactions. It is coupled with a chemical submodel by utilizing an adaptive mesh generated over the growing tissue domain. This chemical signaling submodel describes the dynamics of the morphogen gradient and associated downstream signals inside individual cells, which control cell growth and division in the mechanical submodel. A hypothesized cell division rule based on the morphogen concentration sensed by individual cells is applied to study how the decay length of the morphogen gradient affects tissue growth.

By applying different boundary conditions in the chemical submodel, we found that tissue growth was maintained longer under absorbing boundary conditions. This indicates that the significant reduction of morphogen at the hinge region surrounding a wing disc tissue, as observed in experiments, could better promote tissue growth, compared with the case of the hinge region being a simple obstacle and preventing morphogen spread. By varying the decay length of the morphogen gradient, it was also shown that the tissue grew faster with a greater decay length. Moreover, cell division became more spatially homogeneous, giving rise to a more symmetric tissue shape consistent with experimental observations. We also found that the feedback regulation of pMAD, a downstream signal of the morphogen, on the synthesis of receptors increased the decay length and therefore facil-

itated tissue growth. Overall, these results suggest that the decay length of the morphogen gradient can play an important role in the growth regulation of the wing disc.

In this study, we tested a hypothesized cell division rule based on the temporal changes of morphogen, which was proposed in Wartlick *et al.* [67]. However, this chemical-mechanical model provides a general framework to study growth regulation of epithelial tissue, and it can be used to investigate other hypothesized mechanisms of growth regulation. For example, it was shown that cell mechanical stress contributes to growth control through a feedback loop in the wing disc [60, 100, 102], known as the integral-feedback mechanism, which might help to achieve a more uniform growth rate in the presence of an exponential morphogen gradient. In addition, it demonstrated that cytoskeletal tension could regulate growth by altering the Hippo pathway directly [61], working as an interaction between chemical signals and mechanical properties at a subcellular scale. Therefore, the multiscale model developed in this study can be extended to implement cell growth rate in the form of a function of both cellular mechanical properties and chemical signals.

Moreover, it was suggested that some signaling pathways could be affected by cell mechanical properties, including shear stress and tension sensed at adherens junctions [105, 106, 107]. Meanwhile, signaling molecules could rearrange structural components within individual cells and direct new materials to the cell membrane to modify the mechanical properties [66]. These interactions between chemical and mechanical components can be incorporated into the multiscale model as more detailed experimental quantification is provided. Also, in this study, the subcellular scale was mostly used in the mechanical submodel to describe cell growth and introduce mechanical properties. Although we calcu-

lated the distributions of chemical signals over a mesh with subcellular partitioning, only cell-based averages were used to regulate cell division. However, this spatial mesh with subcellular partitioning benefited the simulation results in terms of accuracy compared with a cell-based mesh. It is also possible to apply this coupled model to study polarized chemical signals within individual cells and subcellular interaction between chemical signals and mechanical properties for other biological systems.

2D models are commonly used for studying the growth of the *Drosophila* wing disc pouch by neglecting the tissue thickness. This is because the wing disc pouch consists of epithelial cell layers, and the thickness is much smaller than the apical view dimensions. Also, the key structural components, such as E-cadherins and actomyosin, are concentrated on the top surface of the epithelia. These components contribute significantly to cell adhesion and contractility. In our 2D mechanical submodel, during cell division, the movement of the nucleus and a significant amount of cytoplasm added to the top surface of the cell, known as the process of mitotic rounding, are taken into account to include effects from the neglected dimension to some level. Additionally, a 2D model allows simulations with a large number of cells in a high resolution. As a future direction, we will try to extend our model into 3D to include extracellular matrix (ECM) and the interaction between ECM and cells, as well as intracellular signals distributed along the 3rd dimension regulating cell growth. The use of parallel computing and GPU clusters may enable 3D simulations at a similar resolution with more reasonable computational costs.

4.4 Methods

4.4.1 Mechanical submodel

For the mechanical submodel, we follow a similar approach as the Epi-scale model [83]. Epi-scale model is a multiscale subcellular element computational platform that simulates the growth of epithelial monolayers with detailed cell mechanics. Individual cells are represented as collections of two types of interacting subcellular nodes: internal nodes and membrane nodes. Internal nodes account for the cytoplasm, and the membrane nodes represent both the plasma membrane and associated contractile actomyosin cortex. Interactions between internal and membrane nodes are modeled by using different energy functions, as shown in Figure 4.5B [90, 108]. Combined interactions between internal nodes (E^{II}) represent the cytoplasmic pressure of a cell. Combined interactions between internal and membrane nodes of the same cell (E^{MI}) represent the pressure from the cytoplasm to the membrane. Interactions between membrane nodes of the same cell (E^{MMS}) represent cortical stiffness. Cell-cell adhesion (E^{Adh}) is modeled by combining pairwise interactions between membrane nodes of two neighboring cells. E^{MMD} is a repulsive force between membrane nodes of neighboring cells and prevents membranes of different cells from overlapping. Springs and Morse energy functions are utilized to model all the interactions [91]. The following equations of the motion describe movements of internal and membrane nodes, respectively:

$$\eta \dot{x}_i^I = -\left(\sum_j \nabla E_{ij}^{MI} + \sum_m \nabla E_{im}^{II}\right) \; i = 1, 2, \ldots..N^I{}_{(t)} \tag{4.1}$$

$$\eta \dot{x}_j^M = -\left(\sum_i \nabla E_{ij}^{MI} + \sum_k \nabla E_{kj}^{MMS} + \sum_l \nabla E_{lj}^{MMD} + \nabla E_j^{Adh}\right) \; j = 1, 2, ..N^M \tag{4.2}$$

where η is the damping coefficient, x_i^I and x_j^M represent positions of internal and membrane nodes. m is the index for any internal node. k is the index for any membrane node of the same cell interacting with the membrane node j. l is the index for any membrane node of a different cell interacting with the membrane node j. Cell growth is modeled by adding internal nodes, and therefore N^I increases based on cell proliferation rate. The individual cell cycle in the current model is shown in Figure 4.5A. Initial and final configurations of the tissue in a simulation with a given growth rate and cell division rate are shown in Figure 4.5C and Figure 4.5D,E, respectively.

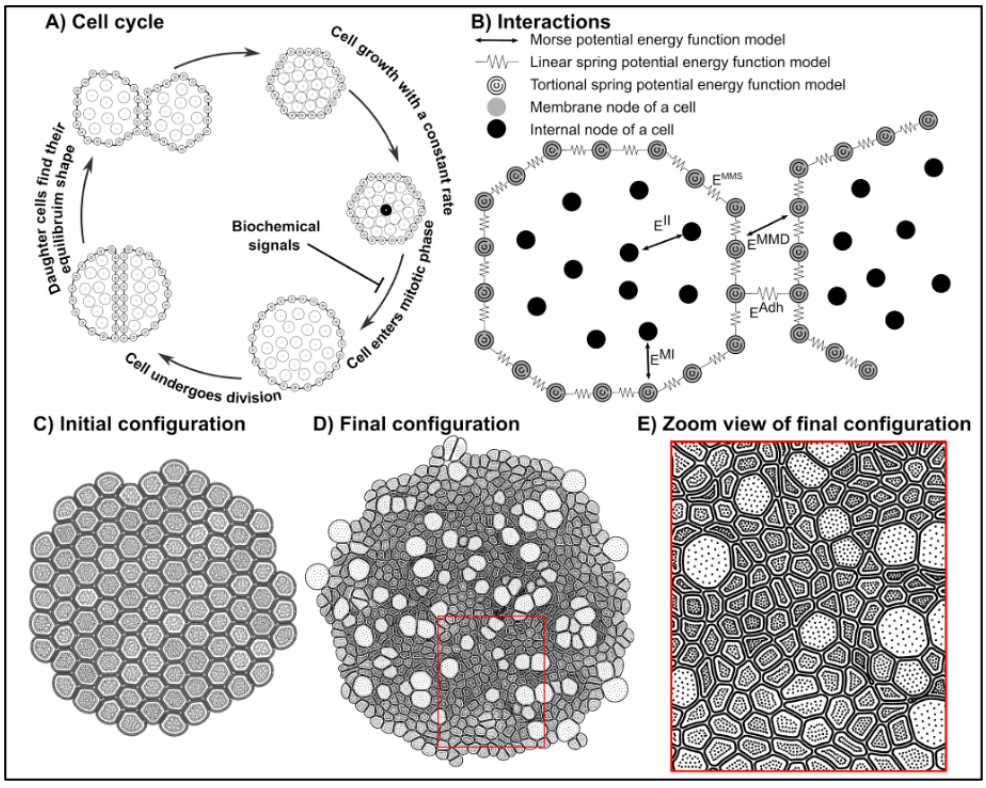

Figure 4.5: A) Life cycle of a cell in the mechanical submodel. B) Mechanical forces between different nodes in the mechanical submodel. C) Initial tissue configuration in a simulation with no growth regulations. D) Final tissue configuration from the simulation in (C). E) Zoom-in view of the final configuration.

4.4.2 Chemical submodel

In the chemical signaling submodel, we consider a chemical signal which regulates the growth rate and cell division. A morphogen, which is a signaling molecule governing the growth and patterning of tissue development, diffuses in the extracellular space to form a gradient at the tissue level. A reaction-diffusion equation is used to model the spatiotemporal dynamics as below:

$$\frac{\partial [M]}{\partial t} = D_M \nabla^2 [M] + s_M(x) - d_M [M] \tag{4.3}$$

where $[M]$ denotes the concentration of the morphogen molecules, D_M is the diffusion coefficient of morphogen molecules, and d_M is the degradation rate of morphogen molecules. The production rate of morphogen molecules, varying spatially, is denoted by $s_M(x)$. D_M and d_M together determine how far the molecules can reach in the steady state (See Table 5.2 –5.4 for more information). The local morphogen concentration is sensed by individual cells through binding with receptors on the cell membrane to activate the intracellular signaling network.

To model the intracellular signaling network, we consider the receptor R , the complex after binding MR, and a downstream signal S. More components with more complex regulations can be modeled similarly. Together with the diffusive morphogen, it gives rise to a chemical signaling network at both cell and tissue levels, formulated as Equations 4.4–4.7 below. More specifically, the binding of the morphogen molecules and receptors is reversible, so both binding and unbinding kinetics are included with k_{on} denoting the binding rate and k_{off} characterizing the unbinding rate. A standard Hill function is ap-

plied to model the activation of downstream signal S by the complex MR. The maximal signal production rate and concentration at which the production is half of the maximum are denoted by v_s and k_{MR}, respectively. It is assumed that S regulates the synthesis of the receptor as a feedback regulation, which is also modeled as a Hill function, to accommodate the feedback regulation present in the *Drosophila* wing disc. The minimum and maximum receptor production rates are $v_{R,min}$ and $v_{R,max}$. The concentration producing half occupation is represented by k_s. Notice that only M can diffuse within the tissue, and all other components are restricted within the cell without diffusion.

$$\frac{\partial [M]}{\partial t} = D_M \nabla^2 [M] + s_M(x) - d_M [M] - k_{on} [M] [R] + k_{off} [MR] \tag{4.4}$$

$$\frac{\partial [R]}{\partial t} = v_{R,\min} + \frac{v_{R,\max} - v_{R,\min}}{1 + \left(\frac{[S]}{k_S}\right)^{n_1}} - d_R [R] - k_{on} [M] [R] + k_{off} [MR] \tag{4.5}$$

$$\frac{\partial [MR]}{\partial t} = k_{on} [M] [R] - k_{off} [MR] - d_{MR} [MR] \tag{4.6}$$

$$\frac{\partial [S]}{\partial t} = \frac{v_S}{1 + \left(\frac{[MR]}{k_{MR}}\right)^{n_2}} - d_S [S] \tag{4.7}$$

4.4.3 Dynamic mesh generator to couple mechanical and chemical submodels

To generate a computational mesh for the chemical signaling submodel, we first identify neighbors of individual cells based on the distance between membrane nodes of every two cells (See Figure 4.6 and Table 5.1 for more information). In particular, one cell is considered to be a neighbor of the other if the shortest distance between their membrane nodes is less than some threshold. This threshold is chosen based on the distance between

neighboring cells obtained in the equilibrium in the simulation (See Table 5.1 for more details). The same threshold is also used to determine a common edge between neighboring cells, i.e., membrane nodes from neighboring cells with a distance less than the threshold are selected to form a common edge. The middle points are calculated for each pair of those selected nodes, which give rise to a common edge between these two neighboring cells (Figure 4.6B). The endpoints of each shared edge are used to determine the vertices of the triangular mesh. It is possible that multiple cells neighboring each other give rise to a junction. Therefore we consider all common edges associated with the same junction point and calculate the centroid of their endpoints near the junction as a vertex in the triangular mesh (red dots in Figure 4.6C). We go over all junctions and calculate corresponding vertices throughout the tissue. Next, the center of each cell is obtained by calculating the centroid of all its membrane nodes, and it is connected to vertices obtained at junctions (Figure 4.6D). By doing that, each cell is discretized by a triangular mesh that shares a common edge with its neighboring cells, and triangles in all cells give rise to a mesh covering the entire tissue (Figure 4.2A). Notice that boundary cells usually lack neighbors along one or more sides; therefore their discretization will be treated separately (See the next section for more information). Nodes from cell membranes that act as the tissue boundary in those cells are selected as vertices such that some minimal distance is satisfied between successive ones. They are denoted by boundary vertices and connected with the corresponding cell centers to give rise to the triangular mesh inside boundary cells. A mesh quality check is implemented to guarantee that no highly skewed triangles are generated for convergence and accuracy of the computation over the mesh. Adjustment is conducted by merging or

splitting triangles if triangles are found to be too skewed in the quality check (See the next section for more information). Such a mesh generator provides triangular meshes in individual cells, as well as a global mesh over the whole tissue. Moreover, the triangular mesh is updated at some frequency to accommodate the cell deformation and tissue growth obtained in the mechanical submodel.

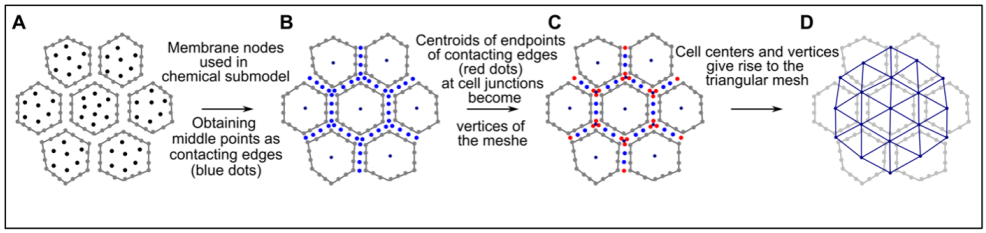

Figure 4.6: A) Nodes obtained from the mechanical submodel. Black nodes represent cytoplasm. Gray nodes represent cell membrane, connected by linear springs. B) Identifying common edges shared by neighboring cells. Blue dots are obtained as middle points of membrane nodes from neighboring cells. C) Identifying junction points, i.e., centroids of endpoints of contacting edges among neighboring cells, denoted by red nodes. D) Triangles obtained by connecting cell centers and junction points.

4.4.4 Treatments on skewed triangles and boundary cells

Highly skewed triangles involved in the triangular mesh may affect the convergence and precision of the numerical solver. As shown in gray color in Figure 4.7A, a highly skewed triangle is often generated when the shared edge of two neighboring cells is too short. To avoid that, we merge two vertices into one at the middle point when the edge of two neighboring cells is less than a threshold ($l_{intersect}$) (shown in red in Figure 4.7A'). Merging two vertices into one implies that each skewed triangle is now merged with the corresponding adjacent regular triangle (shown in green color in Figure 4.7A'). Consequently,

three connected triangles with the one skewed at the middle are now converted into two regular triangles (shown in blue color in Figure 4.7A").

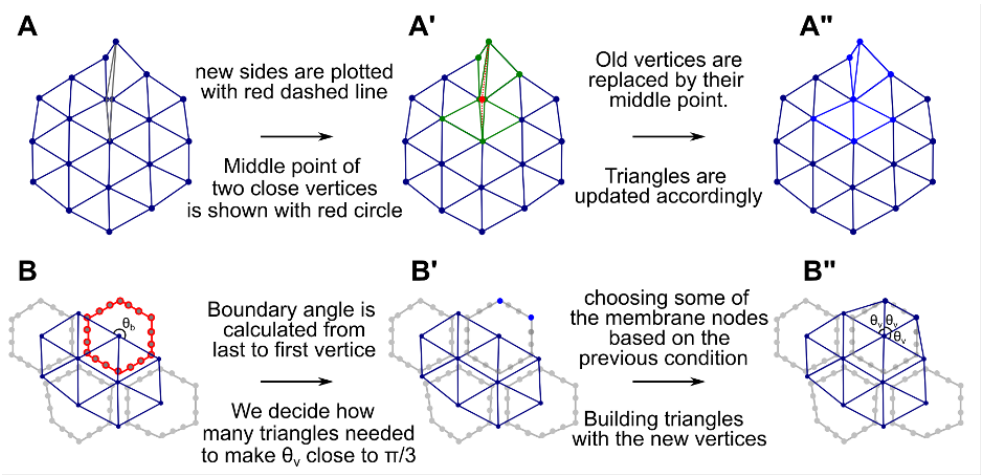

Figure 4.7: A) Triangular meshes with two highly skewed triangles. A') Midpoint of two close vertices is calculated, and A") old vertices are replaced by the midpoint, then we update triangles accordingly. B) A configuration within which the boundary cell is not covered by the triangular mesh. B') Some of the membrane nodes are chosen as vertices. The number of new vertices depends on the boundary angle. B") New triangles are built with the new vertices. Membrane nodes in (B') are chosen such that these triangles are close to equilateral triangles.

Discretizing boundary cells needs special treatment since some parts of their membrane are not adjacent to any other cells. The membrane parts of boundary cells that are not adjacent to any other cells (see the cell in red color in Figure 4.7B as an example) are discretized by selecting a few of their own membrane nodes (blue dots in Figure 4.7B') as the vertices of triangles. The number of membrane nodes is chosen so that triangles are close to equilateral triangles, as shown in Figure 4.7B". Mathematically, the number of new vertices on the membrane of boundary cells can be approximated according to the following equation:

$$n_{vertex} = Round[\frac{\theta_{boundary}}{\pi/3}] \tag{4.8}$$

4.4.5 Discretization of governing equations of chemical submodel

We discretize Equations. 4.4–4.7 by using the explicit Euler method in time. The diffusion of $[Dpp]$ is approximated by passive transport between neighboring triangles. The chemical submodel is solved on the triangular mesh to obtain the quasi-steady state. The chemical signaling concentration at the cell level is obtained by calculating the average over triangles within individual cells and is also used as the initial condition for the next update on the chemical signaling distribution.

$$\begin{aligned}[Dpp]_i^{t+\Delta t} = [Dpp]_i^t + (\ & D_{Dpp} \sum_{nghbr} \frac{A_{i,nghbr}\,([Dpp]_{nghbr}^t - [Dpp]_i^t)}{l_{i,nghbr}} \\ & + \frac{v_{Dpp}}{1+\left(\frac{x_i}{r_s L(t)}\right)^{n_s}} - \frac{d_{Dpp}}{1+\left(\frac{x_i}{r_s L(t)}\right)^{n_s}} [Dpp]_i^t \\ & - k_{on}[Dpp]_i^t[Tkv]_i^t + k_{off}[Dpp\_Tkv]_i^t\ ) \times \Delta t\end{aligned} \tag{4.9}$$

$$\begin{aligned}[Tkv]_i^{t+\Delta t} = [Tkv]_i^t + (\ & v_{\min} + \frac{v_{\max} - v_{\min}}{1+\left(\frac{[pMad]_i^t}{k_P}\right)^{n_1}} \\ & - d_{Tkv}[Tkv]_i^t - k_{on}[Dpp]_i^t[Tkv]_i^t + k_{off}[Dpp\_Tkv]_i^t\ ) \times \Delta t\end{aligned} \tag{4.10}$$

$$\begin{aligned}[Dpp\_Tkv]_i^{t+\Delta t} = [Dpp\_Tkv]_i^t + (\ & - d_{Dpp\_Tkv}[Dpp\_Tkv]_i^t \\ & + k_{on}[Dpp]_i^t[Tkv]_i^t - k_{off}[Dpp\_Tkv]_i^t\ ) \times \Delta t\end{aligned} \tag{4.11}$$

$$[pMad]_i^{t+\Delta t} = [pMad]_i^t + \left(\frac{v_P}{1+\left(\frac{[Dpp\_Tkv]_i^t}{k_{Dpp\_Tkv}}\right)^{n_2}} - d_P[pMad]_i^t \right) \times \Delta t \tag{4.12}$$

In Equations. 4.9–4.12, $[*]_{\mathrm{i}}^{\mathrm{t}}$ is the concentration of chemical signals on triangle i at time t. The diffusion is approximated as the flux between two neighboring triangles, which is dependent on the length of the contact edge, $\mathrm{A_{i,nghbr}}$, and the concentration gradient

between them. The steady state is obtained when the relative difference in concentrations of each chemical signal (Dpp, Tkv, and pMad) between two successive time steps is less than 10^{-4}, i.e.,

$$\frac{[\alpha]_i^{t+1} - [\alpha]_i^t}{[\alpha]_i^t \, \Delta t} < 10^{-4} \, \forall i \in all \, meshes, \, \alpha = \, Dpp, \, Tkv, \, Dpp_{Tkv}, \, pMad \tag{4.13}$$

Absorbing boundary condition is applied by assuming that free Dpp molecules would be diminished to zero at the boundary of the domain, corresponding to the fact that no Dpp signal was captured in the hinged region surrounding the wing disc pouch. We impose this condition in our chemical submodel by enforcing zero Dpp level on triangles along the tissue boundary at every time step, i.e.,

$$[Dpp]_i^t = 0 \forall t \, \& \, \forall i \in boundary \, meshes \tag{4.14}$$

4.4.6 Frequency of information exchange between mechanical and chemical submodels

When coupling the mechanical and chemical submodels, cell configurations used in the chemical submodel and chemical signal concentration used in the mechanical submodel need to be updated at some frequency to ensure consistent information is used in both submodels. Such frequency has to be chosen appropriately because too small frequencies will lead to non-compatible information exchanged between two submodels, while too big frequencies result in redundant computation and high computational cost.

When applying the coupled model to study the development of the *Drosophila* wing disc, the minimum time scale that takes one cell to enter the mitotic phase and divide is used to estimate the frequency of information exchange between two submodels. Considering the maximum cell growth rate at the beginning of the simulation ($g_{0,max} = 1.1 \times 10^{-4}$), it takes at least 9090 units of time in the mechanical submodel for one cell to start a cell cycle and divide. Note that the growth rate of daughter cells decays with respect to time. Therefore, cell cycle length increases in the later stage of the simulation. Thus 9090 units of time is the shortest cell cycle used in the simulation. Also, the chance of getting cell divisions will be higher if there are more cells involved. Therefore, we update the steady state of chemical signal concentration based on the cell configurations obtained most recently in the mechanical submodel every 200 units of time in the mechanical submodel, i.e., the coupling frequency $f_{exch} = 0.005$. This means we update the profile of chemical signals around 45 times within each cell cycle. This estimated frequency allows us to compute the relative change on the Dpp signal for all cells without too expensive computational cost.

We have utilized Intel(R) Xeon(R) CPU E5-1650 v2 3.50 GHz CPU and an Nvidia TITAN V graphic card (GPU) to run our simulations. The GPU is used to simulate the mechanical submodel, whereas the CPU is utilized to calculate the pseudo-steady state of the morphogen profile in the chemical signaling submodel. Typically, a simulation of the simplified model takes around 100 h to complete, while a simulation of the advanced model takes approximately 200 h. These simulation times are obtained from simulations with the highest rate of cell division in both simplified and advanced models. Other simulations in

each model take less time to complete as they have fewer cells included in the model during the simulation.

Chapter 5

Multi-scale Chemical-Mechanical Model: Convergence Analysis, Analytical Solutions, and Parameter Overview

5.1 Convergence tests on the chemical signaling submodel

To validate the convergence of the numerical method in approximating the quasi-steady state of the chemical submodel, we solve the reaction-diffusion equation governing the dynamics of the morphogen within a fixed domain at various mesh sizes. Since we assume the apical view of the wing disc tissue to be symmetric, we simplify the test by considering

only the right-hand side of the tissue domain. This approach doesn't compromise generality and allows us to focus on assessing convergence.

In this test, we primarily examine the convergence concerning mesh size using the simplified model (Equation 4.3). An absorbing boundary condition is applied at the right end. For time integration, we employ the Euler method. Therefore, the equation can be expressed as follows:

$$\partial M/\partial t = D\nabla^2 M + s(x) - dM \tag{5.1}$$

where M denotes the concentration of the morphogen molecules, D is the diffusion coefficient of morphogen molecules, d represents the degradation rate of morphogen molecules. The production rate of morphogen molecules by cells, denoted by $s(x)$, varies spatially. In particular, it is zero almost everywhere except at the origin (Figure 5.1A,B). To obtain the steady state of Equation 5.1 on a 1D domain, we divide it into N=10 and N=20 equal subintervals, creating two distinct meshes for the analysis.. We observe that the decay length of the morphogen gradient, $\lambda = \sqrt{\frac{D}{d}}$ (see section 5.2 for more detail), which measure the spread of the morphogen, is independent of the spatial mesh size (Figure 5.1A', B'), indicating the convergence of the morphogen gradient when reducing spatial mesh size.

We also compare the relative change of Dpp on meshes with different sizes in a 2D domain. Since the cell division rule employed in the coupled model depends on the relative change, it it necessary to show that the relative change is independent of mesh size, and consequently the cell division is independent of the mesh size. Specifically, we select a tissue arrangement consisting of 200 cells, derived from the simulation of the coupled model. Subsequently, we employ a mesh generator to create a triangular mesh structure

from this tissue configuration. Utilizing Equation 5.1, we determine the quasi-steady state of the morphogen gradient. This process is then replicated for the tissue containing 210 cells, generated through the same simulation of the coupled model. The relative change in the Dpp level between the two stages is calculated. Subsequently, we proceed to subdivide each triangle in the meshes for 200 and 210 cells into smaller triangles by dividing the edges along the cell boundary into 2 or 4 equal segments. Following the same computation as before, we determine the relative changes in Dpp on these refined meshes. The results are shown in Figure 5.1C. The relative changes observed across various meshes exhibited highly similar distributions. Specifically, when comparing the mesh without splitting to the one with mesh size halved, the R-squared value is 0.9, indicating a strong correlation between the two data sets of relative changes. The slope is 0.89, and the intercept is 0.005 for this comparison. Furthermore, when comparing the two refined meshes, the R-squared value increase to 0.98, indicating an even stronger correlation between the data sets. The slope is 1.2, and the intercept is 0.009 for this comparison. Indeed, both comparisons reveal that the relative changes of Dpp obtained over different meshes are remarkably similar to each other. This consistency strongly suggests that the approach we employed to calculate such relative changes is highly robust to variations in mesh size. We are also verifying the convergence of the morphogen gradient concerning the time step size in the 2D domain. For this purpose, we select a tissue configuration from simulation with $d = 0.04$ containing 182 cells. We calculate the quasi-steady-state level of Dpp using the time step $\Delta t = 5 \times 10^{-4}$. We reduce the time step by a factor of 2 and 4 and confirm that very similar morphogen gradients

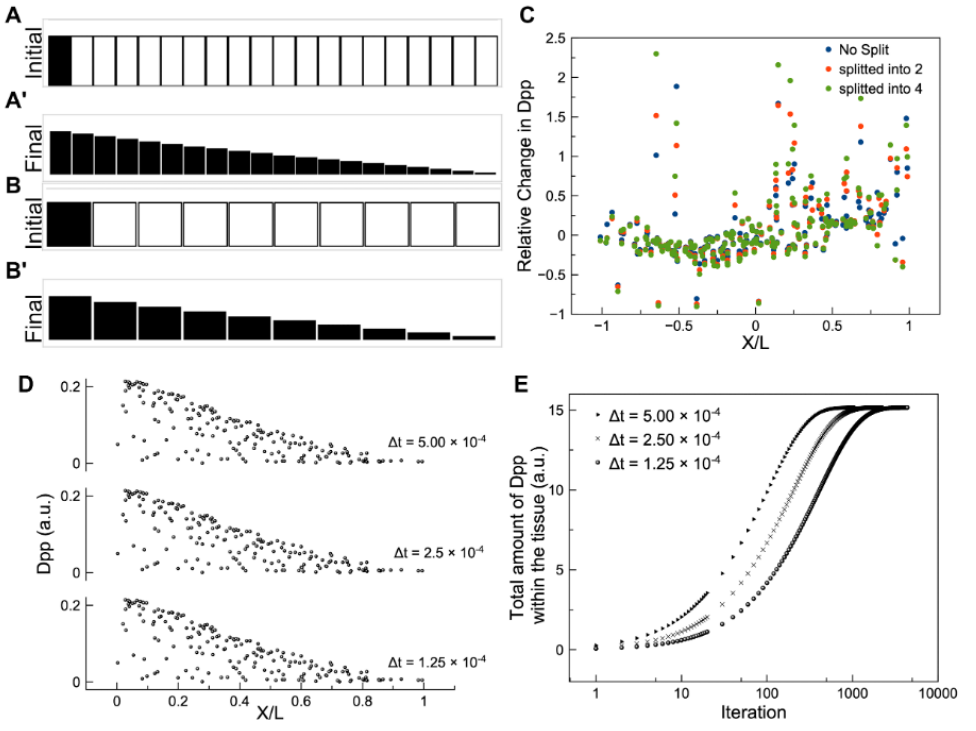

Figure 5.1: Initial distribution of morphogen in 1D domain using A) 20 and B) 10 mesh grids. A') and B') show the final distributions for (A) and (B) accordingly. Refer to Table 5.2 for parameters ($d = 0.04$). C) Relative change in Dpp profile for different mesh sizes. D) Cell level Dpp profile calculated based on the simplified model using different time steps and E) Tissue level Dpp calculated as a function of the number of iterations for different time steps.

are achieved (Figure 5.1D). However, more iterations is required to reach the quasi-steady state (Figure 5.1E), indicating the convergence when reducing the time step size.

5.2 Analytical solution to the 1D diffusion equation

The simplified chemical submodel, which considers only one chemical signal, can be solved analytically on the 1D domain. These analytical solutions provide valuable insights into how different parameters influence the steady-state distribution. By analyzing these solutions, we can better understand the behavior of the system under various conditions and gain important knowledge about the underlying mechanisms. The reaction-diffusion equation with a specific source function can be written as below:

$$\partial M/\partial t = D\nabla^2 M - dM + s(x) \tag{5.2}$$

$$s(x) = \begin{cases} v & x < L_s \\ 0 & x > L_s \end{cases} \tag{5.3}$$

where M represents the concentration of the morphogen, while D and d correspond to the diffusion rate and degradation rate, respectively. Production function, denoted by $s(x)$, is nonzero only near the origin. L_s is the length of the source region For steady state solution satisfying $\partial M/\partial t = 0$, we can assume it in the form of

$$M(x) = c_1 e^{-x/\lambda} + c_2 e^{x/\lambda} \tag{5.4}$$

where $\lambda = \sqrt{D/d}$. Boundary conditions are applied to determine values for c_1 and c_2. Assuming M is zero at infinity, the following boundary condition can be used to determine c_2.

$$M(\infty) = 0 \; ; c_2 = 0 \tag{5.5}$$

On the other hand, the total amount of M within the domain should be equal to the net change due to the production and degradation based on the mass conservation, i.e.,

$$\int_0^\infty M(x)dx = c_1\sqrt{D/d} = L_s v/d \tag{5.6}$$

Therefore, c_1 can be determined, and the analytical solution is written as below:

$$M(x) = \frac{L_s v}{\sqrt{Dd}} e^{-\sqrt{d/D}\ x} \tag{5.7}$$

From this equation, we observe that the spread of M depends on diffusion rate and degradation rate, i.e. $\sqrt{D/d}$, which is defined as the decay length. In particular, the concentration of M spreads further if the decay length is larger. When considering a finite domain with length L, the following boundary condition is used and c_2 can be determined.

$$M(x = L) = 0 \; ; c_2 = -c_1 e^{(-2L)/\lambda} \tag{5.8}$$

Similar to the previous calculation, we can determine c_1 by integrating both sides of the reaction-diffusion equation,

$$\int_0^L (D\nabla^2 M - dM + s(x)\ )\ dx = 0 \tag{5.9}$$

Therefore c_1 and the steady state solution are:

$$c_1 = \frac{L_s v}{d\lambda(e^{-L/\lambda} - 1)^2} \tag{5.10}$$

$$M(x) = \frac{L_s v}{d\lambda(e^{\frac{-L}{\lambda}} - 1)^2}(e^{\frac{-x}{\lambda}} - \frac{e^{\frac{x}{\lambda}}}{e^{\frac{2L}{\lambda}}}) \tag{5.11}$$

Based on this result, we observe that the steady state profile is closer to an exponential function when $\lambda \ll L$, while it decays linearly when $\lambda \gg L$.

5.3 Comparison of Dpp Relative Change under Different Boundary Conditions

No flux boundary condition gives rise to a flatter Dpp gradient when the degradation rate is very small. However, the level of Dpp gradient becomes high everywhere. As shown in Figure 4.5A, in the coupled model, the cell division condition will be checked multiple times in a cell cycle. Cells will only divide if the relative increase of Dpp exceeds 50%. Therefore, even though a high level of Dpp is achieved, it does not necessarily guarantee multiple instances of cell division. For a more detailed comparison of cell divisions

under the two boundary conditions, we compute the relative change of Dpp in individual cells for simulated tissues with 200-220 cells under different conditions. Then we plot the relative change of Dpp against their relative cell positions along the x-axis, as shown in Figure 5.2. In contrast to the absorbing boundary condition, under no flux boundary condition the relative increase of Dpp level is lower than 50% in most cells, with the exception of some cells near the middle of the tissue. This is because the absolute Dpp level is high everywhere and the relative increase becomes small, preventing cell division under no flux boundary condition. Therefore, Dpp distribution with a larger decay length helps a tissue grow longer, faster, and in a more spatially homogeneous manner, is only true for absorbing boundary conditions where the Dpp concentration is always decaying from the source to the sink.

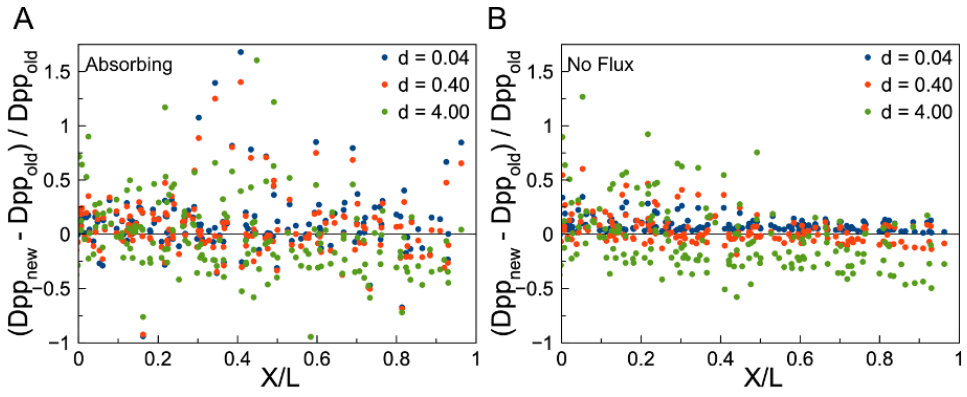

Figure 5.2: Relative change of Dpp value at cell level. The relative change in Dpp value calculated as the tissue grew from 200 to 220 cells under two boundary conditions: A) absorbing and B) no flux. The values are presented as a function of relative distance from the source region to individual cells. Tissue configurations are taken from the simulation resulting from a simplified model using absorbing boundary condition with $d = 0.04$. Different degradation rates are tested under different boundary conditions.

5.4 Table of parameters

5.4.1 Parameters used in mesh generation method

In the mechanical submodel, it is important to consider the distance between membrane nodes of neighboring cells, which averages around 0.3 μm. Therefore, the threshold value, denoted as l_{thres}, used to determine whether two cells are neighbors, should exceed 0.3 μm. Simultaneously, l_{thres} must be sufficiently small to distinguish membrane nodes from adjacent cells. To satisfy both conditions, we opt for l_{thres} to be 0.5 μm. The same threshold value is also utilized for merging closely located vertices into a single entity, as discussed in the section on Methods, and it is denoted as $l_{intersect}$. To avoid skewed triangles in the mesh, we ensure that there is at least a 1.0 μm distance between two neighboring vertices. In the simulated tissue, it is common to observe three cells that are neighbors to each other, and there are a few cases where four cells are also neighbors. To determine the vertices shared by three or four cells in the mesh structure, different threshold values are utilized. Specifically, for three-cell cases, we use $l_{thres} = 0.5$ μm, and for four-cell cases, a higher resolution is required, so we apply $l_{thres-4cell} = 0.35$ μm to identify neighboring cells more accurately. A list of parameters used for discretization is shown as below:

parameter	**Value**	**Unit**	**Description**
l_{thres}	0.5	μm	Based on the resolution of the model
$l_{intersect}$	0.5	μm	Based on the resolution of the model
$l_{thres-4cell}$	0.35	μm	Based on the resolution of the model

Table 5.1: Parameters used in discretization in the mechanical and chemical submodels

5.4.2 Parameters used in mechanical and chemical submodels and their coupling

Parameters related to the mechanical submodel, chemical submodel, and coupling are listed below:

parameter	**Value**	**Unit**	**Source or calibration section**
D_{Dpp}	20.0	$\mu m^2.s^{-1}$	[43]
v_{Dpp}	1.0	$M.s^{-1}$	[43]
d_{Dpp}	0.04 & 0.4 & 4.0	s^{-1}	Parameter study
r_s	0.12	_	[43]
Δt	5×10^{-4}	s	Based on stability of algorithm
f_{exch}	0.005	s^{-1}	Based on cell cycle lifetime

Table 5.2: Parameters in simplified chemical submodel in Eqn 8. We studied the effect of degradation of Dpp on tissue growth, proliferation distribution of cells within the tissue, and tissue circularity

parameter	**Value**	**Unit**	Source or calibration section
d_{Dpp}	0.1	$\mu m^2.s^{-1}$	Calibration in this study
k_{on}	0.025	$M^{-1}.s^{-1}$	[43]
k_{off}	0.000025	$M^{-1}.s^{-1}$	[43]
n_s	40.0	_	[43]
v_{min}	1.0	$M.s^{-1}$	[43]
v_{max}	10 & 20	$M.s^{-1}$	Parameter study
d_{Tkv}	0.1	s^{-1}	[43]
k_p	0.1 & 1.0 & 10	M	Parameter study
n_1	8.0	_	[43]
d_{Dpp_Tkv}	0.1	s^{-1}	[43]
v_{pMad}	1.0	$M.s^{-1}$	[43]
d_{pMad}	0.1	s^{-1}	[43]
k_{Dpp_Tkv}	1.0	M	[43]
n_2	-2.0	_	[43]

Table 5.3: Parameters in the advanced chemical submodel. Parameters not included are the same as the simplified model. k_p and v_{max} are perturbed to study the effect of feedback strength on tissue growth.

The mechanical submodel has been calibrated in Nematbakhsh *et al.*, (2017) [83]. We used the same mechanical parameters that can describe the mechanical properties of cells in Drosophila wing disc. The growth related parameters have been reduced in this study to reach better convergence, as shown in Table 5.4. The proliferation rate of the cell i^{th} is chosen stochastically between the minimum ($g_{0,min}$) and maximum ($g_{0,max}$) growth speed to resemble randomness in the cell growth rate. The maximum and minimum growth speed decay exponentially with respect to time to resemble growth speed reduction in the wing disc in time.

$$g_i(t) = Rnd(g_{0,min}, g_{0,max})\ e^{-k_g t} \tag{5.12}$$

$$g_i(t) = (g_{0,Avg} + Rnd(-g_0, g_0))\ e^{-k_g t} \tag{5.13}$$

parameter	**Value**	**Unit**	**Source or calibration section**
$g_{0,min}$	0.55×10^{-4}	$a.u^{-1}$	Model convergence
$g_{0,max}$	1.1×10^{-4}	$a.u^{-1}$	Model convergence
k_g	1.1×10^{-5}	$a.u^{-1}$	—

Table 5.4: Parameters in the mechanical submodel. * Arbitrary unit of time.

Chapter 6

Modeling Study of Bacterial Chemotactic Dynamics

6.1 Introduction

Flagellated motion in bacteria is a common mechanism that can lead to different swimming patterns depending on the number of flagella, and their location on the bacterial cell body. For example, different swimming patterns can occur due to differences in the bundling of flagella, such as the run-tumble pattern in *E. coli*, the run-reverse pattern in *Pseudomonas aeruginosa* and *Pseudomonas putida*, and the run-reverse-flick pattern in *Vibrio alginolyticus* [109, 110, 111, 112, 113, 114]. Bacterial chemotaxis refers to the way that the bacteria sense and react to chemical signals in their environment, and emerge a biased motion. This enables bacteria to understand signals and navigate towards or away from a source of nutrition or other resources to improve their survival chance. Chemotaxis

in *E. coli* controls frequency and duration of tumbling [115, 116, 117, 118, 119]. In some other bacteria, the motility pattern of the bacteria including running, and reversing, as well as the frequency of their reversals, is influenced by the gradient of the chemical signal [111]. The bacteria exhibit random swimming direction after each reversal event, however, they tend to reverse more often when swimming in the opposite direction of the chemoattractant gradient [111, 120].

A new swimming mode, called wrap mode, was discovered by simultaneously tracking individual bacteria and their flagellum [120, 121, 122]. In this mode, flagellar filament wraps around the bacteria cell body and unwraps momentarily when the flagellum switches its direction of rotation. Increasing the randomness in bacterial swimming direction, and decreasing the swimming speed are two important characteristics of the wrap mode [122]. The wrap mode is observed in the swimming pattern of *Pseudomonas aeruginosa* [122], *Pseudomonas putida* [120], and some other polar flagellated bacteria [123, 124, 125]. A computational study of chemotactic bacteria using Monod–Wyman–Changeux model shows that the wrap mode increases the bacterial chemotactic ability [115, 122]. A study on the motion of *P. putida* in the presence of a chemoattractant gradient revealed that the rate of transitions between swimming modes changes only when the bacteria is moving down the gradient in the wrap mode. Analytical study utilizing Keller-Segel approach suggests that when only one swimming mode is involved in the chemotactic strategy, the chemotaxis is optimized only if the bacteria swims faster in the chemotactic mode. However a mixed chemotactic strategy involving both run and wrap modes might be more effective if the bacterial reorientation during the wrap mode is insufficient [120].

Here we create and calibrate a multi-scale model of chemotactic bacteria and use this model to test various chemotaxis strategies and swimming patterns within fluid environments.

6.2 Results

6.2.1 Model simulations of bacteria in liquid

For simulations of bacterial chemotaxis in liquid, initially, N_b cells are distributed in a circular pattern of the radius R_0 with the center located in the center of the square domain of size $L_x \times L_y$. The orientation of the bacteria is randomly chosen between 0 (horizontal direction toward the right) and 2π. Bacteria might enter the wrap mode before reversing direction of motion depending on the choice of wrapping probability introduced in the model. Assuming the wrapping probability is zero, the bacteria would follow a run-reverse pattern.However, for nonzero wrapping probability the bacteria will follow a run-wrap-reverse swimming pattern. The background duration of runs in absence of chemoattractant gradient is calibrated using experimental data presented in Tian *et al.*[122] The run, and wrap durations are randomly drawn from an experimental distribution with a mean of 2.1 s and 1.0 s, respectively. However, durations might change depending on whether the bacteria is moving up or down the gradient. A point source of chemoattractant is located at the center of the domain. The distribution of the chemoattractant in the 2D domain is calculated using a finite difference method with no flux boundary condition. Using a chemotactic model explained in "Bacterial chemotactic submodel" , bacteria may reverse

sooner than expected if it is moving down the gradient. The simulations modeled bacterial movement for 200 seconds.

6.2.2 Determination of the levels of chemotaxis sensitivity for bacteria utilizing a run-reverse pattern to aggregation towards a source

Here we describe simulations of bacterial motion using a run-reverse pattern with different bacterial sensitivities to the chemoattractant gradient, ξ. We use three metrics to measure the chemotaxis efficiency and bacterial aggregation, including drift velocity, mean distance from the source, and aggregation time. The drift velocity of individual bacteria represents how far they move towards the source within a given time window. The average drift velocity is computed for the entire bacterial colony. The aggregation time is the accumulative time spent by each bacteria closer than an arbitrary threshold of 5 μm to the source. We show that the biased motion toward the up gradient increases with ξ . This can be seen through an increase in drift velocity toward the source, v_d, from relatively zero for low sensitivities ($\xi = 1$ and $\xi = 2$) to $v_d = 12\ \mu m/s$ and $v_d = 6.1\ \mu m/s$ for high sensitivities($\xi = 20$ and $\xi = 50$, respectively) (Figure 6.1A). In addition, the average distance from the source, $\bar{D}$, is more random for low sensitivity (dark blue in Figure 6.1B). However, $\bar{D}$ decreases faster when sensitivity is higher. For intermediate sensitivities ($\xi = 2$ and $\xi = 5$) the chemotaxis is weak far from the source, therefore the bacteria behave the same in both simulations at the beginning of the simulations (red and green in Figure 6.1B). Chemotaxis increases with the shortening of the distance from the source as the gradient becomes stronger. Higher sensitivity ($\xi = 5$) emerges a faster reduction in

$\bar{D}$. This transition happens when the average distance of the bacteria from the source is around 260 μm.

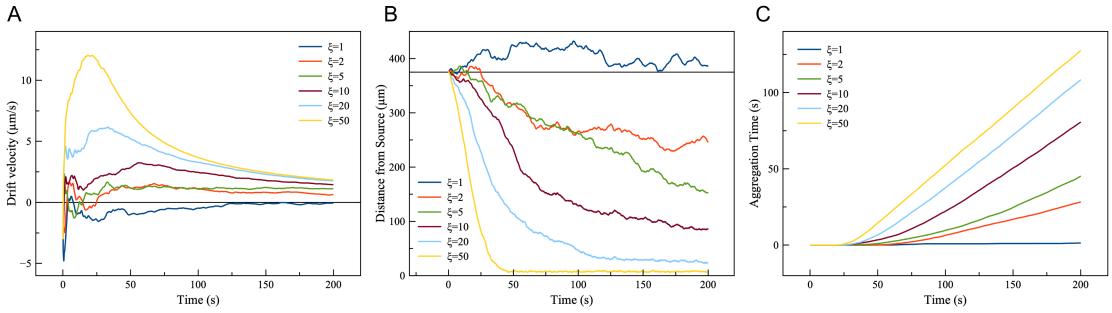

Figure 6.1: A) Drift velocity, B) distance from the source, and C) aggregation time as a function of time in simulations with run-reverse pattern

The aggregation time (t_{ag}), increases with ξ (Figure 6.1C). The aggregation time measured at the end of the simulation, t_{ag}, is 0, 0, 45.2, 115.5 and 127.7, for ξ equal to 1, 2, 5, 10, 20, and 50, respectively. for low sensitivities to chemotaxis ($\xi = 1$) the aggregation time is almost 0 (Dark blue in Figure 6.1C). This is because the chemotaxis sensitivity is small not only for making a biased motion toward up the chemoattractant gradient but also for keeping the bacteria that reached the source due to the random motion. For an intermediate level of chemotaxis sensitivity ($\xi = 10$), the aggregation time is $t_{ag} = 45.2\ s$ (burgundy in Figure 6.1C). The biased motion is strong enough to maintain bacteria near the source as the chemoattractant gradient is stronger close to the source. However, it takes a while for each individual bacteria to aggregate since further from the source the gradient is weak. By further increasing the sensitivity, the motion becomes more and more biased toward the source of the gradient even far from the source. This results in early aggregation of bacteria in the source region, therefore, increasing aggregation time. The

aggregation time for high sensitivities($\xi = 20$ and $\xi = 50$) is $t_{ag} = 115.5\ s$ and $t_{ag} = 127.7\ s$, respectively(light blue and yellow in Figure 6.1C). In these simulations we observe that the chemotaxis is not only important to improve navigation toward the source but also helps the bacteria to remain in a region with a high concentration of chemoattractant. We identified a range of parameter values for chemotaxis sensitivity in the baseline model that exhibits different degrees of chemotactic performance. This results can be used for future variations of the models and simulations.

6.3 Addition of wrap mode leads to a decreased ability to aggregate around a point source

In the previous section, we study the impact of chemotaxis sensitivity on bacterial motion that undergoes a run-reverse pattern. However recent studies revealed that the *P. aeruginosa* might enter into a new swimming mode, called wrap mode [120, 121, 122]. Motivated by these studies, we simulate the bacterial motion following a run-wrap-reverse pattern. The bacteria might enter to the wrap mode before reversing its direction of motion using a stochastic process (Refer to subsection 6.7.2 for more details.). First, we study the motion in the case that both wrap and run modes are involved in the chemotactic mechanism. In order to observe the impact of new motility pattern in the chemotaxis, we set the chemotactic sensitivity to be the same in both modes ($\xi_{wrap} = \xi_{run} \equiv \xi$). We find that the bacterial motion is still random for low chemotaxis sensitivities($\xi = 1, 2$ and 5). Furthermore, we observe an increase in biased motion as ξ increases, however, the biased motion toward the source is not as efficient as the run-reverse pattern. This can

be seen by the drop in the drift velocity and aggregation time for a fixed ξ. e.g Drift velocity and final aggregation time are $v_d = 9.1\ \mu m/s$ and $t_{ag} = 53.3\ s$, respectively in run-wrap-reverse pattern(yellow in Figure 6.2A and 6.2C), while they are $v_d = 12\ \mu m/s$ and $t_{ag} = 127.6\ s$ for the run-reverse pattern(yellow in Figure 6.1A and 6.1C) when $\xi = 50$. Here we conclude that having a more complicated swimming pattern results in lower efficiency in chemotaxis. Second, we study the bacterial motion in the case of no chemotactic behavior

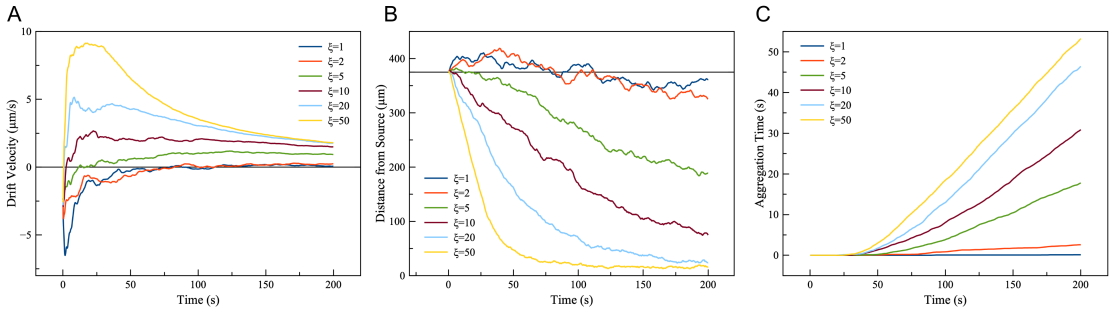

Figure 6.2: A) Drift velocity, B) distance from the source, and C) aggregation time as a function of time in the simulation with run-wrap-reverse pattern while both run and wrap mode involved in chemotaxis mechanism.

in the wrap mode ($\xi_{wrap} = 0.0$). Similar to the previous simulations, biased motion still increases with run. However it displays a further decrease in the drift velocity (Figure 6.3A) and aggregation time (Figure 6.3C) (e.g. $v_d = 5.6\ \mu m/s$ and $t_{ag} = 27.9\ s$ for $\xi_{run} = 50$) compared to the simulation with chemotactic wrap mode (Figure 6.2). These results suggest that introducing a new phase in which the bacteria is not chemotactic results in weaker biased motion. For further investigations, we add a stochastic process for bacteria to follow a run-reverse or a run-wrap-reverse pattern. The wrapping probability, P_{wrap}, determines which pattern emerges whenever the run duration is over. Increasing P_{wrap} represents a shift from a run-reverse to a run-wrap-reverse pattern. We observe that increasing the

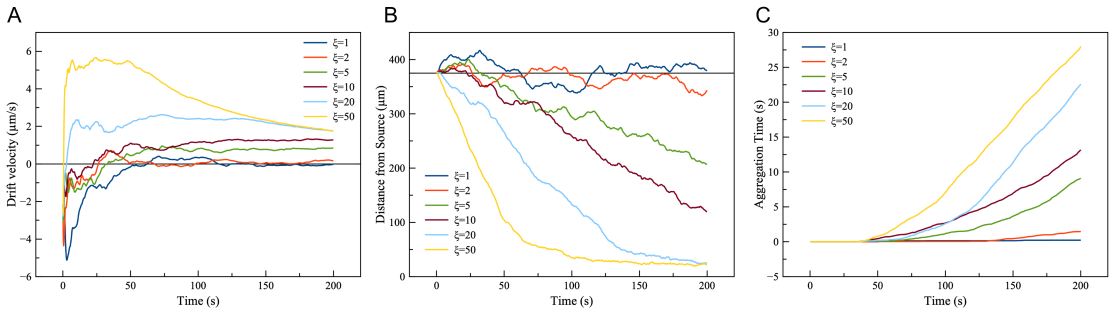

Figure 6.3: A) Drift velocity, B) distance from the source, and C) aggregation time as a function of time in the simulation with run-wrap-reverse pattern while the wrap mode is not involved in the chemotaxis mechanism.

P_{wrap} while the wrap mode is not involved in the chemotaxis mechanism leads to lower drift velocity and aggregation time. For a low probability of wrapping (dark blue in Figure 6.4),

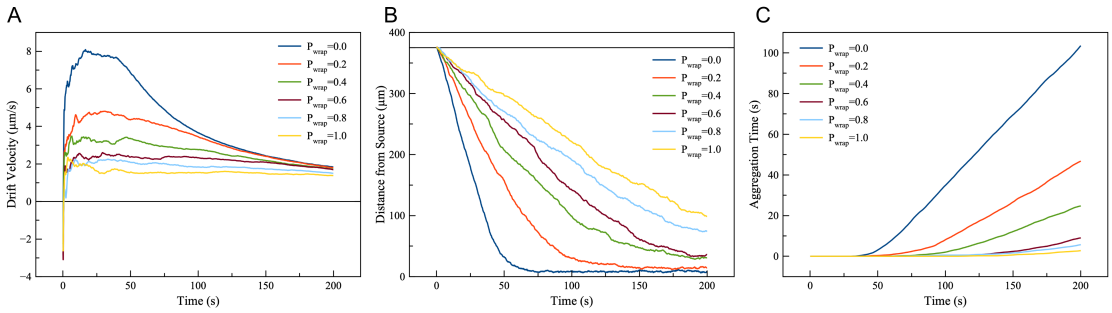

Figure 6.4: A) Drift velocity, B) distance from the source and C) aggregation time as a function of time for different wrapping probability, while the wrap mode is not involved in the chemotaxis mechanism.

the results look like the simulation with only the run-reverse pattern. On the other hand, high wrapping probabilities shows weaker biased motion as the duration of non-chemotactic phase increased, and the results are similar to non-chemotactic wrap mode in run-wrap-reverse pattern (Figure 6.3).

6.4 Chemotaxis within the dominant swimming mode is responsible for the aggregation ability of bacteria

In another chemotaxis mechanism, bacteria are not chemotactic during the run mode, meaning that the motion is unbiased regardless of the direction of motion concerning the chemoattractant gradient while the bacteria is in the run mode. Such behavior has been observed in the swimming of *P. putida* [120]. Thus we simulate the motion of bacteria following this pattern with relatively high sensitivity during the wrap mode ($\xi_{wrap} = 20$) and very low sensitivity during the run mode ($\xi_{run} = 0.01$). The bacteria will spend more time in the chemotactic phase as the wrapping probability increases, however, the motion is almost random even for very high wrapping probabilities ($P_{wrap} = 1.0$). The drift velocities calculated for all simulations are almost zero, except for $P_{wrap} = 1.0$ (yellow line in Figure 6.5A) with a drift velocity below 2 $\mu m/s$. For the high wrapping probability, we observe that the average distance from the source is reduced to 300 μm, then increases to 350 μm (yellow line in Figure 6.5B). Also by looking at the trajectory of individual bacteria, we noticed that those bacteria that successfully get closer to the source through chemotaxis, or even random motions, are unable to maintain their short distance to the source (yellow line in Figure 6.5B). The aggregation time is shorter than 0.3 s for all of the simulations(results are not included). These simulations suggest that this pattern cannot produce an aggregation near the source region, at least when the bacteria spend a long enough time in a non-chemotaxis phase.

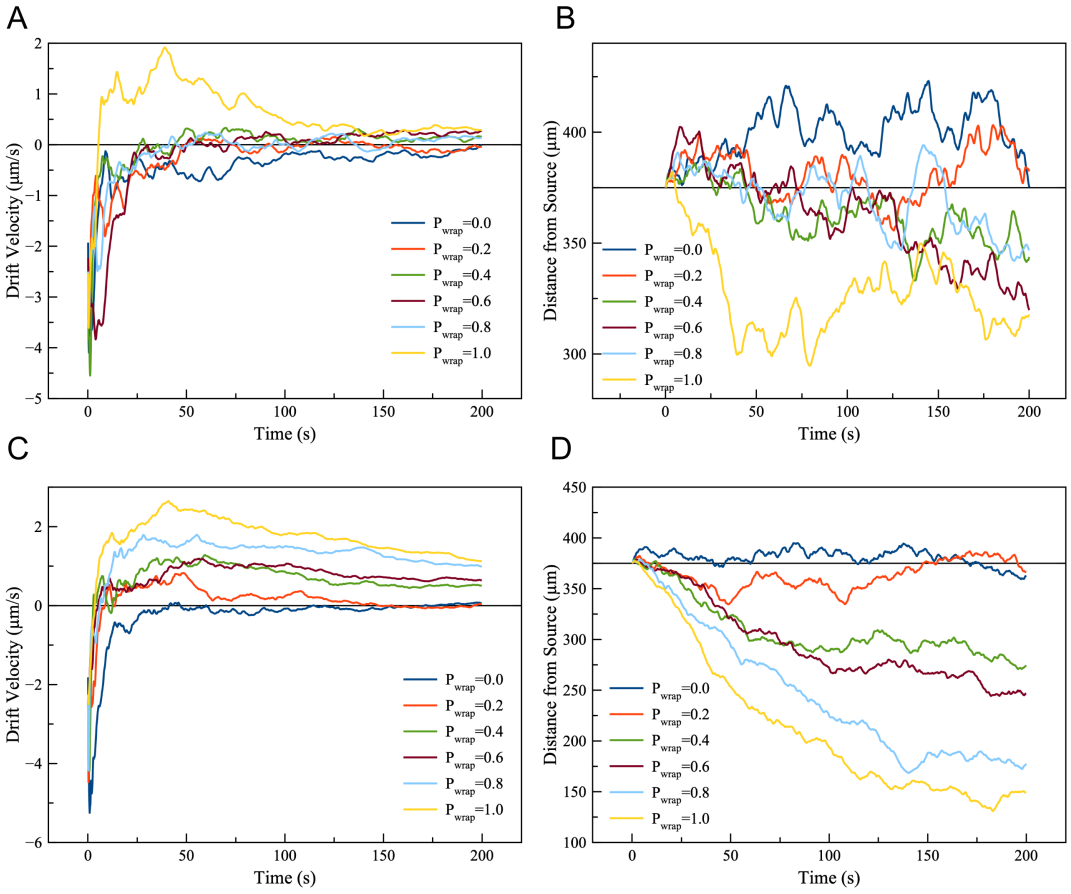

Figure 6.5: A,C) Drift velocity and B,D) distance from the source as a function of time for simulations with non-chemotactic run mode with run-wrap-reverse pattern. (A,B) Run and wrap durations are drawn from experimental distribution. (C,D) Distributions of run and wrap modes have been exchanged.

In another set of simulations, we exchange the time distributions of run and wrap modes so that the non-chemotactic mode become the shorter mode. Simulations with longer wrap mode and shorter run mode show an improvement in drift velocities and aggregation time. Most simulations reveal non-zero drift velocity (v_d is 2.6, 1.8, 1.2, and 1.2 μm for P_{wrap} equal to 1.0, 0.8, 0.6, and 0.4, respectively) and the aggregation time is below 1.5 s in the simulations (results are not included). The average distance from the source decreases as P_{wrap} increases. For low wrapping probabilities($P_{wrap} = 0.0$ or $P_{wrap} = 0.2$) the average distance from the source is about $\bar{D} = 375$ μm while for high wrapping probabilities ($P_{wrap} = 1.0$) is almost $\bar{D} = 150$ μm. These simulations suggest that reducing the duration of the non-chemotactic phase and enhancing the duration of the chemotactic phase improve the chemotaxis behavior. Yet, the mechanism is more efficient when the run mode is involved in the chemotaxis strategy rather than the wrap mode.

6.5 Emergence of wrap mode recover the strong chemotaxis in swimming pattern with small turning angles

In a simulation of chemotactic bacteria with small turning angles on average, $\theta_{turn,max}$, individual bacteria are able to reduce their distance to the source just by having a biased forward and backward motion. However at some stage in their path, they reach a point where their direction is perpendicular to the direction of the source. Then, they will move back and forth, and the length of their movement is determined by the local chemoattractant gradient. Therefore, the chemotaxis behavior is limited in this case and it highly

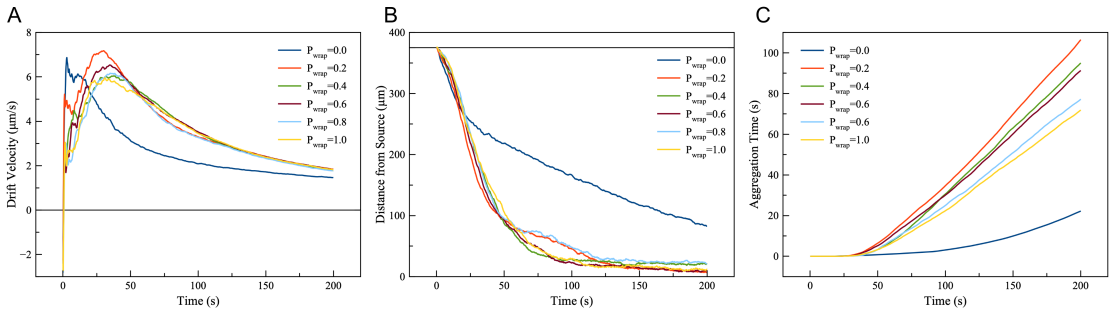

Figure 6.6: A) Drift velocity, B) distance from the source and C) aggregation time as a function of time for different wrapping probability for bacteria following run-reverse pattern without re-orientations)

depends on the initial orientation of bacteria. Here we have introduced a source of reorientation with wrapping mode with different probability of occurrence. We have observed that the emergence of non-chemotactic wrap mode, serving as a source for reorientation, recovers the effective chemotaxis and results in faster aggregation of the bacteria around the source region. We also observed that having a high probability of the wrapping mode is unnecessary, as a small reorientation is sufficient to recover strong chemotaxis.

6.6 Conclusion and Future Plans

In this study, we have developed a Sub-Cellular Element model and integrated it with a chemotaxis model to analyze diverse bacterial motility patterns under different chemotaxis strategies. We observed that chemotaxis is particularly effective for simple swimming patterns like the run-reverse motion. The efficiency of chemotaxis increases with the sensitivity of the bacteria to the chemoattractant. Complicated swimming patterns are not necessarily increasing chemotaxis. However, in specific cases, such as bacteria employing a run-reverse pattern without reorientation, chemotaxis becomes limited. In such

scenarios, incorporating a reorientation source using the wrap mode significantly enhances the efficiency of chemotaxis. These findings are more consistent with the outcomes derived from the Keler-Segel analytical approach, rather than the agent-based model with Monod-Wyman-Changeux for describing chemotaxis behavior [120, 122]. One possible explanation behind this difference lies in the variations between the models employed to reflect chemotaxis behavior. Another possible explanation concerns the dissimilarities in cell body re-orientation. In the study by Tian et al. (2022) [122], cells alter their orientation during both the pull and push modes, while in our model, re-orientations occur following the reversal events. It is plausible that the average cell body re-orientation differs across the models. Our simulations involving mixed chemotaxis strategies revealed that if bacteria spend extended periods in a non-chemotactic mode, they struggle to remain near the source region. Hence, chemotaxis and aggregation are most robust when the dominant swimming mode is part of the chemotaxis strategy.

The model we have developed enables the simulation of bacterial motion in the presence of a fungi network. Specifically, the model incorporates the bacteria's natural inclination to follow hyphae segments. The presence of a fungal network can affect the ability of bacteria to sense these chemical cues. Fungal hyphae may act as a physical barrier to the bacterial motion, preventing bacteria from moving and doing chemotaxis. Moreover, fungal hyphae may also secrete chemicals that attract or repel bacteria, further affecting bacterial chemotaxis around fungal networks. Our future plans involve simulating how bacteria interact with the hyphae structure through their responses to small metabolites, and investigating how bacteria migrate towards the tips of the fungi network by utilizing

highway following and chemotaxis in response to the large metabolites secreted at the tips of the network.

6.7 Methods

6.7.1 Model description

In this section we describe a subcellular element modeling approach [126] and use it to represent individual bacteria and their mechanical interactions with other bacteria and the environment. Then we account for the chemotactic response of the bacteria [127], and couple it with the mechanical submodel. Parameters involved in this model can be found in Table 6.1 and 6.2

6.7.2 Bacterial motility submodel

Mechanical Model of Bacteria. We use the Subcellular Element (SCE) model to describe bacterial physical properties and motion. In this model, each bacteria is represented by nodes connected to one another by linear and rotational springs (Figure 6.7). *Pseudomonas* is a relatively small bacteria with a length of approximately 2 μm on average, In order to reduce the computational cost while still accounting for the details in the physical properties of the bacteria, we assume that each bacteria consists of five nodes. Linear springs allow for a reasonable amount of straining in the bacteria length while generally maintaining its average length fixed. In an individual cell, the bonding force, F^i_{bond}, represents the force between two nodes connected by linear spring.

$$F^i_{bond} = \sum_{j \in BN(i)} k_b(|x_i - x_j| - l_{eq})\hat{r}_{ij} \tag{6.1}$$

where l_{eq}, the equilibrium distance between two consecutive nodes, is equal to the length of the bacteria divided by the number of springs required to connect the nodes, $N_{nodes} - 1$ (Figure 6.7). In this case we have $l_{eq} = 0.5\ \mu m$. The set of bonded neighbors of node is donated by $BN(i)$. k_b is the linear spring constant (Table 6.1), x_i is the position of node i, and $\hat{r}_{ij}$ is the directional unit vector pointing from node i to node j.

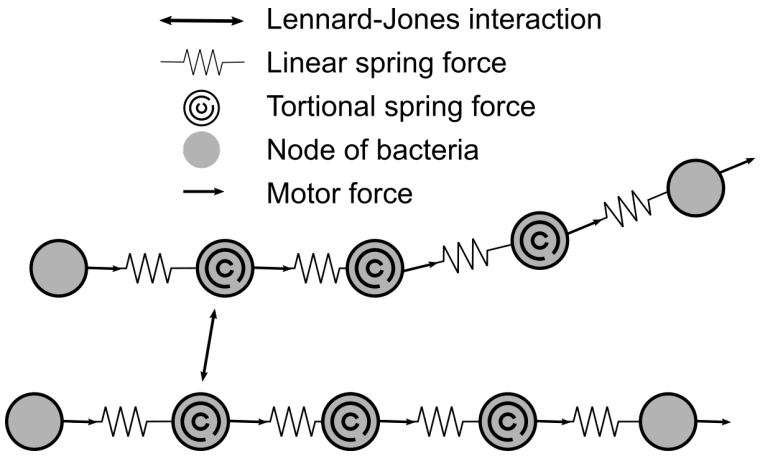

Figure 6.7: Interactions between different nodes in the Sub-Cellular Element model.

Bending stiffness of a bacteria is modeled by rotational springs. The bending energy of a joint, constituted by 3 consecutive nodes namely i, j and k, denoted by U_{bend}, reads as:

$$U_{bend} = k_{bend}[1 - cos(\theta_{ijk} - \theta_{eq})] \tag{6.2}$$

where k_{bend} is the corresponding spring constant (Table 6.1), θ_{ijk} is the angle between nodes i, j, and k, and $\theta_{eq} = \pi$ is the equilibrium angle. The bending forces of a joint (F^i_{bend}, F^k_{bend},

and F^j_{bend}) can be calculated by getting the derivative of bending energy (Equation 6.2). [128]

$$F^i_{bend} = -k_{bend}(\frac{\vec{r}_{kj}}{|r_{ij}||r_{kj}|} - cos\theta_{ijk}\frac{\vec{r}_{ij}}{|r_{ij}|^2}) \tag{6.3}$$

$$F^k_{bend} = -k_{bend}(\frac{\vec{r}_{ij}}{|r_{ij}||r_{kj}|} - cos\theta_{ijk}\frac{\vec{r}_{kj}}{|r_{kj}|^2}) \tag{6.4}$$

$$F^j_{bend} = -(F^i_{bend} + F^k_{bend}) \tag{6.5}$$

Swimming motility of the bacteria due to the flagellum activities is also modeled. Each bacteria moves forward with a constant propulsive force f_{motor}. In order to have a smooth motion in the simulated bacteria, the propulsive force is distributed uniformly among all the nodes of the bacteria (Figure 6.7). Therefore the propulsive force applied to each node follows:

$$F^i_{motor} = \frac{f_{motor}}{N_{nodes}}\hat{r}_{i,i+1} \tag{6.6}$$

Starting from the node at the tail to the head, each node is moving toward the next node. The head node also moves in the same direction as the node behind it. We also assume that the propulsive force is similar for all the bacteria moving in a medium.

The dynamics of each SCE is achieved by the cell-cell and cell-environment interactions. Since our model assumes an overdamped regime,the inertia forces are negligible. The motion of the bacteria is represented by the following equation,

$$\frac{dx_i(t)}{dt} = \frac{-1}{\gamma}\nabla_i U^i(x,t) \tag{6.7}$$

$$-\nabla_i U^i(x,t) = F^i(x,t) = F^i_{bond} + F^i_{bend} + F^i_{motor} \tag{6.8}$$

where γ is the friction coefficient and $-\nabla_i U^i(x,t)$ is the net force acting on node i. The term on the left hand side of the Equation 6.7 depicts the time derivative of the location of the bacteria in 2D space. The term on the right hand side of the Equation 6.7 is the equivalent force applied to the element due to the interactions written as a gradient of energy state of the system, $-\nabla_i U^i(x,t)$. We use Euler's forward method to solve the equations of motion. In vitro experiments, the vertical displacement of the bacteria is limited compared to their horizontal displacement, therefore we made our bacterial model in 2D. In order to maintain the number of bacteria in each simulation we used periodic boundary conditions for the motion of bacteria,assuming a bacteria reaches to the domain from one side when another one leaves from the other side.

Mechanical Modeling Of The Wrap Mode. A new mode of motion has been observed in the swimming of *Pseudomonas aeruginosa* and *Pseudomonas putida* in which their flagellum might wrap around the bacteria when the flagellum switches its direction of rotation. This results in a reduction to the speed of the bacteria while randomizing its direction of motion. In this way, the bacteria continues moving forward with an increase in its angular velocity until the flagellum unwraps causing the bacteria to undergo a standard reversal process. We have added this mode of motion to our model using a stochastic process which assigns a probability for the bacteria to enter wrap mode before each reversal. The duration and angular velocity of the wrap mode has been measured experimentally for *P.aeruginosa*. Thus, in our model, if the bacteria enters wrap mode, we randomly select a turn angle and mode duration from experimentally observed distributions. During the wrap

mode, a reduced motor force is applied to the nodes, and the orientation of the force at the head node is rotated by the turn angle. We assume that wrap mode delays the reversal process and after the chosen duration the bacteria reverses as described below.

6.7.3 Bacterial chemotactic submodel

The bacteria do run-reverse in order to navigate better toward nutrition sources. The frequency of reversing the direction of motion is controlled by an internal clock. Previous studies show that the reversal rate follows the equation below [127]:

$$\lambda = \lambda_0 e^{(-\xi v \cdot \nabla s \ \Theta(-v \cdot \nabla s))}; \ \Theta(u) = \begin{cases} 0 & u < 0 \\ 1 & u > 0 \end{cases} \tag{6.9}$$

where λ_0 is the rate of reversal in absence of chemoattractant, v is the velocity of the bacteria. The concentration of chemoattractant is represented by s, and ξ is a scalar that corresponds to the strength of the chemotaxis. Here we assume the bacteria is a pessimistic bacteria in terms of chemotactic behavior meaning that the frequency of reversal increases as the bacteria is moving down the gradient but remains unchanged while moving up the gradient. In our model, the reversal rate is controlled by a Heaviside function $\Theta(-v \cdot \nabla s)$. When a bacterium is moving up a gradient, $v \cdot \nabla s > 0$, and $\Theta = 0$, therefore the reversal frequency remains unchanged ($\lambda = \lambda_0$), and the bacteria continue moving up the gradient. On the other hand, when a bacterium is moving down the gradient, $v \cdot \nabla s < 0$, then $\Theta = 1$ and a relatively high frequency of reversal helps the bacteria to avoid an unfavorable

environment. The bacteria reverses its direction of motion earlier in order to search for a new environment that might be more suitable for them.

Bacteria Clock and Bacterial Reversals. Within our model, each bacteria has an internal clock that keeps track of the time spent in its current swimming mode (e.g run mode or wrap mode). The time on the clock increases with every simulation step until it reaches a maximal threshold defined as $T_{rev} = \frac{1}{\lambda_{run}}$ run for run mode and $T_{unwrap} = \frac{1}{\lambda_{wrap}}$ wrap for wrap mode. Then the bacteria starts its next swimming mode. During the reversal time, the bacteria rotates its orientation randomly and tries to explore a different path. We use a uniform distribution between $-\pi/3$ and $\pi/3$ for the turning angle of the bacteria. The motor force at the head node of the bacteria is perturbed by turning angle for a short interval, called turning time. Note that the turning angle is not a function of chemoattractant concentration and the only way that the bacteria use chemotaxis to navigate to the source is through controlling the reversal rate. The reversal time and unwrapping time might be manipulated only if the related swimming mode is involved in the chemotaxis mechanism.

Computational Implementation Of The Model. We use a finite difference method to model diffusion and secretion of chemoattractant in the environment. The domain is discretized to squares with length of 5 μm and the chemoattractant can diffuse from one square to 4 neighboring squares. Note that the size of the grid must be smaller than the average distance travelled by bacteria in during each run because we need to calculate the gradient of chemoattractant based on a temporal manner, and it depends on how long

the bacteria moves within that interval. The concentration of chemoattractant is used to modify the reversal rates of bacteria moving in the 2D domain.

$$v \cdot \nabla s = \frac{s(x(t+\Delta t), y(t+\Delta t)) - s(x(t), y(t))}{\Delta t} \tag{6.10}$$

The time scale of diffusion of chemoattractant is faster than the motion of the bacteria, therefore we calculate the profile before initializing the bacteria colony. We find the chemoattractant distribution by solving diffusion equation with a constant source located at the center of the domain using Euler forward method.

6.7.4 Table of Parameters

Parameters used for modeling individual bacteria, their swimming patters, modeling the secretion and diffusion of chemoattractant, and domain properties are listed here.

Parameter	Value	Unit	Description and source
$L_{bacteria}$	2	μm	Length of bacteria[129]
N_{nodes}	5	_	Number of nodes in a bacteria
k_b	5.0	$\mu N \cdot \mu m^{-1}$	Stiffness of linear spring
k_{bend}	0.5	$\mu N \cdot \mu m$	Stiffness of torsional spring
$f_{motor,run}$	1.5	μN	Motor force in run mode
$f_{motor,wrap}$	0.64	μN	Motor force in wrap mode
t_{run}	0.7	s	Run mode's mean duration [122]
t_{wrap}	-0.4	s	Wrap mode's mean duration[122]
$\sigma_{t,run}$	0.6	_	Run mode's duration SD[122]
$\sigma_{t,wrap}$	0.9	_	Wrap mode's duration SD[122]
$\bar{\omega}_{wrap}$	0.52	s^{-1}	Wrap mode's mean angular velocity[122]
$\sigma_{\omega,wrap}$	0.18	_	Wrap mode's angular velocity SD[122]
$\theta_{turn,max}$	$\pi/3$	_	Maximum turning angle
t_{turn}	0.2	s	Duration of turning
t_{min}	0.3	s	Minimum duration of modes
$L_x \times L_y$	1000×1000	μm^2	Size of the domain
N_b	50	_	Number of bacteria
T_{total}	200	s	Total time of simulation
γ	0.01	$\mu N \cdot s \cdot \mu m^{-1}$	Damping coefficient
dt	0.00001	s	time step
R_0	375	μm	Initial distance from the source
R_{agg}	5	μm	Threshold of source vicinity
ξ	Parameter study*	_	Bacterial chemotaxis sensitivity
P_{wrap}	Parameter study**	_	Wrapping probability

Table 6.1: Mechanical and motility parameters used in simulating bacterial swimming.
$*$ The sensitivity of the bacteria to the chemical gradient has been changed in different simulations. The numbers are 1, 2, 5, 10, 20, and 50.
$**$ The wrapping probability is zero for run-reverse pattern, and is chosen from 0.2, 0.4, 0.6, 0.8, and 1.0 for run-wrap-reverse pattern.

parameter	Value	Unit	Description and source
D	200	$\frac{\mu m^2}{a.u\ of\ time}$	Diffusion coefficient
p	100	$a.u$	Chemoattractant secretion rate
dt_{chem}	0.05	$a.u\ of\ time$	chemical model's time step
$\Delta x \times \Delta y$	5×5	μm^2	Grid size
t_{chem}	500	$a.u\ of\ time$	Total duration of chemical model

Table 6.2: parameters used in simulating chemoattractant distribution

Chapter 7

Summary

In this conclusion, the three projects have successfully uncovered complex dynamics that occur across different biological scales.The first project focused on viral capsid assembly and disassembly, highlighting the interesting hysteresis demonstrated by the empty capsids. The classical nucleation theory was utilized to explain these transitions by analyzing changes in free protein concentration during the process, indicating the existence of barriers for both assembly and disassembly.

The second project investigates morphogen spreading and tissue growth, with a focus on understanding the regulatory mechanisms that govern tissue development in the Drosophila wing disc tissue. By integrating chemical signals and mechanical forces through a multiscale model, we have gained a deeper understanding of the complex interplay that drives tissue size, shape, and growth regulation. Our research has revealed that the size of the domain of the Dpp morphogen gradient is a crucial factor in determining tissue size and shape, with larger gradients leading to faster growth rates and more symmetric

shapes. Additionally, we have discovered that the downregulation feedback is a key mechanism that allows for morphogen spreading, thereby prolonging tissue growth at a spatially homogeneous rate.

In the third project, we focused on modeling chemotactic bacteria. Our study involved analyzing various bacterial swimming patterns and chemotaxis strategies to gain insights into how bacterial chemotaxis can be optimized and the impact of complex behaviors on aggregation. Throughout our research, we explored a wide range of bacterial motility patterns and found that chemotaxis is most efficient in simple swimming patterns, such as the run-reverse motion. While complex swimming patterns may lead to aggregation, this only occurs when the dominant swimming mode is chemotactic. Finally, we discovered that complex swimming patterns can recover the chemotaxis efficiency for cases with limited re-orientation.

In summary, these projects have uncovered the basic principles that govern biological systems across various scales. They have provided valuable insights into the complexities of viral dynamics, tissue growth regulation, and bacterial movement. The intersection of these research pathways enriching our understanding of the multifaceted dynamics in the world of biology.

Bibliography

[1] Robijn F. Bruinsma, Gijs J. L. Wuite, and Wouter H. Roos. Physics of viral dynamics. *Nature reviews. Physics*, pages 1–16, January 2021. ISSN 2522-5820. doi: 10.1038/s42254-020-00267-1.

[2] Thomas C. T. Michaels, Mathias M. J. Bellaiche, Michael F. Hagan, and Tuomas P. J. Knowles. Kinetic constraints on self-assembly into closed supramolecular structures. *Scientific reports*, 7(1):12295, September 2017. ISSN 2045-2322. doi: 10.1038/s41598-017-12528-8.

[3] Roya Zandi, Bogdan Dragnea, Alex Travesset, and Rudolf Podgornik. On virus growth and form. *Physics Reports*, 847(C), March 2020. doi: 10.1016/j.physrep.2019.12.005.

[4] Roya Zandi, Paul van der Schoot, David Reguera, Willem Kegel, and Howard Reiss. Classical Nucleation Theory of Virus Capsids. *Biophysical Journal*, 90(6):1939–1948, 2006. ISSN 0006-3495. doi: https://doi.org/10.1529/biophysj.105.072975. URL `https://www.sciencedirect.com/science/article/pii/S0006349506723803`.

[5] Suzanne B. P. E. Timmermans, Alireza Ramezani, Toni Montalvo, Mark Nguyen, Paul van der Schoot, Jan C. M. van Hest, and Roya Zandi. The Dynamics of Viruslike Capsid Assembly and Disassembly. *Journal of the American Chemical Society*, 144 (28):12608–12612, July 2022. ISSN 1520-5126 0002-7863. doi: 10.1021/jacs.2c04074.

[6] Zachary D. Harms, Lisa Selzer, Adam Zlotnick, and Stephen C. Jacobson. Monitoring Assembly of Virus Capsids with Nanofluidic Devices. *ACS nano*, 9(9):9087–9096, September 2015. ISSN 1936-086X 1936-0851. doi: 10.1021/acsnano.5b03231.

[7] Pepijn Moerman, Paul van der Schoot, and Willem Kegel. Kinetics versus Thermodynamics in Virus Capsid Polymorphism. *The journal of physical chemistry. B*, 120 (26):6003–6009, July 2016. ISSN 1520-5207. doi: 10.1021/acs.jpcb.6b01953. Place: United States.

[8] Adam Zlotnick. To Build a Virus Capsid: An Equilibrium Model of the Self Assembly of Polyhedral Protein Complexes. *Journal of Molecular Biology*, 241(1): 59–67, August 1994. ISSN 0022-2836. doi: 10.1006/jmbi.1994.1473. URL https://www.sciencedirect.com/science/article/pii/S0022283684714732.

[9] T. Keef, C. Micheletti, and R. Twarock. Master equation approach to the assembly of viral capsids. *Journal of theoretical biology*, 242(3):713–721, October 2006. ISSN 0022-5193. doi: 10.1016/j.jtbi.2006.04.023. Place: England.

[10] D. C. Rapaport. Role of reversibility in viral capsid growth: a paradigm for self-assembly. *Physical review letters*, 101(18):186101, October 2008. ISSN 0031-9007. doi: 10.1103/PhysRevLett.101.186101. Place: United States.

[11] C. Berthet-Colominas, M. Cuillel, M. H. J. Koch, P. Vachette, and B. Jacrot. Kinetic study of the self-assembly of brome mosaic virus capsid. *European Biophysics Journal*, 15(3):159–168, December 1987. ISSN 1432-1017. doi: 10.1007/BF00263680. URL https://doi.org/10.1007/BF00263680.

[12] Roi Asor, Christopher John Schlicksup, Zhongchao Zhao, Adam Zlotnick, and Uri Raviv. Rapidly Forming Early Intermediate Structures Dictate the Pathway of Capsid Assembly. *Journal of the American Chemical Society*, 142(17):7868–7882, April 2020. ISSN 0002-7863. doi: 10.1021/jacs.0c01092. URL https://doi.org/10.1021/jacs.0c01092. Publisher: American Chemical Society.

[13] Roya Zandi and Paul van der Schoot. Size regulation of ss-RNA viruses. *Biophysical journal*, 96(1):9–20, January 2009. ISSN 1542-0086 0006-3495. doi: 10.1529/biophysj.108.137489.

[14] Antoni Luque, David Reguera, Alexander Morozov, Joseph Rudnick, and Robijn Bruinsma. Physics of shell assembly: line tension, hole implosion, and closure catastrophe. *The Journal of chemical physics*, 136(18):184507, May 2012. ISSN 1089-7690 0021-9606. doi: 10.1063/1.4712304. Place: United States.

[15] Dimo Kashchiev. nucleation: basic theory with applications. In *Nucleation*, pages 113–290. Elsevier, 2000. ISBN 0-08-053783-9.

[16] Antoni Luque Santolaria. *Structure, mechanical properties, and self-assembly of viral capsids*. Universitat de Barcelona, 2011. ISBN 84-694-6593-7.

[17] Michael F. Hagan. Modeling Viral Capsid Assembly. *Advances in chemical physics*, 155:1–68, 2014. ISSN 0065-2385 1934-4791. doi: 10.1002/9781118755815.ch01.

[18] J. B. Bancroft and E. Hiebert. Formation of an infectious nucleoprotein from protein and nucleic acid isolated from a small spherical virus. *Virology*, 32(2):354–356, June 1967. ISSN 0042-6822. doi: 10.1016/0042-6822(67)90284-x. Place: United States.

[19] J. B. Bancroft. The self-assembly of spherical plant viruses. *Advances in virus research*, 16:99–134, 1970. ISSN 0065-3527. doi: 10.1016/s0065-3527(08)60022-6. Place: United States.

[20] K. W. Adolph and P. J. Butler. Studies on the assembly of a spherical plant virus. I. States of aggregation of the isolated protein. *Journal of molecular biology*, 88(2):327–341, September 1974. ISSN 0022-2836. doi: 10.1016/0022-2836(74)90485-9. Place: England.

[21] Maelenn Chevreuil, Lauriane Lecoq, Shishan Wang, Laetitia Gargowitsch, Naïma Nhiri, Eric Jacquet, Thomas Zinn, Sonia Fieulaine, Stéphane Bressanelli, and Guillaume Tresset. Nonsymmetrical Dynamics of the HBV Capsid Assembly and Disassembly Evidenced by Their Transient Species. *The journal of physical chemistry. B*, 124(45):9987–9995, November 2020. ISSN 1520-5207. doi: 10.1021/acs.jpcb.0c05024. Place: United States.

[22] Jinsheng Zhou, Adam Zlotnick, and Stephen C. Jacobson. Disassembly of Single Virus Capsids Monitored in Real Time with Multicycle Resistive-Pulse Sensing. *Analytical Chemistry*, 94(2):985–992, January 2022. ISSN 0003-2700. doi: 10.1021/acs.analchem.1c03855. URL `https://doi.org/10.1021/acs.analchem.1c03855`. Publisher: American Chemical Society.

[23] Yohei Yamauchi and Urs F. Greber. Principles of Virus Uncoating: Cues and the Snooker Ball. *Traffic (Copenhagen, Denmark)*, 17(6):569–592, June 2016. ISSN 1600-0854 1398-9219. doi: 10.1111/tra.12387.

[24] Michael F. Hagan and David Chandler. Dynamic pathways for viral capsid assembly. *Biophysical journal*, 91(1):42–54, July 2006. ISSN 0006-3495 1542-0086. doi: 10.1529/biophysj.105.076851.

[25] Rees F. Garmann, Mauricio Comas-Garcia, Charles M. Knobler, and William M. Gelbart. Physical Principles in the Self-Assembly of a Simple Spherical Virus. *Accounts of chemical research*, 49(1):48–55, January 2016. ISSN 1520-4898 0001-4842. doi: 10.1021/acs.accounts.5b00350. Place: United States.

[26] Xianxun Sun and Zongqiang Cui. Virus-Like Particles as Theranostic Platforms. *Advanced Therapeutics*, 3(5):1900194, May 2020. doi: 10.1002/adtp.201900194. URL https://doi.org/10.1002/adtp.201900194. Publisher: John Wiley & Sons, Ltd.

[27] Mark B. van Eldijk, Joseph C.-Y. Wang, Inge J. Minten, Chenglei Li, Adam Zlotnick, Roeland J. M. Nolte, Jeroen J. L. M. Cornelissen, and Jan C. M. van Hest. Designing two self-assembly mechanisms into one viral capsid protein. *Journal of the American Chemical Society*, 134(45):18506–18509, November 2012. ISSN 1520-5126 0002-7863. doi: 10.1021/ja308132z.

[28] Dan W. Urry. Physical Chemistry of Biological Free Energy Transduction As Demonstrated by Elastic Protein-Based Polymers. *The Journal of Physical Chemistry B*, 101 (51):11007–11028, December 1997. ISSN 1520-6106. doi: 10.1021/jp972167t. URL https://doi.org/10.1021/jp972167t. Publisher: American Chemical Society.

[29] Suzanne B. P. E. Timmermans, Daan F. M. Vervoort, Lise Schoonen, Roeland J. M. Nolte, and Jan C. M. van Hest. Self-Assembly and Stabilization of Hybrid Cowpea Chlorotic Mottle Virus Particles under Nearly Physiological Conditions. *Chemistry, an Asian journal*, 13(22):3518–3525, November 2018. ISSN 1861-471X. doi: 10.1002/asia.201800842. Place: Germany.

[30] Lise Schoonen, Roel J.M. Maas, Roeland J.M. Nolte, and Jan C.M. van Hest. Expansion of the assembly of cowpea chlorotic mottle virus towards non-native and physiological conditions. *In honor of Professor Ben L. Feringa; 2016 Tetrahedron Prize for Creativity in Organic Chemistry; 'Dynamic Functional Molecular Systems'*, 73(33):4968–4971, August 2017. ISSN 0040-4020. doi: 10.1016/j.tet.2017.04.038. URL https://www.sciencedirect.com/science/article/pii/S0040402017304210.

[31] Suzanne Barbara Pascale Emile Timmermans. *Artificial organelles based on hybrid protein nanoparticles*. PhD thesis, Chemical Engineering and Chemistry, April 2022. Proefschrift.

[32] Sanaz Panahandeh, Siyu Li, Bogdan Dragnea, and Roya Zandi. Virus Assembly Pathways Inside a Host Cell. *ACS Nano*, 16(1):317–327, January 2022. ISSN 1936-0851. doi: 10.1021/acsnano.1c06335. URL https://doi.org/10.1021/acsnano.1c06335. Publisher: American Chemical Society.

[33] Sanaz Panahandeh, Siyu Li, Laurent Marichal, Rafael Leite Rubim, Guillaume Tresset, and Roya Zandi. How a Virus Circumvents Energy Barriers to Form Symmetric Shells. *ACS Nano*, 14(3):3170–3180, March 2020. ISSN 1936-0851. doi: 10.1021/acsnano.9b08354. URL https://doi.org/10.1021/acsnano.9b08354.

Publisher: American Chemical Society.

[34] Sanaz Panahandeh, Siyu Li, and Roya Zandi. The equilibrium structure of self-assembled protein nano-cages. *Nanoscale*, 10(48):22802–22809, December 2018. ISSN 2040-3372 2040-3364. doi: 10.1039/c8nr07202g. Place: England.

[35] Sushmita Singh and Adam Zlotnick. Observed hysteresis of virus capsid disassembly is implicit in kinetic models of assembly. *The Journal of biological chemistry*, 278 (20):18249–18255, May 2003. ISSN 0021-9258. doi: 10.1074/jbc.M211408200. Place: United States.

[36] Paul van der Schoot and Roya Zandi. Kinetic theory of virus capsid assembly. *Physical biology*, 4(4):296–304, November 2007. ISSN 1478-3975 1478-3967. doi: 10.1088/1478-3975/4/4/006. Place: England.

[37] Alireza Ramezani, Samuel Britton, Roya Zandi, Mark Alber, Ali Nematbakhsh, and Weitao Chen. A multiscale chemical-mechanical model predicts impact of morphogen spreading on tissue growth. *npj Systems Biology and Applications*, 9(1):16, May 2023. ISSN 2056-7189. doi: 10.1038/s41540-023-00278-5. URL `https://doi.org/10.1038/s41540-023-00278-5`.

[38] Laura Boulan, Marco Milán, and Pierre Léopold. The Systemic Control of Growth. *Cold Spring Harbor perspectives in biology*, 7(12), August 2015. ISSN 1943-0264. doi: 10.1101/cshperspect.a019117.

[39] Peter J. Bryant and Patrice Levinson. Intrinsic growth control in the imaginal primordia of Drosophila, and the autonomous action of a lethal mutation causing overgrowth. *Developmental Biology*, 107(2):355–363, February 1985. ISSN 0012-1606. doi: 10.1016/0012-1606(85)90317-3. URL `https://www.sciencedirect.com/science/article/pii/0012160685903173`.

[40] Ross G. Harrison. Some Unexpected Results of the Heteroplastic Transplantation of Limbs. *Proceedings of the National Academy of Sciences*, 10(2):69–74, 1924. doi: 10.1073/pnas.10.2.69. URL `https://www.pnas.org/doi/abs/10.1073/pnas.10.2.69`. _eprint: https://www.pnas.org/doi/pdf/10.1073/pnas.10.2.69.

[41] Victor C. Twitty and Joseph L. Schwind. The growth of eyes and limbs transplanted heteroplastically between two species of Amblystoma. *Journal of Experimental Zoology*, 59(1):61–86, 1931. doi: https://doi.org/10.1002/jez.1400590105. URL `https://onlinelibrary.wiley.com/doi/abs/10.1002/jez.1400590105`. _eprint: https://onlinelibrary.wiley.com/doi/pdf/10.1002/jez.1400590105.

[42] Jannik Vollmer, Fernando Casares, and Dagmar Iber. Growth and size control during development. *Open biology*, 7(11), November 2017. ISSN 2046-2441. doi: 10.1098/rsob.170190.

[43] Yilun Zhu, Yuchi Qiu, Weitao Chen, Qing Nie, and Arthur D. Lander. Scaling a Dpp Morphogen Gradient through Feedback Control of Receptors and Co-receptors. *Developmental cell*, 53(6):724–739.e14, June 2020. ISSN 1878-1551 1534-5807. doi: 10.1016/j.devcel.2020.05.029.

[44] Carl-Henrik Heldin, Kohei Miyazono, and Peter ten Dijke. TGF-β signalling from cell membrane to nucleus through SMAD proteins. *Nature*, 390(6659):465–471, December 1997. ISSN 1476-4687. doi: 10.1038/37284. URL `https://doi.org/10.1038/37284`.

[45] Peter M. Siegel and Joan Massagué. Cytostatic and apoptotic actions of TGF-β in homeostasis and cancer. *Nature Reviews Cancer*, 3(11):807–820, November 2003. ISSN 1474-1768. doi: 10.1038/nrc1208. URL `https://doi.org/10.1038/nrc1208`.

[46] S. Bellusci, R. Henderson, G. Winnier, T. Oikawa, and B. L. Hogan. Evidence from normal expression and targeted misexpression that bone morphogenetic protein (Bmp-4) plays a role in mouse embryonic lung morphogenesis. *Development (Cambridge, England)*, 122(6):1693–1702, June 1996. ISSN 0950-1991. Place: England.

[47] M. Hammerschmidt, G. N. Serbedzija, and A. P. McMahon. Genetic analysis of dorsoventral pattern formation in the zebrafish: requirement of a BMP-like ventralizing activity and its dorsal repressor. *Genes & development*, 10(19):2452–2461, October 1996. ISSN 0890-9369. doi: 10.1101/gad.10.19.2452. Place: United States.

[48] C. M. Jones, K. M. Lyons, and B. L. Hogan. Involvement of Bone Morphogenetic Protein-4 (BMP-4) and Vgr-1 in morphogenesis and neurogenesis in the mouse. *Development (Cambridge, England)*, 111(2):531–542, February 1991. ISSN 0950-1991. Place: England.

[49] K. M. Lyons, R. W. Pelton, and B. L. Hogan. Organogenesis and pattern formation in the mouse: RNA distribution patterns suggest a role for bone morphogenetic protein-2A (BMP-2A). *Development (Cambridge, England)*, 109(4):833–844, August 1990. ISSN 0950-1991. Place: England.

[50] JP Martínez-Barberá, H Toresson, S Da Rocha, and S Krauss. Cloning and expression of three members of the zebrafish Bmp family: Bmp2a, Bmp2b and Bmp4. *Gene*, 198(1-2):53–59, October 1997. ISSN 0378-1119. doi: 10.1016/s0378-1119(97)00292-8. URL `https://doi.org/10.1016/s0378-1119(97)00292-8`.

[51] H. Ide, T. Yoshida, N. Matsumoto, K. Aoki, Y. Osada, T. Sugimura, and M. Terada. Growth regulation of human prostate cancer cells by bone morphogenetic protein-2. *Cancer research*, 57(22):5022–5027, November 1997. ISSN 0008-5472. Place: United States.

[52] Guang-Quan Zhao. Consequences of knocking out BMP signaling in the mouse. *Genesis (New York, N.Y. : 2000)*, 35(1):43–56, January 2003. ISSN 1526-954X. doi: 10.1002/gene.10167. Place: United States.

[53] S. Chien, S. Li, and Y. J. Shyy. Effects of mechanical forces on signal transduction and gene expression in endothelial cells. *Hypertension (Dallas, Tex. : 1979)*, 31(1 Pt 2):162–169, January 1998. ISSN 0194-911X. doi: 10.1161/01.hyp.31.1.162. Place: United States.

[54] Sui Huang and Donald E. Ingber. The structural and mechanical complexity of cell-growth control. *Nature Cell Biology*, 1(5):E131–E138, September 1999. ISSN 1476-4679. doi: 10.1038/13043. URL `https://doi.org/10.1038/13043`.

[55] R. Huiskes, R. Ruimerman, G. H. van Lenthe, and J. D. Janssen. Effects of mechanical forces on maintenance and adaptation of form in trabecular bone. *Nature*, 405(6787): 704–706, June 2000. ISSN 0028-0836. doi: 10.1038/35015116. Place: England.

[56] Rakesh K. Jain, John D. Martin, and Triantafyllos Stylianopoulos. The role of mechanical forces in tumor growth and therapy. *Annual review of biomedical engineering*, 16:321–346, July 2014. ISSN 1545-4274 1523-9829. doi: 10.1146/annurev-bioeng-071813-105259.

[57] J. A. Kitterman. The effects of mechanical forces on fetal lung growth. *Clinics in perinatology*, 23(4):727–740, December 1996. ISSN 0095-5108. Place: United States.

[58] Yanlan Mao, Alexander L. Tournier, Andreas Hoppe, Lennart Kester, Barry J. Thompson, and Nicolas Tapon. Differential proliferation rates generate patterns of mechanical tension that orient tissue growth. *The EMBO journal*, 32(21):2790–2803, October 2013. ISSN 1460-2075 0261-4189. doi: 10.1038/emboj.2013.197.

[59] Nicolas Minc, Arezki Boudaoud, and Fred Chang. Mechanical forces of fission yeast growth. *Current biology : CB*, 19(13):1096–1101, July 2009. ISSN 1879-0445 0960-9822. doi: 10.1016/j.cub.2009.05.031.

[60] Boris I. Shraiman. Mechanical feedback as a possible regulator of tissue growth. *Proceedings of the National Academy of Sciences of the United States of America*, 102 (9):3318, March 2005. doi: 10.1073/pnas.0404782102. URL `http://www.pnas.org/content/102/9/3318.abstract`.

[61] Yuanwang Pan, Idse Heemskerk, Consuelo Ibar, Boris I. Shraiman, and Kenneth D. Irvine. Differential growth triggers mechanical feedback that elevates Hippo signaling. *Proceedings of the National Academy of Sciences*, 113(45):E6974, November 2016. doi: 10.1073/pnas.1615012113. URL `http://www.pnas.org/content/113/45/E6974.abstract`.

[62] Justin Werfel, Silva Krause, Ashley G. Bischof, Robert J. Mannix, Heather Tobin, Yaneer Bar-Yam, Robert M. Bellin, and Donald E. Ingber. How changes in extracellular matrix mechanics and gene expression variability might combine to drive cancer progression. *PloS one*, 8(10):e76122, 2013. ISSN 1932-6203. doi: 10.1371/journal.pone.0076122.

[63] William T. Gibson, Boris Y. Rubinstein, Emily J. Meyer, James H. Veldhuis, G. Wayne Brodland, Radhika Nagpal, and Matthew C. Gibson. On the origins of the mitotic shift in proliferating cell layers. *Theoretical biology & medical modelling*, 11:26, May 2014. ISSN 1742-4682. doi: 10.1186/1742-4682-11-26.

[64] Andrius Masedunskas, Monika Sramkova, Laura Parente, Katiuchia Uzzun Sales, Panomwat Amornphimoltham, Thomas H. Bugge, and Roberto Weigert. Role for the actomyosin complex in regulated exocytosis revealed by intravital microscopy. *Proceedings of the National Academy of Sciences*, 108(33):13552–13557, 2011. doi: 10.1073/pnas.1016778108. URL `https://www.pnas.org/doi/abs/10.1073/pnas.1016778108`. _eprint: https://www.pnas.org/doi/pdf/10.1073/pnas.1016778108.

[65] Franz Meitinger and Saravanan Palani. Actomyosin ring driven cytokinesis in budding yeast. *Cytokinetic ring construction and constriction*, 53:19–27, May 2016. ISSN 1084-9521. doi: 10.1016/j.semcdb.2016.01.043. URL `https://www.sciencedirect.com/science/article/pii/S1084952116300404`.

[66] Thomas J. Widmann and Christian Dahmann. Dpp signaling promotes the cuboidal-to-columnar shape transition of Drosophila wing disc epithelia by regulating Rho1. *Journal of cell science*, 122(Pt 9):1362–1373, May 2009. ISSN 0021-9533. doi: 10.1242/jcs.044271. Place: England.

[67] O. Wartlick, P. Mumcu, A. Kicheva, T. Bittig, C. Seum, F. Jülicher, and M. González-Gaitán. Dynamics of Dpp signaling and proliferation control. *Science (New York,*

N.Y.), 331(6021):1154–1159, March 2011. ISSN 1095-9203 0036-8075. doi: 10.1126/science.1200037. Place: United States.

[68] Takuya Akiyama and Matthew C. Gibson. Decapentaplegic and growth control in the developing Drosophila wing. *Nature*, 527(7578):375–378, November 2015. ISSN 1476-4687 0028-0836. doi: 10.1038/nature15730. Place: England.

[69] Ching-Shan Chou, Wing-Cheong Lo, Kimberly K. Gokoffski, Yong-Tao Zhang, Frederic Y. M. Wan, Arthur D. Lander, Anne L. Calof, and Qing Nie. Spatial dynamics of multistage cell lineages in tissue stratification. *Biophysical journal*, 99(10):3145–3154, November 2010. ISSN 1542-0086 0006-3495. doi: 10.1016/j.bpj.2010.09.034.

[70] Huijing Du, Qing Nie, and William R. Holmes. The Interplay between Wnt Mediated Expansion and Negative Regulation of Growth Promotes Robust Intestinal Crypt Structure and Homeostasis. *PLoS computational biology*, 11(8):e1004285, August 2015. ISSN 1553-7358 1553-734X. doi: 10.1371/journal.pcbi.1004285.

[71] Wing-Cheong Lo, Ching-Shan Chou, Kimberly K. Gokoffski, Frederic Y.-M. Wan, Arthur D. Lander, Anne L. Calof, and Qing Nie. Feedback regulation in multistage cell lineages. *Mathematical biosciences and engineering : MBE*, 6(1):59–82, January 2009. ISSN 1547-1063 1551-0018. doi: 10.3934/mbe.2009.6.59.

[72] Lei Zhang, Arthur D. Lander, and Qing Nie. A reaction-diffusion mechanism influences cell lineage progression as a basis for formation, regeneration, and stability of intestinal crypts. *BMC systems biology*, 6:93, July 2012. ISSN 1752-0509. doi: 10.1186/1752-0509-6-93.

[73] John A. Adam. A simplified mathematical model of tumor growth. *Mathematical Biosciences*, 81(2):229–244, 1986. ISSN 0025-5564. doi: https://doi.org/10.1016/0025-5564(86)90119-7. URL `https://www.sciencedirect.com/science/article/pii/0025556486901197`.

[74] Vittorio Cristini, John Lowengrub, and Qing Nie. Nonlinear simulation of tumor growth. *Journal of mathematical biology*, 46(3):191–224, March 2003. ISSN 0303-6812. doi: 10.1007/s00285-002-0174-6. Place: Germany.

[75] S. M. Wise, J. S. Lowengrub, H. B. Frieboes, and V. Cristini. Three-dimensional multispecies nonlinear tumor growth–I Model and numerical method. *Journal of theoretical biology*, 253(3):524–543, August 2008. ISSN 1095-8541 0022-5193. doi: 10.1016/j.jtbi.2008.03.027.

[76] Jeremy Ovadia and Qing Nie. Stem Cell Niche Structure as an Inherent Cause of Undulating Epithelial Morphologies. *Biophysical Journal*, 104(1):237–246, January 2013. ISSN 0006-3495. doi: 10.1016/j.bpj.2012.11.3807. URL https://www.sciencedirect.com/science/article/pii/S0006349512050540.

[77] Charles S. Peskin. The immersed boundary method. *Acta Numerica*, 11:479–517, 2002. doi: 10.1017/S0962492902000077. Publisher: Cambridge University Press.

[78] Stanley Osher and James A. Sethian. Fronts propagating with curvature-dependent speed: Algorithms based on Hamilton-Jacobi formulations. *Journal of Computational Physics*, 79(1):12–49, 1988. ISSN 0021-9991. doi: https://doi.org/10.1016/0021-9991(88)90002-2. URL https://www.sciencedirect.com/science/article/pii/0021999188900022.

[79] Chad M. Glen, Melissa L. Kemp, and Eberhard O. Voit. Agent-based modeling of morphogenetic systems: Advantages and challenges. *PLoS computational biology*, 15 (3):e1006577, March 2019. ISSN 1553-7358 1553-734X. doi: 10.1371/journal.pcbi.1006577. Place: United States.

[80] Xu Dong, Panagiota T. Foteinou, Steven E. Calvano, Stephen F. Lowry, and Ioannis P. Androulakis. Agent-based modeling of endotoxin-induced acute inflammatory response in human blood leukocytes. *PloS one*, 5(2):e9249, February 2010. ISSN 1932-6203. doi: 10.1371/journal.pone.0009249. Place: United States.

[81] Reza Farhadifar, Jens-Christian Röper, Benoit Aigouy, Suzanne Eaton, and Frank Jülicher. The influence of cell mechanics, cell-cell interactions, and proliferation on epithelial packing. *Current biology : CB*, 17(24):2095–2104, December 2007. ISSN 0960-9822. doi: 10.1016/j.cub.2007.11.049. Place: England.

[82] M. Misra, B. Audoly, and S. Y. Shvartsman. Complex structures from patterned cell sheets. *Philosophical transactions of the Royal Society of London. Series B, Biological sciences*, 372(1720), May 2017. ISSN 1471-2970 0962-8436. doi: 10.1098/rstb.2015.0515. Place: England.

[83] Ali Nematbakhsh, Wenzhao Sun, Pavel A. Brodskiy, Aboutaleb Amiri, Cody Narciso, Zhiliang Xu, Jeremiah J. Zartman, and Mark Alber. Multi-scale computational study of the mechanical regulation of cell mitotic rounding in epithelia. *PLOS Computational Biology*, 13(5):e1005533, May 2017. ISSN 1553-7358. doi: 10.1371/journal.pcbi.1005533. URL https://journals.plos.org/ploscompbiol/article?id=10.1371/journal.pcbi.1005533. Number: 5.

[84] George W. Bassel, Petra Stamm, Gabriella Mosca, Pierre Barbier de Reuille, Daniel J. Gibbs, Robin Winter, Ales Janka, Michael J. Holdsworth, and Richard S. Smith. Mechanical constraints imposed by 3D cellular geometry and arrangement modulate growth patterns in the Arabidopsis embryo. *Proceedings of the National Academy of Sciences of the United States of America*, 111(23):8685–8690, June 2014. ISSN 1091-6490 0027-8424. doi: 10.1073/pnas.1404616111. Place: United States.

[85] Vito Conte, José J. Muñoz, and Mark Miodownik. A 3D finite element model of ventral furrow invagination in the Drosophila melanogaster embryo. *Journal of the mechanical behavior of biomedical materials*, 1(2):188–198, April 2008. ISSN 1878-0180. doi: 10.1016/j.jmbbm.2007.10.002. Place: Netherlands.

[86] Arne Keller, Flavio Lanfranconi, and Christof M. Aegerter. The influence of geometry on the elastic properties of the Drosophila wing disc. *Physica A: Statistical Mechanics and its Applications*, 510:208–218, November 2018. ISSN 0378-4371. doi: 10.1016/j.physa.2018.06.106. URL `http://www.sciencedirect.com/science/article/pii/S0378437118308306`.

[87] Nan Luo, An Yan, Gang Liu, Jingzhe Guo, Duoyan Rong, Masahiro M. Kanaoka, Zhen Xiao, Guanshui Xu, Tetsuya Higashiyama, Xinping Cui, and Zhenbiao Yang. Exocytosis-coordinated mechanisms for tip growth underlie pollen tube growth guidance. *Nature communications*, 8(1):1687, November 2017. ISSN 2041-1723. doi: 10.1038/s41467-017-01452-0. Place: England.

[88] Tinri Aegerter-Wilmsen, Maria B. Heimlicher, Alister C. Smith, Pierre Barbier de Reuille, Richard S. Smith, Christof M. Aegerter, and Konrad Basler. Integrating force-sensing and signaling pathways in a model for the regulation of wing imaginal disc size. *Development (Cambridge, England)*, 139(17):3221–3231, September 2012. ISSN 1477-9129 0950-1991. doi: 10.1242/dev.082800. Place: England.

[89] Simon Tanaka, David Sichau, and Dagmar Iber. LBIBCell: a cell-based simulation environment for morphogenetic problems. *Bioinformatics (Oxford, England)*, 31 (14):2340–2347, July 2015. ISSN 1367-4811 1367-4803. doi: 10.1093/bioinformatics/btv147. Place: England.

[90] T. J. Newman. Modeling multicellular systems using subcellular elements. *Mathematical biosciences and engineering : MBE*, 2(3):613–624, July 2005. ISSN 1547-1063. doi: 10.3934/mbe.2005.2.613. Place: United States.

[91] Sebastian A. Sandersius and Timothy J. Newman. Modeling cell rheology with the Subcellular Element Model. *Physical biology*, 5(1):015002, April 2008. ISSN 1478-3975

1478-3967. doi: 10.1088/1478-3975/5/1/015002. Place: England.

[92] R. Burke and K. Basler. Dpp receptors are autonomously required for cell proliferation in the entire developing Drosophila wing. *Development (Cambridge, England)*, 122 (7):2261–2269, July 1996. ISSN 0950-1991. Place: England.

[93] Patrick Fried and Dagmar Iber. Dynamic scaling of morphogen gradients on growing domains. *Nature Communications*, 5(1):5077, October 2014. ISSN 2041-1723. doi: 10.1038/ncomms6077. URL `https://doi.org/10.1038/ncomms6077`.

[94] Matthew C. Gibson and Norbert Perrimon. Extrusion and death of DPP/BMP-compromised epithelial cells in the developing Drosophila wing. *Science (New York, N.Y.)*, 307(5716):1785–1789, March 2005. ISSN 1095-9203 0036-8075. doi: 10.1126/science.1104751. Place: United States.

[95] Stefan Harmansa, Fisun Hamaratoglu, Markus Affolter, and Emmanuel Caussinus. Dpp spreading is required for medial but not for lateral wing disc growth. *Nature*, 527(7578):317–322, November 2015. ISSN 1476-4687. doi: 10.1038/nature15712. URL `https://doi.org/10.1038/nature15712`.

[96] Shinya Matsuda and Markus Affolter. Dpp from the anterior stripe of cells is crucial for the growth of the Drosophila wing disc. *eLife*, 6, July 2017. ISSN 2050-084X. doi: 10.7554/eLife.22319.

[97] Jie Shen and Christian Dahmann. Extrusion of cells with inappropriate Dpp signaling from Drosophila wing disc epithelia. *Science (New York, N.Y.)*, 307(5716):1789–1790, March 2005. ISSN 1095-9203 0036-8075. doi: 10.1126/science.1104784. Place: United States.

[98] A. A. Teleman and S. M. Cohen. Dpp gradient formation in the Drosophila wing imaginal disc. *Cell*, 103(6):971–980, December 2000. ISSN 0092-8674. doi: 10.1016/s0092-8674(00)00199-9. Place: United States.

[99] Shaohua Zhou, Wing-Cheong Lo, Jeffrey L. Suhalim, Michelle A. Digman, Enrico Gratton, Qing Nie, and Arthur D. Lander. Free extracellular diffusion creates the Dpp morphogen gradient of the Drosophila wing disc. *Current biology : CB*, 22(8): 668–675, April 2012. ISSN 1879-0445 0960-9822. doi: 10.1016/j.cub.2012.02.065.

[100] Tinri Aegerter-Wilmsen, Christof M. Aegerter, Ernst Hafen, and Konrad Basler. Model for the regulation of size in the wing imaginal disc of Drosophila. *Mecha-*

nisms of development, 124(4):318–326, April 2007. ISSN 0925-4773. doi: 10.1016/j.mod.2006.12.005. Place: Ireland.

[101] T. Bittig, O. Wartlick, M. González-Gaitán, and F. Jülicher. Quantification of growth asymmetries in developing epithelia. *The European physical journal. E, Soft matter*, 30(1):93–99, September 2009. ISSN 1292-895X 1292-8941. doi: 10.1140/epje/i2009-10507-6. Place: France.

[102] Lars Hufnagel, Aurelio A. Teleman, Hervé Rouault, Stephen M. Cohen, and Boris I. Shraiman. On the mechanism of wing size determination in fly development. *Proceedings of the National Academy of Sciences of the United States of America*, 104(10):3835–3840, March 2007. ISSN 0027-8424 1091-6490. doi: 10.1073/pnas.0607134104.

[103] M. Milán, S. Campuzano, and A. García-Bellido. Cell cycling and patterned cell proliferation in the wing primordium of Drosophila. *Proceedings of the National Academy of Sciences of the United States of America*, 93(2):640–645, January 1996. ISSN 0027-8424 1091-6490. doi: 10.1073/pnas.93.2.640.

[104] Jannik Vollmer and Dagmar Iber. An Unbiased Analysis of Candidate Mechanisms for the Regulation of Drosophila Wing Disc Growth. *Scientific reports*, 6:39228, December 2016. ISSN 2045-2322. doi: 10.1038/srep39228.

[105] Sirio Dupont. Role of YAP/TAZ in cell-matrix adhesion-mediated signalling and mechanotransduction. *Experimental cell research*, 343(1):42–53, April 2016. ISSN 1090-2422 0014-4827. doi: 10.1016/j.yexcr.2015.10.034. Place: United States.

[106] Kenneth D. Irvine and Boris I. Shraiman. Mechanical control of growth: ideas, facts and challenges. *Development (Cambridge, England)*, 144(23):4238–4248, December 2017. ISSN 1477-9129 0950-1991. doi: 10.1242/dev.151902.

[107] Shuguo Sun and Kenneth D. Irvine. Cellular Organization and Cytoskeletal Regulation of the Hippo Signaling Network. *Trends in cell biology*, 26(9):694–704, September 2016. ISSN 1879-3088 0962-8924. doi: 10.1016/j.tcb.2016.05.003.

[108] Scott Christley, Briana Lee, Xing Dai, and Qing Nie. Integrative multicellular biological modeling: a case study of 3D epidermal development using GPU algorithms. *BMC Systems Biology*, 4(1):107, August 2010. ISSN 1752-0509. doi: 10.1186/1752-0509-4-107. URL `https://doi.org/10.1186/1752-0509-4-107`.

[109] HOWARD C. BERG and DOUGLAS A. BROWN. Chemotaxis in Escherichia coli analysed by Three-dimensional Tracking. *Nature*, 239(5374):500–504, October 1972. ISSN 1476-4687. doi: 10.1038/239500a0. URL https://doi.org/10.1038/239500a0.

[110] Shuichi Nakamura and Tohru Minamino. Flagella-Driven Motility of Bacteria. *Biomolecules*, 9(7), 2019. ISSN 2218-273X. doi: 10.3390/biom9070279. URL https://www.mdpi.com/2218-273X/9/7/279.

[111] Qiuxian Cai, Zhaojun Li, Qi Ouyang, Chunxiong Luo, and Vernita D. Gordon. Singly Flagellated Pseudomonas aeruginosa Chemotaxes Efficiently by Unbiased Motor Regulation. *mBio*, 7(2):10.1128/mbio.00013–16, 2016. doi: 10.1128/mbio.00013-16. URL https://journals.asm.org/doi/abs/10.1128/mbio.00013-16. _eprint: https://journals.asm.org/doi/pdf/10.1128/mbio.00013-16.

[112] Liyan Ping, Jan Birkenbeil, and Shamci Monajembashi. Swimming behavior of the monotrichous bacterium Pseudomonas fluorescens SBW25. *FEMS microbiology ecology*, 86(1):36–44, October 2013. ISSN 1574-6941 0168-6496. doi: 10.1111/1574-6941.12076. Place: England.

[113] Matthias Theves, Johannes Taktikos, Vasily Zaburdaev, Holger Stark, and Carsten Beta. A Bacterial Swimmer with Two Alternating Speeds of Propagation. *Biophysical Journal*, 105(8):1915–1924, 2013. ISSN 0006-3495. doi: https://doi.org/10.1016/j.bpj.2013.08.047. URL https://www.sciencedirect.com/science/article/pii/S0006349513010217.

[114] Li Xie, Tuba Altindal, Suddhashil Chattopadhyay, and Xiao-Lun Wu. Bacterial flagellum as a propeller and as a rudder for efficient chemotaxis. *Proceedings of the National Academy of Sciences*, 108(6):2246–2251, 2011. doi: 10.1073/pnas.1011953108. URL https://www.pnas.org/doi/abs/10.1073/pnas.1011953108. _eprint: https://www.pnas.org/doi/pdf/10.1073/pnas.1011953108.

[115] Jacque Monod, Jeffries Wyman, and Jean-Pierre Changeux. On the nature of allosteric transitions: A plausible model. *Journal of Molecular Biology*, 12(1):88–118, 1965. ISSN 0022-2836. doi: https://doi.org/10.1016/S0022-2836(65)80285-6. URL https://www.sciencedirect.com/science/article/pii/S0022283665802856.

[116] HOWARD C. BERG and ROBERT A. ANDERSON. Bacteria Swim by Rotating their Flagellar Filaments. *Nature*, 245(5425):380–382, October 1973. ISSN 1476-4687. doi: 10.1038/245380a0. URL https://doi.org/10.1038/245380a0.

[117] R. M. Macnab. Bacterial flagella rotating in bundles: a study in helical geometry. *Proceedings of the National Academy of Sciences of the United States of America*, 74 (1):221–225, January 1977. ISSN 0027-8424 1091-6490. doi: 10.1073/pnas.74.1.221. Place: United States.

[118] MICHAEL SILVERMAN and MELVIN SIMON. Flagellar rotation and the mechanism of bacterial motility. *Nature*, 249(5452):73–74, May 1974. ISSN 1476-4687. doi: 10.1038/249073a0. URL https://doi.org/10.1038/249073a0.

[119] L. Turner, W. S. Ryu, and H. C. Berg. Real-time imaging of fluorescent flagellar filaments. *Journal of bacteriology*, 182(10):2793–2801, May 2000. ISSN 0021-9193 1098-5530. doi: 10.1128/JB.182.10.2793-2801.2000. Place: United States.

[120] Zahra Alirezaeizanjani, Robert Großmann, Veronika Pfeifer, Marius Hintsche, and Carsten Beta. Chemotaxis strategies of bacteria with multiple run modes. *Science advances*, 6(22):eaaz6153, May 2020. ISSN 2375-2548. doi: 10.1126/sciadv.aaz6153. Place: United States.

[121] Marius Hintsche, Veronika Waljor, Robert Großmann, Marco J. Kühn, Kai M. Thormann, Fernando Peruani, and Carsten Beta. A polar bundle of flagella can drive bacterial swimming by pushing, pulling, or coiling around the cell body. *Scientific reports*, 7(1):16771, December 2017. ISSN 2045-2322. doi: 10.1038/s41598-017-16428-9. Place: England.

[122] Maojin Tian, Zhengyu Wu, Rongjing Zhang, and Junhua Yuan. A new mode of swimming in singly flagellated Pseudomonas aeruginosa. *Proceedings of the National Academy of Sciences of the United States of America*, 119(14):e2120508119, April 2022. ISSN 1091-6490 0027-8424. doi: 10.1073/pnas.2120508119. Place: United States.

[123] Yoshiaki Kinosita, Yoshitomo Kikuchi, Nagisa Mikami, Daisuke Nakane, and Takayuki Nishizaka. Unforeseen swimming and gliding mode of an insect gut symbiont, Burkholderia sp. RPE64, with wrapping of the flagella around its cell body. *The ISME Journal*, 12(3):838–848, March 2018. ISSN 1751-7370. doi: 10.1038/s41396-017-0010-z. URL https://doi.org/10.1038/s41396-017-0010-z.

[124] Maira A. Constantino, Mehdi Jabbarzadeh, Henry C. Fu, Zeli Shen, James G. Fox, Freddy Haesebrouck, Sara K. Linden, and Rama Bansil. Bipolar lophotrichous Helicobacter suis combine extended and wrapped flagella bundles to exhibit multiple modes of motility. *Scientific Reports*, 8(1):14415, September 2018. ISSN 2045-2322. doi: 10.1038/s41598-018-32686-7. URL https://doi.org/10.1038/

s41598-018-32686-7.

[125] Eli J. Cohen, Daisuke Nakane, Yoshiki Kabata, David R. Hendrixson, Takayuki Nishizaka, and Morgan Beeby. Campylobacter jejuni motility integrates specialized cell shape, flagellar filament, and motor, to coordinate action of its opposed flagella. *PLOS Pathogens*, 16(7):1–24, July 2020. doi: 10.1371/journal.ppat.1008620. URL https://doi.org/10.1371/journal.ppat.1008620. Publisher: Public Library of Science.

[126] Aboutaleb Amiri, Cameron Harvey, Amy Buchmann, Scott Christley, Joshua D. Shrout, Igor S. Aranson, and Mark Alber. Reversals and collisions optimize protein exchange in bacterial swarms. *Physical review. E*, 95(3-1):032408, March 2017. ISSN 2470-0053 2470-0045. doi: 10.1103/PhysRevE.95.032408. Place: United States.

[127] R. N. Bearon and W. M. Durham. A model of strongly biased chemotaxis reveals the trade-offs of different bacterial migration strategies. *Mathematical medicine and biology : a journal of the IMA*, 37(1):83–116, February 2020. ISSN 1477-8602 1477-8599. doi: 10.1093/imammb/dqz007. Place: England.

[128] Katrina Hui, Guang Lin, and Wenxiao Pan. Understanding the mechanisms of sickle cell disease by simulations with a discrete particle model. *Computational Science & Discovery*, 6(1):015004, February 2013. doi: 10.1088/1749-4699/6/1/015004. URL https://dx.doi.org/10.1088/1749-4699/6/1/015004. Publisher: IOP Publishing.

[129] Yi-Wei Tang, Max Sussman, Dongyou Liu, Ian R. Poxton, and Joseph D. Schwartzman. Chapter 1 - Molecular Medical Microbiology – The Expanding Concept. In Yi-Wei Tang, Max Sussman, Dongyou Liu, Ian Poxton, and Joseph Schwartzman, editors, *Molecular Medical Microbiology (Second Edition)*, pages 1–4. Academic Press, Boston, January 2015. ISBN 978-0-12-397169-2. doi: 10.1016/B978-0-12-397169-2.00001-9. URL https://www.sciencedirect.com/science/article/pii/B9780123971692000019.

[130] Roya Zandi, David Reguera, Robijn Bruinsma, William Gelbart, and Joseph Rudnick. Assembly and Disassembly of Viral Capsids. *Journal of Theoretical Medicine*, 6: 263468, January 1900. ISSN 1748-670X. doi: 10.1080/10273660500149166. URL https://doi.org/10.1080/10273660500149166. Publisher: Hindawi Publishing Corporation.

[131] Roya Zandi and David Reguera. Mechanical properties of viral capsids. *Phys. Rev. E*, 72(2):021917, August 2005. doi: 10.1103/PhysRevE.72.021917. URL https://link.aps.org/doi/10.1103/PhysRevE.72.021917. Publisher: American Physical Society.

[132] Inge J. Minten, Koos D. M. Wilke, Linda J. A. Hendriks, Jan C. M. van Hest, Roeland J. M. Nolte, and Jeroen J. L. M. Cornelissen. Metal-ion-induced formation and stabilization of protein cages based on the cowpea chlorotic mottle virus. *Small (Weinheim an der Bergstrasse, Germany)*, 7(7):911–919, April 2011. ISSN 1613-6829 1613-6810. doi: 10.1002/smll.201001777. Place: Germany.

[133] M. Cuillel, C. Berthet-Colominas, B. Krop, A. Tardieu, P. Vachette, and B. Jacrot. Self-assembly of brome mosaic virus capsids. Kinetic study using neutron and X-ray solution scattering. *Journal of molecular biology*, 164(4):645–650, March 1983. ISSN 0022-2836. doi: 10.1016/0022-2836(83)90055-4. Place: England.

[134] S. C. Gill and P. H. von Hippel. Calculation of protein extinction coefficients from amino acid sequence data. *Analytical biochemistry*, 182(2):319–326, November 1989. ISSN 0003-2697. doi: 10.1016/0003-2697(89)90602-7. Place: United States.

[135] Lise Schoonen, Jan Pille, Annika Borrmann, Roeland J. M. Nolte, and Jan C. M. van Hest. Sortase A-Mediated N-Terminal Modification of Cowpea Chlorotic Mottle Virus for Highly Efficient Cargo Loading. *Bioconjugate chemistry*, 26(12):2429–2434, December 2015. ISSN 1520-4812 1043-1802. doi: 10.1021/acs.bioconjchem.5b00485. Place: United States.

[136] T. J. Newman and R. Grima. Many-body theory of chemotactic cell-cell interactions. *Physical Review E*, 70(5):051916, November 2004. doi: 10.1103/PhysRevE.70.051916. URL `https://link.aps.org/doi/10.1103/PhysRevE.70.051916`. Number: 5.

[137] M. Rahman and D. D. Bhatta. Evaluation of added mass and damping coefficient of an oscillating circular cylinder. *Applied Mathematical Modelling*, 17(2):70–79, February 1993. ISSN 0307-904X. doi: 10.1016/0307-904X(93)90095-X. URL `http://www.sciencedirect.com/science/article/pii/0307904X9390095X`. Number: 2.

[138] Walter Musial and Bonnie Ram. Large-Scale Offshore Wind Power in the United States. Assessment of Opportunities and Barriers. Technical Report NREL/TP–500-40745, National Renewable Energy Lab. (NREL), Golden, CO (United States), September 2010. URL `http://www.osti.gov/scitech/biblio/1219151`. Issue: NREL/TP–500-40745.

[139] Emily J. Meyer, Aissam Ikmi, and Matthew C. Gibson. Interkinetic Nuclear Migration Is a Broadly Conserved Feature of Cell Division in Pseudostratified Epithelia. *Current Biology*, 21(6):485–491, March 2011. ISSN 0960-9822. doi: 10.1016/j.cub.2011.02.002. URL `http://www.sciencedirect.com/science/article/pii/S0960982211001655`. Number: 6.

[140] Simeone Marino, Ian B. Hogue, Christian J. Ray, and Denise E. Kirschner. A methodology for performing global uncertainty and sensitivity analysis in systems biology. *Journal of Theoretical Biology*, 254(1):178–196, September 2008. ISSN 0022-5193. doi: 10.1016/j.jtbi.2008.04.011. URL http://www.sciencedirect.com/science/article/pii/S0022519308001896. Number: 1.

[141] J. R. Morison, J. W. Johnson, and S. A. Schaaf. The Force Exerted by Surface Waves on Piles. *Journal of Petroleum Technology*, 2(05):149–154, May 1950. ISSN 0149-2136. doi: 10.2118/950149-G. URL https://www.onepetro.org/journal-paper/SPE-950149-G. Number: 05.

[142] Ali Nematbakhsh, David J. Olinger, and Gretar Tryggvason. A Nonlinear Computational Model of Floating Wind Turbines. *Journal of Fluids Engineering*, 135(12): 121103–121103, September 2013. ISSN 0098-2202. doi: 10.1115/1.4025074. URL http://dx.doi.org/10.1115/1.4025074. Number: 12.

[143] Thierry Savin, Natasza A. Kurpios, Amy E. Shyer, Patricia Florescu, Haiyi Liang, L. Mahadevan, and Clifford J. Tabin. On the growth and form of the gut. *Nature*, 476(7358):57–62, August 2011. ISSN 1476-4687. doi: 10.1038/nature10277. URL https://www.nature.com/articles/nature10277. Number: 7358.

[144] Zhangli Peng, Xuejin Li, Igor V. Pivkin, Ming Dao, George E. Karniadakis, and Subra Suresh. Lipid bilayer and cytoskeletal interactions in a red blood cell. *Proceedings of the National Academy of Sciences*, 110(33):13356–13361, August 2013. ISSN 0027-8424, 1091-6490. doi: 10.1073/pnas.1311827110. URL https://www.pnas.org/content/110/33/13356. Number: 33.

[145] Veritas, N. *Environmental conditions and environmental loads*. DNV-GL, 2000.

[146] RG Dean and RA Dalrymple. *Water wave mechanics for engineers and scientists*. World Scientific., 1991.

[147] Fletcher Alexander G., Cooper Fergus, and Baker Ruth E. Mechanocellular models of epithelial morphogenesis. *Philosophical Transactions of the Royal Society B: Biological Sciences*, 372(1720):20150519, May 2017. doi: 10.1098/rstb.2015.0519. URL https://royalsocietypublishing.org/doi/full/10.1098/rstb.2015.0519. Number: 1720.

[148] O. Faltinsen. *Sea Loads on Ships and Offshore Structures*. Cambridge University Press, September 1993. ISBN 978-0-521-45870-2.

[149] Matteo Rauzi, Pascale Verant, Thomas Lecuit, and Pierre-François Lenne. Nature and anisotropy of cortical forces orienting Drosophila tissue morphogenesis. *Nature Cell Biology*, 10(12):1401–1410, December 2008. ISSN 1465-7392. doi: 10.1038/ncb1798. URL http://www.nature.com/ncb/journal/v10/n12/abs/ncb1798.html. Number: 12.

[150] Ivan Niven. *Maxima and Minima Without Calculus*. Cambridge University Press, 1981. ISBN 978-0-88385-306-1. Google-Books-ID: ImKbYaS2KzwC.

[151] G. M. Odell, G. Oster, P. Alberch, and B. Burnside. The mechanical basis of morphogenesis: I. Epithelial folding and invagination. *Developmental Biology*, 85(2):446–462, July 1981. ISSN 0012-1606. doi: 10.1016/0012-1606(81)90276-1. URL http://www.sciencedirect.com/science/article/pii/0012160681902761. Number: 2.

[152] Zhiliang Xu, Nan Chen, Malgorzata M Kamocka, Elliot D Rosen, and Mark Alber. A multiscale model of thrombus development. *Journal of The Royal Society Interface*, 5(24):705–722, July 2008. doi: 10.1098/rsif.2007.1202. URL https://royalsocietypublishing.org/doi/full/10.1098/rsif.2007.1202. Number: 24.

[153] John Nicholas Newman. *Marine Hydrodynamics*. MIT Press, January 1977. ISBN 978-0-262-14026-3.

[154] Amarendra Badugu and Andres Käch. Independent apical and basal mechanical systems determine cell and tissue shape in the Drosophila wing disc. *bioRxiv*, page 2020.04.10.036152, April 2020. doi: 10.1101/2020.04.10.036152. URL https://www.biorxiv.org/content/10.1101/2020.04.10.036152v1.

[155] James F. Wilson. *Dynamics of Offshore Structures*. John Wiley & Sons, January 2003. ISBN 978-0-471-27565-7.

[156] Davide Heller, Andreas Hoppe, Simon Restrepo, Lorenzo Gatti, Alexander L. Tournier, Nicolas Tapon, Konrad Basler, and Yanlan Mao. EpiTools: An Open-Source Image Analysis Toolkit for Quantifying Epithelial Growth Dynamics. *Developmental Cell*, 36(1):103–116, January 2016. ISSN 1534-5807. doi: 10.1016/j.devcel.2015.12.012. URL http://www.cell.com/developmental-cell/abstract/S1534-5807(15)00797-2. Number: 1.

[157] Ira Herbert Abbott and Albert Edward Von Doenhoff. *Theory of Wing Sections, Including a Summary of Airfoil Data*. Courier Corporation, 1959. ISBN 978-0-486-60586-9.

[158] O. M. Faltinsen, J. N. Newman, and T. Vinje. Nonlinear wave loads on a slender vertical cylinder. *Journal of Fluid Mechanics*, 289:179–198, April 1995. ISSN 1469-7645. doi: 10.1017/S0022112095001297. URL http://journals.cambridge.org/article_S0022112095001297.

[159] LH Carpenter. On the motion of two cylinders in an ideal fluid. *Journal of Research of the National Bureau of Standards*, 61(2):83–87, 1958. Number: 2.

[160] Robert W. Fox and Alan T. Mcdonald. *Introduction to fluid mechanics*. John Wiley, 1994. ISBN 978-0-471-59274-7. URL https://infoscience.epfl.ch/record/24502.

[161] Kimberly D. McClure and Gerold Schubiger. Developmental analysis and squamous morphogenesis of the peripodial epithelium in Drosophila imaginal discs. *Development*, 132(22):5033–5042, November 2005. ISSN 0950-1991, 1477-9129. doi: 10.1242/dev.02092. URL http://dev.biologists.org/content/132/22/5033. Number: 22.

[162] N. E. Kochin, I. A. Kibel, N. V. Roze, and W. R. Dean. Theoretical Hydrodynamics. *Journal of Applied Mechanics*, 33:237, 1966. doi: 10.1115/1.3625011. URL http://adsabs.harvard.edu/abs/1966JAM....33..237K.

[163] Subrata Kumar Chakrabarti. *Hydrodynamics of Offshore Structures*. WIT Press, 1987. ISBN 978-0-905451-66-4.

[164] K Hasselmann, TP Barnett, E Bouws, H Carlson, DE Cartwright, K Enke, JA Ewing, H Gienapp, DE Hasselmann, P Kruseman, A Meerburg, P M{ü}ller, DJ Olbers, K Richter, W Sell, and H Walden. Measurements of wind-wave growth and swell decay during the {Joint North Sea Wave Project}. *Deut. Hydrogr. Z.*, 8(12):1–95, 1973. Number: 12.

[165] James F. Manwell, Jon G. McGowan, and Anthony L. Rogers. *Wind Energy Explained: Theory, Design and Application*. John Wiley & Sons, September 2010. ISBN 978-0-470-68628-7.

[166] Lienhard. *Synopsis of lift, drag, and vortex frequency data for rigid circular cylinders*. Technical Extension Service, Washington State University., 1966.

[167] J. Li, M. Dao, C. T. Lim, and S. Suresh. Spectrin-Level Modeling of the Cytoskeleton and Optical Tweezers Stretching of the Erythrocyte. *Biophysical Journal*, 88(5):3707–3719, May 2005. ISSN 0006-3495. doi: 10.1529/biophysj.104.047332. URL http:

//www.sciencedirect.com/science/article/pii/S0006349505734196. Number: 5.

[168] Paul D. Sclavounos. Nonlinear impulse of ocean waves on floating bodies. *Journal of Fluid Mechanics*, 697:316–335, April 2012. ISSN 1469-7645. doi: 10.1017/jfm.2012.68. URL http://journals.cambridge.org/article_S0022112012000687.

[169] John H. Nath and Tokuo Yamamoto. Forces from Fluid Flow around Objects. In *Coastal Engineering 1974*, pages 1808–1827. American Society of Civil Engineers, July 2016. ISBN 978-0-87262-113-8. URL http://ascelibrary.org/doi/abs/10.1061/9780872621138.109.

[170] Takefumi Kondo and Shigeo Hayashi. Mitotic cell rounding accelerates epithelial invagination. *Nature*, 494(7435):125–129, February 2013. ISSN 0028-0836. doi: 10.1038/nature11792. URL http://www.nature.com/nature/journal/v494/n7435/abs/nature11792.html. Number: 7435.

[171] Jeffrey Settleman. Rac 'n Rho: The Music that Shapes a Developing Embryo. *Developmental Cell*, 1(3):321–331, September 2001. ISSN 1534-5807. doi: 10.1016/S1534-5807(01)00053-3. URL http://www.sciencedirect.com/science/article/pii/S1534580701000533. Number: 3.

[172] S. A. Sandersius, C. J. Weijer, and T. J. Newman. Emergent cell and tissue dynamics from subcellular modeling of active biomechanical processes. *Physical Biology*, 8(4):045007, July 2011. ISSN 1478-3975. doi: 10.1088/1478-3975/8/4/045007. URL https://doi.org/10.1088%2F1478-3975%2F8%2F4%2F045007. Number: 4.

[173] Melda Tozluoğlu, Maria Duda, Natalie J. Kirkland, Ricardo Barrientos, Jemima J. Burden, José J. Muñoz, and Yanlan Mao. Planar Differential Growth Rates Initiate Precise Fold Positions in Complex Epithelia. *Developmental Cell*, 51(3):299–312.e4, November 2019. ISSN 1534-5807. doi: 10.1016/j.devcel.2019.09.009. URL http://www.sciencedirect.com/science/article/pii/S1534580719307385. Number: 3.

[174] Anatol Roshko. Experiments on the flow past a circular cylinder at very high Reynolds number. *Journal of Fluid Mechanics*, 10(03):345–356, May 1961. ISSN 1469-7645. doi: 10.1017/S0022112061000950. URL http://journals.cambridge.org/article_S0022112061000950. Number: 03.

[175] Amarendra Badugu and Andres Käch. Cytoplasmic flows caused by actomyosin contraction drive interkinetic nuclear migration. *bioRxiv*, page 2020.04.09.034660, April

2020. doi: 10.1101/2020.04.09.034660. URL https://www.biorxiv.org/content/10.1101/2020.04.09.034660v1.

[176] Q. Ouyang and Harry L. Swinney. Transition from a uniform state to hexagonal and striped Turing patterns. *Nature*, 352(6336):610–612, August 1991. ISSN 1476-4687. doi: 10.1038/352610a0. URL https://doi.org/10.1038/352610a0.

[177] P. J. Bryant. Pattern formation in the imaginal wing disc of Drosophila melanogaster: fate map, regeneration and duplication. *The Journal of experimental zoology*, 193(1): 49–77, July 1975. ISSN 0022-104X. doi: 10.1002/jez.1401930106. Place: United States.

[178] J. A. Williams, J. B. Bell, and S. B. Carroll. Control of Drosophila wing and haltere development by the nuclear vestigial gene product. *Genes & development*, 5(12B): 2481–2495, December 1991. ISSN 0890-9369. doi: 10.1101/gad.5.12b.2481. Place: United States.

[179] L. Wolpert. Positional information and the spatial pattern of cellular differentiation. *Journal of theoretical biology*, 25(1):1–47, October 1969. ISSN 0022-5193. doi: 10.1016/s0022-5193(69)80016-0. Place: England.

[180] Julyan H. E. Cartwright. Labyrinthine Turing pattern formation in the cerebral cortex. *Journal of theoretical biology*, 217(1):97–103, July 2002. ISSN 0022-5193. doi: 10.1006/jtbi.2002.3012. Place: England.

[181] Ian K. Quigley and David M. Parichy. Pigment pattern formation in zebrafish: a model for developmental genetics and the evolution of form. *Microscopy research and technique*, 58(6):442–455, September 2002. ISSN 1059-910X. doi: 10.1002/jemt.10162. Place: United States.

[182] E. A. Gaffney and N. A. M. Monk. Gene expression time delays and Turing pattern formation systems. *Bulletin of mathematical biology*, 68(1):99–130, January 2006. ISSN 0092-8240. doi: 10.1007/s11538-006-9066-z. Place: United States.

[183] Matthew C. Gibson, Ankit B. Patel, Radhika Nagpal, and Norbert Perrimon. The emergence of geometric order in proliferating metazoan epithelia. *Nature*, 442(7106): 1038–1041, August 2006. ISSN 1476-4687 0028-0836. doi: 10.1038/nature05014. Place: England.

[184] Philip K. Maini, Ruth E. Baker, and Cheng-Ming Chuong. Developmental biology. The Turing model comes of molecular age. *Science (New York, N.Y.)*, 314(5804): 1397–1398, December 2006. ISSN 1095-9203 0036-8075. doi: 10.1126/science.1136396.

[185] Koichiro Uriu and Yoh Iwasa. Turing pattern formation with two kinds of cells and a diffusive chemical. *Bulletin of mathematical biology*, 69(8):2515–2536, November 2007. ISSN 0092-8240. doi: 10.1007/s11538-007-9230-0. Place: United States.

[186] Shigeru Kondo and Takashi Miura. Reaction-diffusion model as a framework for understanding biological pattern formation. *Science (New York, N.Y.)*, 329(5999):1616–1620, September 2010. ISSN 1095-9203 0036-8075. doi: 10.1126/science.1179047. Place: United States.

[187] Jochen Kursawe, Pavel A. Brodskiy, Jeremiah J. Zartman, Ruth E. Baker, and Alexander G. Fletcher. Capabilities and Limitations of Tissue Size Control through Passive Mechanical Forces. *PLoS computational biology*, 11(12):e1004679, December 2015. ISSN 1553-7358 1553-734X. doi: 10.1371/journal.pcbi.1004679.

[188] Pablo Sanchez Bosch, Ruta Ziukaite, Cyrille Alexandre, Konrad Basler, and Jean-Paul Vincent. Dpp controls growth and patterning in Drosophila wing precursors through distinct modes of action. *eLife*, 6, July 2017. ISSN 2050-084X. doi: 10.7554/eLife.22546.

[189] Mengqi Ma, Xueya Cao, Jianli Dai, and José C. Pastor-Pareja. Basement Membrane Manipulation in Drosophila Wing Discs Affects Dpp Retention but Not Growth Mechanoregulation. *Developmental cell*, 42(1):97–106.e4, July 2017. ISSN 1878-1551 1534-5807. doi: 10.1016/j.devcel.2017.06.004. Place: United States.

[190] Gui-Quan Sun, Guang Zhang, Zhen Jin, and Li Li. Predator cannibalism can give rise to regular spatial pattern in a predator–prey system. *Nonlinear Dynamics*, 58: 75–84, October 2009. doi: 10.1007/s11071-008-9462-z.

[191] A. M. Turing. The chemical basis of morphogenesis. 1953. *Bulletin of mathematical biology*, 52(1-2):153–97; discussion 119–152, 1990. ISSN 0092-8240. doi: 10.1007/BF02459572. Place: United States.

[192] Andrei I. Ivanov, Ingrid C. McCall, Brian Babbin, Stanislav N. Samarin, Asma Nusrat, and Charles A. Parkos. Microtubules regulate disassembly of epithelial apical junctions. *BMC cell biology*, 7:12, March 2006. ISSN 1471-2121. doi: 10.1186/1471-2121-7-12.

[193] Ulrike Nienhaus, Tinri Aegerter-Wilmsen, and Christof M. Aegerter. Determination of mechanical stress distribution in Drosophila wing discs using photoelasticity. *Mechanisms of development*, 126(11-12):942–949, December 2009. ISSN 1872-6356 0925-4773. doi: 10.1016/j.mod.2009.09.002. Place: Ireland.

[194] Mingyuan Zhu, Weiwei Chen, Vincent Mirabet, Lilan Hong, Simone Bovio, Soeren Strauss, Erich M. Schwarz, Satoru Tsugawa, Zhou Wang, Richard S. Smith, Chun-Biu Li, Olivier Hamant, Arezki Boudaoud, and Adrienne H. K. Roeder. Robust organ size requires robust timing of initiation orchestrated by focused auxin and cytokinin signalling. *Nature Plants*, 6(6):686–698, June 2020. ISSN 2055-0278. doi: 10.1038/s41477-020-0666-7. URL `https://doi.org/10.1038/s41477-020-0666-7`.

[195] Yanlan Mao, Alexander L. Tournier, Paul A. Bates, Jonathan E. Gale, Nicolas Tapon, and Barry J. Thompson. Planar polarization of the atypical myosin Dachs orients cell divisions in Drosophila. *Genes & development*, 25(2):131–136, January 2011. ISSN 1549-5477 0890-9369. doi: 10.1101/gad.610511. Place: United States.

[196] Isabelle Benoit, Marielle H. van den Esker, Aleksandrina Patyshakuliyeva, Derek J. Mattern, Felix Blei, Miaomiao Zhou, Jan Dijksterhuis, Axel A. Brakhage, Oscar P. Kuipers, Ronald P. de Vries, and Ákos T. Kovács. Bacillus subtilis attachment to Aspergillus niger hyphae results in mutually altered metabolism. *Environmental Microbiology*, 17(6):2099–2113, 2015. doi: https://doi.org/10.1111/1462-2920.12564. URL `https://sfamjournals.onlinelibrary.wiley.com/doi/abs/10.1111/1462-2920.12564`. _eprint: https://sfamjournals.onlinelibrary.wiley.com/doi/pdf/10.1111/1462-2920.12564.

[197] Breanne N. Steffan, Nandhitha Venkatesh, and Nancy P. Keller. Let's Get Physical: Bacterial-Fungal Interactions and Their Consequences in Agriculture and Health. *Journal of Fungi*, 6(4), 2020. ISSN 2309-608X. doi: 10.3390/jof6040243. URL `https://www.mdpi.com/2309-608X/6/4/243`.

[198] A. Deveau, C. Brulé, B. Palin, D. Champmartin, P. Rubini, J. Garbaye, A. Sarniguet, and P. Frey-Klett. Role of fungal trehalose and bacterial thiamine in the improved survival and growth of the ectomycorrhizal fungus Laccaria bicolor S238N and the helper bacterium Pseudomonas fluorescens BBc6R8. *Environmental Microbiology Reports*, 2(4):560–568, 2010. doi: https://doi.org/10.1111/j.1758-2229.2010.00145.x. URL `https://sfamjournals.onlinelibrary.wiley.com/doi/abs/10.1111/j.1758-2229.2010.00145.x`. _eprint: https://sfamjournals.onlinelibrary.wiley.com/doi/pdf/10.1111/j.1758-2229.2010.00145.x.

[199] Yuanchen Zhang, Erik K. Kastman, Jeffrey S. Guasto, and Benjamin E. Wolfe. Fungal networks shape dynamics of bacterial dispersal and community assembly in cheese rind microbiomes. *Nature communications*, 9(1):336, January 2018. ISSN 2041-1723. doi: 10.1038/s41467-017-02522-z. Place: England.

[200] Tom Berthold, Florian Centler, Thomas Hübschmann, Rita Remer, Martin Thullner, Hauke Harms, and Lukas Y. Wick. Mycelia as a focal point for horizontal gene transfer among soil bacteria. *Scientific reports*, 6:36390, November 2016. ISSN 2045-2322. doi: 10.1038/srep36390. Place: England.

[201] Colin J. Ingham, Oren Kalisman, Alin Finkelshtein, and Eshel Ben-Jacob. Mutually facilitated dispersal between the nonmotile fungus Aspergillus fumigatus and the swarming bacterium Paenibacillus vortex. *Proceedings of the National Academy of Sciences of the United States of America*, 108(49):19731–19736, December 2011. ISSN 1091-6490 0027-8424. doi: 10.1073/pnas.1102097108. Place: United States.

[202] Shota Oku, Ayaka Komatsu, Yutaka Nakashimada, Takahisa Tajima, and Junichi Kato. Identification of Pseudomonas fluorescens chemotaxis sensory proteins for malate, succinate, and fumarate, and their involvement in root colonization. *Microbes and environments*, 29(4):413–419, 2014. ISSN 1347-4405 1342-6311. doi: 10.1264/jsme2.ME14128. Place: Japan.

[203] Oliver Pohl, Marius Hintsche, Zahra Alirezaeizanjani, Maximilian Seyrich, Carsten Beta, and Holger Stark. Inferring the Chemotactic Strategy of P. putida and E. coli Using Modified Kramers-Moyal Coefficients. *PLoS computational biology*, 13 (1):e1005329, January 2017. ISSN 1553-7358 1553-734X. doi: 10.1371/journal.pcbi.1005329. Place: United States.

[204] Rajesh Balagam and Oleg A. Igoshin. Mechanism for Collective Cell Alignment in Myxococcus xanthus Bacteria. *PLoS computational biology*, 11(8):e1004474, August 2015. ISSN 1553-7358 1553-734X. doi: 10.1371/journal.pcbi.1004474. Place: United States.

[205] Matthew D. Egbert, Xabier E. Barandiaran, and Ezequiel A. Di Paolo. A minimal model of metabolism-based chemotaxis. *PLoS computational biology*, 6(12):e1001004, December 2010. ISSN 1553-7358 1553-734X. doi: 10.1371/journal.pcbi.1001004. Place: United States.

[206] Gayan Abeysinghe, Momoka Kuchira, Gamon Kudo, Shunsuke Masuo, Akihiro Ninomiya, Kohei Takahashi, Andrew S. Utada, Daisuke Hagiwara, Nobuhiko Nomura, Naoki Takaya, Nozomu Obana, and Norio Takeshita. Fungal mycelia and bacterial

thiamine establish a mutualistic growth mechanism. *Life science alliance*, 3(12), December 2020. ISSN 2575-1077. doi: 10.26508/lsa.202000878. Place: United States.

[207] Shiv Prasad and Avinash P. Ingle. Chapter 12 - Impacts of sustainable biofuels production from biomass. In Mahendra Rai and Avinash P. Ingle, editors, *Sustainable Bioenergy*, pages 327–346. Elsevier, 2019. ISBN 978-0-12-817654-2. doi: https://doi.org/10.1016/B978-0-12-817654-2.00012-5. URL https://www.sciencedirect.com/science/article/pii/B9780128176542000125.

[208] S. C. Bhatia. 26 - Issues relating to biofuels. In S. C. Bhatia, editor, *Advanced Renewable Energy Systems*, pages 688–718. Woodhead Publishing India, 2014. ISBN 978-1-78242-269-3. doi: https://doi.org/10.1016/B978-1-78242-269-3.50026-7. URL https://www.sciencedirect.com/science/article/pii/B9781782422693500267.

[209] Zhenzhen Qiao, Timothy B. Yates, Him K. Shrestha, Nancy L. Engle, Amy Flanagan, Jennifer L. Morrell-Falvey, Yali Sun, Timothy J. Tschaplinski, Paul E. Abraham, Jessy Labbé, Zeng-Yu Wang, Robert L. Hettich, Gerald A. Tuskan, Wellington Muchero, and Jin-Gui Chen. Towards engineering ectomycorrhization into switchgrass bioenergy crops via a lectin receptor-like kinase. *Plant biotechnology journal*, 19 (12):2454–2468, December 2021. ISSN 1467-7652 1467-7644. doi: 10.1111/pbi.13671. Place: England.

[210] A. Deveau, B. Palin, C. Delaruelle, M. Peter, A. Kohler, J. C. Pierrat, A. Sarniguet, J. Garbaye, F. Martin, and P. Frey-Klett. The mycorrhiza helper Pseudomonas fluorescens BBc6R8 has a specific priming effect on the growth, morphology and gene expression of the ectomycorrhizal fungus Laccaria bicolor S238N. *The New phytologist*, 175(4):743–755, 2007. ISSN 0028-646X. doi: 10.1111/j.1469-8137.2007.02148.x. Place: England.

[211] Jessy L. Labbé, David J. Weston, Nora Dunkirk, Dale A. Pelletier, and Gerald A. Tuskan. Newly identified helper bacteria stimulate ectomycorrhizal formation in Populus. *Frontiers in plant science*, 5:579, 2014. ISSN 1664-462X. doi: 10.3389/fpls.2014.00579. Place: Switzerland.

[212] A. Mosnier, P. Havlík, H. Valin, J.S. Baker, B.C. Murray, S. Feng, M. Obersteiner, B.A. McCarl, S.K. Rose, and U.A. Schneider. The Net Global Effects of Alternative U.S. Biofuel Mandates: Fossil Fuel Displacement, Indirect Land Use Change, and the Role of Agricultural Productivity Growth. Technical Report Report NI R 12-01. Durham, NC, Nicholas Institute for Environmental Policy Solutions, Duke University, 2012.

[213] Robert M. Macnab and D. E. Koshland. The Gradient-Sensing Mechanism in Bacterial Chemotaxis. *Proceedings of the National Academy of Sciences*, 69(9):2509–2512, 1972. doi: 10.1073/pnas.69.9.2509. URL https://www.pnas.org/doi/abs/10.1073/pnas.69.9.2509. _eprint: https://www.pnas.org/doi/pdf/10.1073/pnas.69.9.2509.

[214] George W. Ordal and Daniel J. Goldman. Chemotaxis Away from Uncouplers of Oxidative Phosphorylation in *Bacillus subtilis*. *Science*, 189(4205):802–805, 1975. doi: 10.1126/science.808854. URL https://www.science.org/doi/abs/10.1126/science.808854. _eprint: https://www.science.org/doi/pdf/10.1126/science.808854.

[215] Marianne Grognot and Katja M. Taute. More than propellers: how flagella shape bacterial motility behaviors. *Current Opinion in Microbiology*, 61:73–81, 2021. ISSN 1369-5274. doi: https://doi.org/10.1016/j.mib.2021.02.005. URL https://www.sciencedirect.com/science/article/pii/S136952742100028X.

[216] Johannes Taktikos, Holger Stark, and Vasily Zaburdaev. How the Motility Pattern of Bacteria Affects Their Dispersal and Chemotaxis. *PLOS ONE*, 8(12):1–8, December 2014. doi: 10.1371/journal.pone.0081936. URL https://doi.org/10.1371/journal.pone.0081936. Publisher: Public Library of Science.